MICROCAVITY POLARITONS
PROPAGATION, SCATTERING, AND LOCALIZATION

Joanna M Zając

A THESIS SUBMITTED TO
CARDIFF UNIVERSITY
FOR THE DEGREE OF
DOCTOR OF PHYSICS

SEPTEMBER 2012

Declaration

This work has not previously been accepted in substance for any degree and is not being concurrently submitted in candidature for any degree.

Signed: ____________________
Candidate

Date: ____________________

Statement 1

This thesis is the result of my own investigations, except where otherwise stated. Other sources are acknowledged by giving explicit references. A bibliography is appended.

Signed: ____________________
Candidate

Date: ____________________

Statement 2

I hereby give consent for my thesis, if accepted, to be available for photocopying and for inter-library loan, and for the title and summary to be available to outside organisations.

Signed: ____________________
Candidate

Date: ____________________

To: My Dad
Wojtek Zając

ACKNOWLEDGEMENTS

I am grateful to Prof. Pavlos Lagoudakis who had supervised my Master dissertation at Southampton University for indicating the directions of my scientific development and sharing with me his enthusiasm to Physics.

I am grateful to Prof. Wolfgang Langbein who had supervised my Doctorate thesis at Cardiff University for supervising my work, insightful comments and detailed analysis of my work.

I would like to acknowledge all colleges and collaborators who contributed to the progress of this work.

ABSTRACT

Strong coupling between a Fabry-Perot cavity mode and a quantum well exciton give rise to the new quasi-particles microcavity exciton-polaritons. Microcavity polaritons were for the first time demonstrated in 1992 in Ref [1] and since then, the field developed dramatically.

Fundamental physics was explored in these systems including a quantum phase transitions of microcavity polaritons [2–4], demonstration of quantized vortices [5] and superfluidity [6]. Concerning applications [7], properties of microcavity polaritons are explored in optoelectronic devices *e.g.* low threshold electrically pumped polariton lasers, polarization sensitive optical bistable switches, spin memories and spin logic gates.

Main research interest of this work concerned the field of quantum phase transitions and the many-body physics of microcavity polaritons which are relatively easily accessible experimentally as compared to similar physics in cold-atoms systems [8] from the point of view of equipment complexity. However, in polariton physics, samples with desirable properties play a crucial role. Microcavity samples commonly suffer from disorder, for both the exciton and the photon components of the polaritons, which strongly modifies polariton quantum effects and makes them difficult to interpret. This fact emphasizes the importance of the further development in the field of the sample design and growth, and this was one of the goals of this contribution.

In particular, we worked to identify and suppress disorder in microcavity samples and to develop reproducible growth receipts providing samples with long photon lifetime. Photonic disorder was identified as cross-hatch dislocations and point-like-defects. A novel cross-hatch suppressing sample design was proposed and demonstrated, providing samples with long polariton propagation lengths in the order of millimeters in which genuine quantum fluid effects can be explored. Moreover, the origin behind the point-like-defects formation was identified as Ga nano-droplets deposited in microcavity during the molecular-beam epitaxial growth. These states were investigated using surface (differential-interference contrast microscopy, scanning-electron microscopy, chemical etching) and volume (focused-ion beam milling) techniques. Point-like-defect resulted in 0-dimensional polariton states exhibiting quantized energy levels which we have characterized in real and reciprocal space.

The second part of this work was the investigation of quantum many-body effects in low disorder microcavities. In particular, we investigated polariton parametric scattering and demonstrated experimentally and theoretically scattering into "ghost" branches which arises due to energy and momentum conservation of polaritons.

Finally, we theoretically modeled quantum fluid effects of polaritons using Gross-Pitaievskii equation reproducing superfluid transition and bistability for spin independent polariton interactions.

PUBLICATIONS

Optical analogue of the spin Hall effect in a photonic cavity M Maragkou, C E Richards, T Ostatnicky, A J D Grundy, J M Zajac, M Hugues, W Langbein, and P G Lagoudakis Optics Letters, **36**, 7, 1095-1097 (2011)

Polariton states bound to defects in GaAs/AlAs planar microcavities, J M Zajac, W Langbein, M Hugues, M Hopkinson, Phys. Rev. B **85**, 165309 (2012)

Suppression of cross-hatched polariton disorder in GaAs/AlAs microcavities by strain compensation, J M Zajac, E Clarke, W Langbein, Appl. Phys. Lett. **101**, 041114 (2012)

Structure and zero-dimensional polariton spectrum of natural defects in GaAs/AlAs microcavities J M Zajac and W Langbein, Phys. Rev. B **86**, 195401 (2012) Publication chosen as Editors' Suggestion for publication of particular interest, importance, or clarity.

Parametric scattering of microcavity polaritons into ghost branches J M Zajac and W Langbein, Phys. Rev. Lett. (submitted)

PRESENTATIONS

J M Zajac, W Langbein, Two-dimensional imaging of a high quality planar microcavity in real and reciprocal space, *Cold Atoms and Condensed Mater Physics Conference*, Durham, UK, 2009

J M Zajac, W Langbein, Two-dimensional imaging of a high quality planar microcavity in real and reciprocal space, *Speaking about Science*, Cardiff University, UK, 2010

J M Zajac, W Langbein, Two-dimensional imaging of a high quality planar microcavity in real and reciprocal space, *Physics Chat*, Cardiff University, UK, 2010

J M Zajac, W Langbein, Localized polaritons states in planar microcavities, *POLATOM Network conference*, Crete, Greece, 2011

J M Zajac, W Langbein, Localized polaritons states in planar microcavities, *Summer School in Quantum Information and Coherence (SUSSP67)*, Glasgow, UK, 2011

J M Zajac, W Langbein, Photonic disorder in planar semiconductor microcavities, *Optics of excitons in confined systems(OECS)12*, Paris, France, 2011

J M Zajac, W Langbein, Parametric scattering of microcavity polaritons into ghost branches, *POLATOM Network conference*, Cambridge, UK, 2012

J M Zajac, E Clarke, W Langbein, Suppression of cross-hatched polariton disorder in GaAs/AlAs microcavities by strain compensation, *POLATOM Network conference*, Cambridge, UK, 2012

CONTENTS

LIST OF TABLES

List of Figures

1 Physics of microcavity polaritons

In this chapter, the foundations of microcavity polariton physics are discussed. Firstly, in Sec. 1.1, properties of As based III-V semiconductors are presented. Then, the fundamental concepts of excitons and cavity photons are discussed, followed by a description of strong and weak coupling between exciton and cavity photon in the classical and quantum picture with emphasis on the linewidth of polaritons. Further to this in Sec. 1.2, a detailed description of the molecular beam epitaxial growth of GaAs based microcavities with embedded InGaAs/GaAs or AlGaAs/GaAs quantum wells is given together with a discussion of advanced growth techniques. Finally in the Sec. 1.3, a literature on microcavity polaritons is briefly reviewed.

1.1 Microcavity exciton polaritons

1.1.1 III-V semiconductor alloys

We consider hereafter binary and ternary alloys of III-V semiconductors, particularly GaAs, AlAs and InAs. These compounds crystalize in the zinc-blende lattice structure. Both GaAs and InAs are *direct band gap* semiconductors, while AlAs is *indirect* as the conduction band (CB) minimum is at the X point while the valence band (VB) maximum is at the Γ point of the Brillouin zone[1]. We will consider the electronic structure of GaAs and optical transitions between the conduction band and heavy- and light-holes valence bands as shown in Fig. 1.1. For small momenta conduction band is parabolic with dispersion $E_{CB} = \frac{\hbar^2 k^2}{2m_e} + E_g$ where k is electron momentum, m_e is an electron mass and E_g is a band gapenergy if the VB maximum is

---

[1] Γ point: $k_x = 0 = k_y = k_z$; X point: $k_x = \frac{2\pi}{a}$;$k_y = k_z = 0$; L point: $k_x = k_y = k_z = \frac{\pi}{a}$ where a is lattice constant

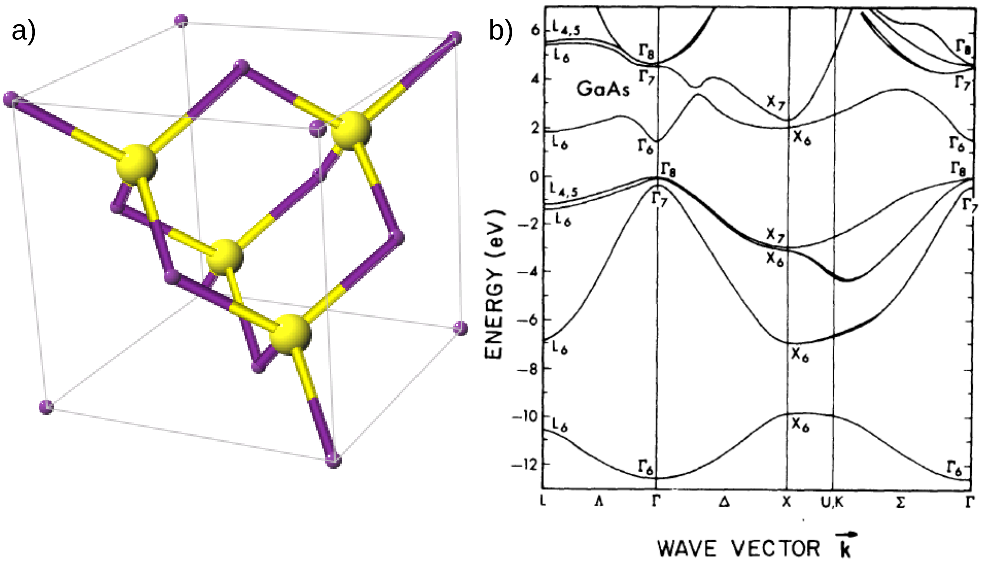

Figure 1.1: In a) zinc-blende structure of GaAs, Ga atoms are shown in yellow and As atoms are in violet. In b), band structure of GaAs along highly symmetric directions obtained by a non-local pseudopotential calculaitons[9, 11].

at $E = 0$. Heavy- and light-holes subbands are anisotropic, their detailed dispersion can be found in Ref. [9, 10]. The temperature dependence of the band gap energy E_g (eV) for semiconductor material is written using the Varshni empirical formula [12]:

$$E_g = E_{g0} - \frac{\alpha T^2}{\beta + T} \tag{1.1}$$

where E_{g0} is energy gap at temperature 0K, and material parameters are listed in Table 1.1. Refractive indices of $\mathrm{Al}_x\mathrm{Ga}_{1-x}\mathrm{As}$ and its dependency on temperature for the wavelength range $800 - 900$ nm relevant in this work is given in Ref. [13]. For ternary *semiconductor alloys*, the dependence of the band gap on the alloy composition at

Alloy	E_{g0} (eV)	α (10^{-4} eV/K)	β (K)
GaAs[12]	1.517	5.5	225
AlAs[14]	2.239	6.0	408
InAs[15]	0.420	2.5	75

Table 1.1: Parameters of the temperature dependent band gap for GaAs, AlAs and InAs

low temperatures (T∼ 10 K) after Ref. [10] is:

$$\mathrm{Al}_x\mathrm{Ga}_{1-x}\mathrm{As} \qquad E_{g0} = 1.519 + 1.36x + 0.22x^2 \tag{1.2}$$

$$\mathrm{In}_x\mathrm{Ga}_{1-x}\mathrm{As} \qquad E_{g0} = 1.519 - 1.584x + 0.475x^2 \tag{1.3}$$

1.1.2 EXCITONS

Excitons are electron-hole pairs bound by the Coulomb potential. For the Wannier excitons, exciton energy E_{XB} and exciton Bohr radius a_{XB} in a 3-dimensional structure can be expressed in terms of the Rydberg energy $R_y = 13.6\,\mathrm{eV}$ and Bohr radius $a_B = 0.053\,\mathrm{nm}$ as

$$E_{XB,3d} = \frac{R_y^*}{n^2} = R_y \frac{\mu}{m_e} \frac{1}{\varepsilon^2 n^2} \tag{1.4}$$

$$a_{XB,3d} = a_B \frac{m_e}{\varepsilon \mu} \tag{1.5}$$

where R_y^* is exciton Rydberg energy, ε is crystal dielectric constant, m_e is the electron mass, $n = 1, 2, 3...$ is the principal quantum number, $\mu = (1/m_e + 1/m_h)^{-1}$ is the reduced mass where m_e,m_h are electron and hole masses. For bulk GaAs, the exciton binding energy and the exciton Bohr radius are $E_{XB} = 4.1\,\mathrm{meV}$, $a_{XB} = 14\,\mathrm{nm}$[16] for the ground state exciton (N=1). In general, exciton binding energies for binary semiconductors increases with band gap energy of the material, shown in Fig. 1.2a). The exciton energy takes the form

$$E_{X,3d} = E_g - E_{XB,3d} + \frac{\hbar^2 K^2}{2M} \tag{1.6}$$

where $M = m_e + m_h$, $K = k_e + k_h$ is the exciton translational mass and wavevector, where subscripts e,h stand for e-electron and h-hole mass and wevevectors. In *low dimensional structures*, electronic confinement is engineered by spatially varying alloy composition. If the band gap modulation takes place on a length scale comparable or smaller than exciton Bohr radius, excitons are confined. The density of states without spin degeneracy (DOS) as a function of energy for parabolic energy dispersion is

$$\begin{aligned} \text{1-dim:} \qquad DOS &= \frac{\sqrt{m}L}{\pi\sqrt{2}\hbar}\frac{1}{\sqrt{E}} \\ \text{2-dim:} \qquad DOS &= \frac{mL^2}{2\pi\hbar^2} \\ \text{3-dim:} \qquad DOS &= \frac{2\pi(2m)^{\frac{3}{2}}L^3}{\hbar^2}\sqrt{E} \end{aligned} \tag{1.7}$$

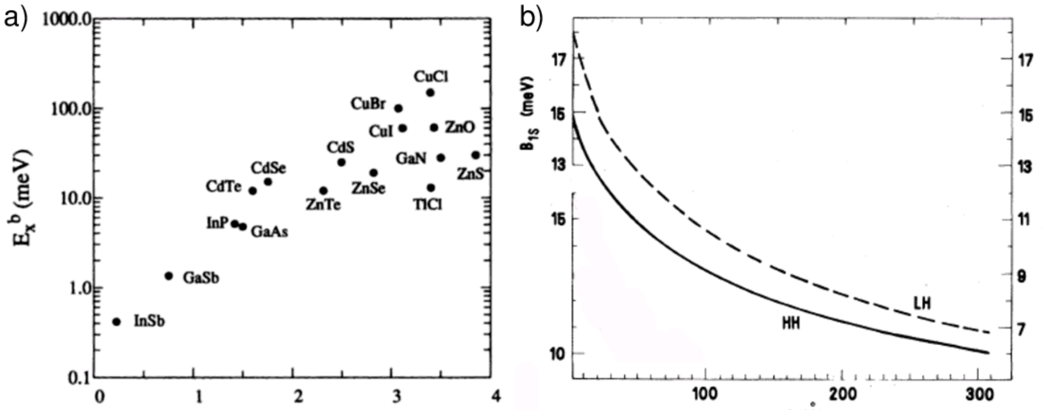

Figure 1.2: In a), exciton binding energy for different materials after Ref. [16]. In b), calculated exciton binding energy for $Al_{0.37}Ga_{0.63}As/GaAs$ quantum wells as function of wells width calculated for infinite wells [19].

for 1,2 and 3-dimensional structures respectively where L is the dimension of the crystal. E_{XB} is a function of dimensionality and will increase as the dimensionality decreases as the electron and hole are pushed closer together due to the confinement and will interact stronger due to the Coulomb potential. The exciton energy in 2-dimensional structure is written as

$$\text{2-dim:} \qquad E_{X,2d} = E_g + E_Q - E_{XB,2d} + \frac{\hbar^2(K_x^2 + K_y^2)}{2M} \tag{1.8}$$

where E_Q is a quantization energy of electron and hole, for the strong confinement[2] $E_Q = \frac{N^2\hbar^2\pi^2}{2\mu L_Q^2}$ where L_Q is the confinement length,$N \in N$. $E_{XB,2d} = R_y^* \frac{1}{(n-\frac{1}{2})^2}$ in two dimensional structures, which for the ground state exciton gives $E_{XB,2d} = 4E_{XB,3d}$, see Fig. 1.2 where the calculated exciton binding energy is plotted as a function of well width for $Al_{0.37}Ga_{0.63}As/GaAs$ quantum wells, it give in general good agreement with experiment[17].

The exciton is a composite boson and above the saturation density it dissociates due to the screening of the Coulomb interaction by free carriers, this is given by the saturation density [18]

$$n_{sat} = \frac{0.139}{a_{XB}^2} \tag{1.9}$$

for $a_{XB} = 14\,\text{nm}$ this results gives $n_{sat} = 8 \cdot 10^{10}$ excitons/cm^2.

---

[2] Strong confinement is when the size of confinement is comparable or smaller than the exciton Bohr radius.

The susceptibility of an exciton with a transition frequency ω_{mn} is given by [20]

$$\chi(\omega) = \frac{n_0 e^2 f_{mn}}{2m\omega_{mn}} \frac{1}{\omega - \omega_{mn} - i\gamma'} \tag{1.10}$$

where ω_{mn} is exciton resonance where m, n are initial and final states respectively, n_0 is an exciton density, f_{mn} is a exciton oscillator strength for transition frequency ω_{mn}, γ' is the homogenous linewidth of exciton which is a sum of the radiative linewidth, Γ, and the non-radiative linewidth, γ which results from exciton-phonon, exciton-free carrier or exciton-exciton scattering. In most samples, there is also inhomogeneous contribution to the exciton linewidth which is a consequence of an alloy composition fluctuations and quantum well thickness fluctuations, see Sec. 1.2.1.
Teh exciton oscillator strength for ω_{mn} transition is

$$f_{mn} = \frac{2m}{\hbar} \frac{|d_{mn}|^2}{e^2} \omega_{mn} \tag{1.11}$$

where $d_{mn} = \langle m|d|n\rangle = \int d^3 r \psi_m^*(\mathbf{r}) d\psi_n^*(\mathbf{r})$ is the electric dipole matrix element describing light-matter coupling strength. It is closely related to the Rabi frequency, Ω_R, for dressed excitons and photons[20]

$$\Omega_R = \frac{|d_{mn} E_{vac}|}{\hbar} \tag{1.12}$$

where E_{vac} is a vacuum field amplitude.

1.1.3 MICROCAVITY PHOTONS

A Fabry-Perot resonator consist of a cavity layer sandwiched between two highly reflective mirrors. For semiconductor microcavities, distributed Bragg reflectors (DBRs) are used as mirrors, they consist of alternating $\frac{\lambda}{4}$ layers of high refractive index contrast materials where $\lambda = \lambda_0 / n_i$ is a cavity mode wavelength in the medium, λ_0 is a cavity mode wavelength in the vacuum with refractive index of the medium n_i. In transmission, due to reflection on interfaces and destructive interference, DBRs give rise to a photonic band gap. The microcavity spacer layer can be seen as a defect in a periodic structure which length is chosen such that it ensures the constructive interference of intra-cavity field. Intracavity fields penetrates into the DBRs such that the effective cavity length, L_{eff} is defined as $L_{eff} = L_{cav} + L_{DBR}$ where[18]

$$L_{DBR} = \frac{\lambda}{2} \frac{n_1 n_2}{n_{cav}(n_2 - n_1)},\ n_1 < n_2 \tag{1.13}$$

where n_1,n_2 are refractive indices of DBR layers. Condition for constructive interference yields

$$\frac{n_{cav}}{c}[(\omega-\omega_c)L_{cav}+(\omega-\omega_m)L_{DBR}]=N\pi \tag{1.14}$$

where ω_c,ω_m is the resonance frequency of the cavity and DBRs,n_{cav} is a spacer refractive index.

Reflectivity of a DBR with N pairs of layers calculated using transfer matrix method [18, 21] leads

$$R(\omega)=1-4\frac{n_{ext}}{n_{cav}}\left(\frac{n_1}{n_2}\right)^{2N},\ n_1<n_2 \tag{1.15}$$

where n_{ext},n_{cav} are refractive indices of external medium and cavity respectively. It is clearly seen from Eq.(1.15) that DBRs with higher index contrast provide a higher reflectivity. For the GaAs/AlAs DBRs used in this work, the refractive index contrast is $\Delta n=0.6$[3] which is relatively modest such that in order to achieve high reflectivity of $R=0.9999$, 25 DBR need to be used.

The homogenous Fabry-Perot linewidth resulting from the decay of the mode through the mirror is

$$\gamma_{cav}=\frac{1-\sqrt{R}}{2\sqrt{R}}\frac{c}{n_{cav}L_{eff}} \tag{1.16}$$

The quality factor of the cavity is defined as $Q=\frac{\omega_{cav}}{\gamma_{cav}}$, Q^{-1} is a measure of the relative energy loss in a single round trip in the cavity. During this work, a structure with $Q=1.5\cdot10^5$ equivalent to 100ps photon lifetime was designed, measured Lorenzian linewidths indicated $Q=10^5$ and lifetimes in the order of 30-50ps, for free polaritons as will be discussed in more details in Chap. 3.

The Fabry-Perot mode dispersion is written as[22]

$$E_{cav}(k)=\frac{hck}{n_{cav}}=\frac{\hbar c}{n_{cav}}\sqrt{\left(\frac{2\pi}{L_{cav}}\right)^2+k_{xy}^2}\approx E(k=0)+\frac{\hbar k_{xy}^2}{2m_{cav}} \tag{1.17}$$

where k_{xy} is a wavevector in the cavity plane, $m_{cav}=\frac{2\pi\hbar n_{cav}}{c\,L_{cav}}$ has the meaning of cavity photon mass, for the samples studied in this work, it is in the order of $2\cdot10^{-5}m_e$ [23]. The above approximation resulting in a parabolic cavity photon dispersion was obtained using the Taylor series expansion and is valid for $k_{xy}\ll\frac{2\pi}{L_{cav}}$. It is important to emphasize that the cavity mode dispersion described by Eq.(1.17) does not have a minimum at $E=0$ as for a free propagating photon, but instead, due to quantization of k_z, it will have a minimum at $E=\frac{\hbar c 2\pi}{n_{cav}L_{cav}}$. This is the important element giving

---

[3] GaAs and AlAs refractive indices are $n_{GaAs}=3.6$, $n_{AlAs}=3$ respectively for $\lambda_0=850\,\mathrm{nm}$ at room temperature

rise to the bosonic stimulation of polaritons in microcavities which will be described later in Sec. 1.3 and Chap. 5.

1.1.4 EXCITON-POLARITON

It is important to answer the question "What is propagating when light travels in matter?" [16]. When light propagates in vacuum, the answer is photons, when light propagates in matter, it induces a polarization field **P** wich interacts which an incident electric field **E**, it is written as

$$\begin{aligned} P(t) = \ & \epsilon_0[\chi^{(1)}E(t) + \chi^{(2)}E(t)^2 + \chi^{(3)}E(t)^3 + ...] \\ & = \tilde{P}^{(1)}(t) + \tilde{P}^{(2)}(t) + \tilde{P}^{(3)}(t) + ... \end{aligned} \tag{1.18}$$

The light-matter quantum or polarization wave is called a polariton. There are two formalisms to consider polaritons[20], in particular, through semiclassical dielectric theory and quantum theory. The first is derived using Hopfield equations[24], which are derived from Maxwell equation for polarization of the medium. Hereafter, we are interested in the situation when active material is embedded inside a planar microcavity. Hopfield equations can be simplified leading to the *two-oscillator model*[18, 25] which provides the polariton dispersion in analytical and simple form

$$(\omega - \omega_X + i\gamma_X)(\omega - \omega_{cav} + i\gamma_{cav}) = V^2, \text{with } V^2 = \frac{(1+\sqrt{R})^2}{2\sqrt{R}} \frac{c\hbar\Gamma_0}{n_{cav}L_{eff}} \tag{1.19}$$

where ω_X,ω_{cav} is an exciton and a Fabry-Perot mode energy, γ_X,γ_{cav} is an exciton and a Fabry-Perot mode linewidth, Γ_0 is the exciton homogenous linewidth. Using the above notation, the condition for strong coupling is $4V^2 > (\gamma_{cav} - \gamma)^2$, together with the condition on exciton and photon linewidths $\gamma_X, \gamma_{cav} < \Omega_R$ where Ω_R is Rabi splitting

$$\Omega_R = 2\sqrt{|V|^2 - \frac{1}{4}(\gamma_{cav} - \gamma)^2} \tag{1.20}$$

In order to calculate V for experimental parameters, we take a cavity with an average of 25 GaAs/AlAs DBR layers, reflectivity $R = 0.9999$ as calculated in Sec. 1.1.3. L_{eff} for 1λ GaAs cavity is 2.6μm Sec. 1.1.3. InGaAs/GaAs quantum well exciton homogenous linewidth is $\simeq \Gamma_0 = 40\mu$eV. Inserting these values into Eq.(1.19) and Eq.(1.20), we obtain $V = 1.3\,$meV and $\Omega_R = 2.6\,$meV which agree with experimental values. The advantage of this model is that it includes finite mode linewidths in a simple manner. Polariton energies and linewidths are plotted in Fig. 1.3a) as a function of detuning $\delta = \omega_{cav} - \omega_X$. In Fig. 1.3b), the Rabi splitting and the polariton broadening are plotted as a function of the DBR reflectivity, after Ref.[18]. The transition between weak and strong coupling regime is evident for R=0.85.

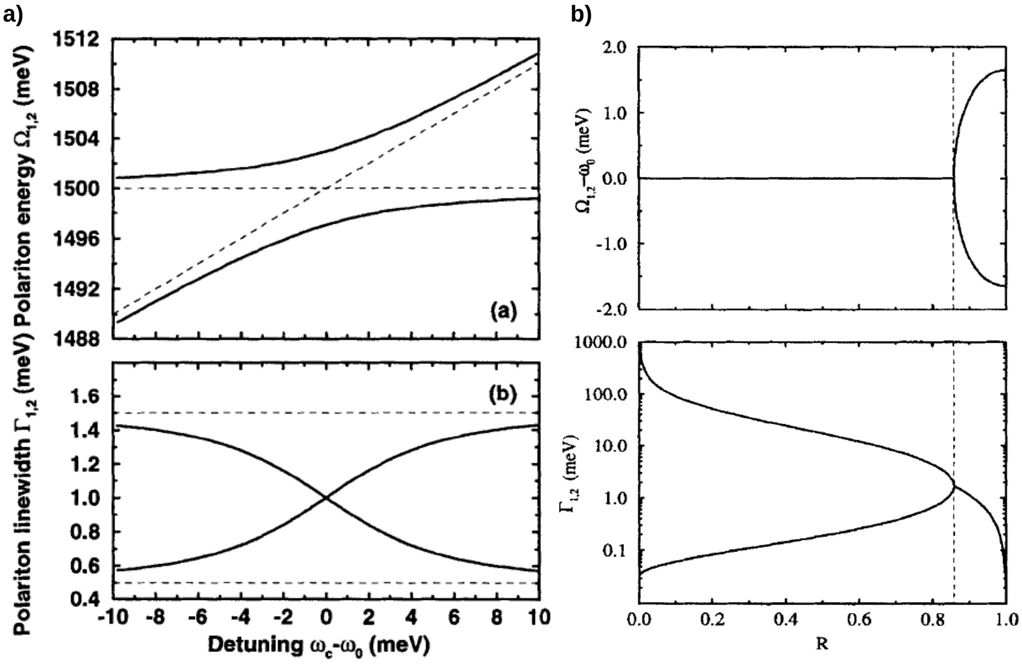

Figure 1.3: In a) the polariton energy(top) and linewidth(bottom) are plotted as function of detuning $\delta = \omega_{cav} - \omega_X$, dashed lines on both plots indicate uncoupled quantities. In b) the Rabi splitting and the polariton broadening are plotted as a function of the DBR reflectivity [18].

Model Hamiltonian: Using second quantization and the notation from [26], the Hamiltonian of the coupled exciton-photon oscillators is written as

$$H_0 = \sum_k \left(E_{cav} a_k^\dagger a_k + E_X b_k^\dagger b_k + \hbar\Omega_R (a_k^\dagger b_k + a_k b_k^\dagger) \right) \tag{1.21}$$

where a is a photon operator, b is an exciton operator in the second quantization [4], we used notation $k = k_{xy}$. In order to find eigenstates of the system, the Hamiltonian from Eq.(1.21) is diagonalised leading to

$$H_0 = \sum_k \left(E_{LP} p_k^\dagger p_k + E_{UP} u_k^\dagger u_k \right) \tag{1.22}$$

---

[4] Creation and annihilation operators are defined as $\hat{a}^\dagger|n\rangle = (n+1)^{1/2}|n+1\rangle$, $\hat{a}|n\rangle = n^{1/2}|n-1\rangle$ respectively, where $|n\rangle$ is the number state which corresponds to the harmonic oscillator eigenstates with n quanta of energy[27]. Polariton operators satisfy bosonic commutation rules: $[a_k, a_{k'}] = [a_k^\dagger, a_{k'}^\dagger] = 0$, $[a_k, a_{k'}^\dagger] = \delta_{k\,k'}$.

where p_k,u_k are lower and upper polaritons operators obtained through unitary transformation

$$\begin{pmatrix} p_k \\ u_k \end{pmatrix} = \begin{pmatrix} X_k & C_k \\ -C_k & X_k \end{pmatrix} \begin{pmatrix} b_k \\ a_k \end{pmatrix} \tag{1.23}$$

where the $X_c > 0$,$C_k < 0$ are Hopfield coefficients. For the lower polariton branch, they are given by the following expressions:

$$\begin{aligned} X_k &= \frac{1}{\sqrt{1+\left(\frac{\hbar\Omega_R}{E_{LP}(k)-E_C(k)}\right)^2}} \\ C_k &= -\frac{1}{\sqrt{1+\left(\frac{E_{LP}(k)-E_C(k)}{\hbar\Omega_R}\right)^2}} \end{aligned} \tag{1.24}$$

The lower polariton operator is defined as $p_k = X_k b_k + C_k a_k$, the quantities $|X_k|^2$ and $|C_k|^2 = 1 - |X_k|^2$ represent the exciton and photon content of polariton.

1.1.4.1 Discussion about dimensionality

In order to work in the strong coupling regime, excitonic and photonic components of polaritons have to have the same dimensionality to satisfy momentum conservation rules, see Table 1.2. During this work, we have studied coupling between 2-dimensional excitons and 2-dimensional photons. In particular, the Fabry-Perot mode energy is quantized due to confinement inside the cavity, compare Eq.(1.17), excitons were confined by quantum wells embedded inside a cavity or by the entire microcavity layer used as active material. In the latter case, cavity lengths were between 0.24 and 0.5μm which is an intermediate regime between a bulk material and quantum wells cavities, namely, carrier confinement effects are absent but quantization of the exciton center of mass motion occurs[28, 29]. Strong coupling between a bulk $n = 1$ GaAs exciton and Fabry-Perot 2λ cavity mode with Rabbi splitting in the order of 4meV was reported [28]. Bulk microcavities exhibit smaller oscillator strength because of greater thickness and smaller exciton broadening ($\gamma_X \sim 0.1$meV) as compared with quantum well structures. During this study, we did not observe signatures of strong coupling in bulk microcavities, cavity mode was red detuned from the bulk exciton by $20 - 50$meV as will be discussed in Chap. 3.

Bulk	Exciton 3D	Strong coupling
	Photon 3D	Exciton-polariton
	$\mathbf{k}_{3D}$ selection rule	Extrinsic radiative process
Quantum well	Exciton 2D	Weak coupling
	Photon 3D	Intrinsic radiative process
	$\mathbf{k}_{\perp}$ continuum	
Quantum well in planar cavity	Exciton 2D	Strong coupling
	Photon 2D	Cavity-polariton
	$\mathbf{k}_{\|\|}$ selection rules	Extrinsic radiative processes

Table 1.2: Exciton-photon interaction for different dimensionalities [30]

1.2 MBE GROWTH

Molecular beam epitaxy (MBE) is a growth technique of semiconductor thin films developed in 1960s. Semiconductor materials are evaporated in a high vacuum environment from a solid state or liquid phase source, and deposited onto a heated substrate where they crystalize forming a single-crystal epitaxial layer. As the name indicates, molecules propagate as a beam with negligible interactions. In practise, growth takes place under high vacuum at a pressure $10^{-3} > p > 10^{-9}$ mbar, or in ultra high vacuum, $p < 10^{-9}$ mbar.The growth rate is controlled through the temperature of effusion cell, switching between the growth of different elements is done using shutters in front of the effusion cells. Growth on a wafer surface is an interplay between atoms' adsorption, surface migration, incorporation, thermal desorption. Possible growth regimes are Layer-by-layer (Frank van der Merwe), layer plus islands (Stanski-Krastanov), and islands (Volmer-Weber) growth modes. In-situ characterization techniques, providing precise growth rate calibration, include reflection high energy electrons diffraction (RHEED) and ellipsometry. Post-growth characterization techniques include X-Ray diffraction, photoluminescence (PL), transmission electron microscopy (TEM).

1.2.1 MBE GROWTH OF III-V MICROCAVITIES

Relevant for this thesis is growth of As based III-V alloys, namely GaAs, AlAs, InGaAs. During this work we have designed and characterized 20 MBE grown wafers, samples were grown in the National Center for III-V Technology in Sheffield, United Kingdom, compare Appendix C.

The growth of III-V heterostructures takes place under V/III flux ratio of about 50 such that the growth rate is controlled by the pressure of group III-elements (Al,Ga,In) while group V-element (As,P) desorb unless covalently bound. Suggested growth conditions are listed in Table 1.3. During the growth, group III adatoms defuse on the surface until they bind to As atoms. High diffusion lengths are maintained by keeping sufficiently low growth rate and by increasing substrate temperature T_{sub}, which at the same time has to be kept below desorption temperature of compounds. Desorption temperatures are around 560°C for InAs, 640°C for GaAs, and 750°C for AlAs[31], compare T_{sub} in Table 1.3. The AlAs interface exhibits higher roughness, in the order of 2 nm, than GaAs interfaces, it is due to the higher surface migration of Ga than Al, namely 1 μm and 0.02 μm respectively as reported in Ref.[32]. When exposed to air, AlAs oxidizes stronger than GaAs as observed in ambient environment under FESEM, compare Chap. 3. The substrate temperature is monitored with a pyrometer and a thermocouple to achieve an accurate reading. Typical growth rates for GaAs and AlAs structures used in this work were 1μm/h resulting in 8 hour growth for the average microcavity structure. Growth rates are set by the cell temperatures which are equal to 300°C for Ga cell, 400°C for As, and 1000°C for Al. The stability of cell temperatures is crucial in order to maintain constant growth rates.

GaAs/AlAs/InGaAs alloys crystalize in zinc-blende lattice which consist of two interpenetrating fcc lattices where one of the lattice (Ga,Al,In) is shifted by $a/4\,[111]$ relative to the other (As) where a is the lattice constant. For fcc lattices due to symmetry, the stiffness tensor reduces to a matrix with only three independent constant elements C_{11}, C_{12}, C_{44} [33]. For the growth of AlAs on GaAs, the epilayer is grown with a lattice constant of the substrate, which is referred to as pseudomorphic growth which leads to a further simplification of the strain tensor elements

$$\begin{aligned}
\epsilon_{xx} &= \epsilon_{yy} = \varepsilon_{\mathrm{m}} = \frac{a_{\mathrm{s}} - a_{\mathrm{f}}}{a_{\mathrm{f}}} \\
\epsilon_{xy} &= \epsilon_{xz} = \epsilon_{yz} = 0 \\
\epsilon_{zz} &= -2\frac{C_{12}}{C_{11}}\epsilon_{xx} \qquad (1.25)
\end{aligned}$$

where a_{s} and a_{f} are the lattice constants of the substrate and the film respectively, $\varepsilon_{\mathrm{m}} < 0$ corresponds to comprehensive strain, while $\varepsilon_{\mathrm{m}} > 0$ to tensile strain. The surface energy of the grown layer is denoted as γ_s,γ_f,γ_{sf} [10] where s and f are energies of a substrate, film, and substrate-film interface layer. Different growth morphologies are deduced when comparing these energies, namely, if $\gamma_f + \gamma_{sf} < \gamma_s$, growth of layers is favorable which is referred to as the Frank-Van der Merwe or layer-by-layer growth. When $\gamma_f + \gamma_{sf} > \gamma_s$, growth of flat layers is overtaken by the growth of islands, this growth mode is called Volmer-Weber mode. The intermediate growth mode, $\gamma_f + \gamma_{sf} \approx \gamma_s$ is called Stranski-Krastanov and consist of the growth of wetting layer on the substrate which is followed by the growth of islands[10]. For AlAs on GaAs growth, due to small lattice mismatch, layer by layer growth is maintained. Above the critical thickness, strain relaxes by formation of misfit dislocation arrays called cross-hatched dislocation pattern with hatches along [110] and [$1\bar{1}0$]. More details on strain relaxation and strain compensation in these structures will be given in Chap. 4.

Alloy	III/V flux ratio	T_{sub}	Growth rate (μm/s)
InGaAs(001)	8-10	500-520°C	1
AlGaAs(001)	8-10	595-625°C	1

Table 1.3: Suggested growth conditions for alloys investigated in this work after Ref. [10, 31]

The cavity resonance depends on both the cavity and DBRs layers thicknesses, see Sec. 1.1.3, such that small errors in thickness and composition of any of the layers contribute to deterioration of the optical properties of the whole structure. For instance, systematic errors in the thickness of DBRs, e.g. a 5% reduction in the thickness of AlAs layer thickness in DBRs, reduces the stopband reflectivity from 99.95% to 99.91% and shifts the stopband by 30nm towards shorter wavelengths [31]. It is important to perform a careful calibration of growth rates with RHEED before each growth. Another common error is an uncompensated drift of the cell flux due to the material depletion, this has to be compensated by increasing the cell temperature. Growth conditions and material parameters can be extracted through reflectivity and photoluminescence measurements on an empty microcavity[5]. In particular, stability and uniformity of the growth can be accessed through spatially resolved cavity linewidth measurements, such results will be shown in Chap. 3, however, if quantum well resonance will be present, cavity linewidth is limited by the quantum well absorbtion.
Important for the growth of stronlgy coupled microcavities is to match the Fabry-Perot mode energy with the quantum well exciton energy, it is achieved by introducing the cavity layer thickness gradient over the wafer as will be discussed in Sec. 1.2.3 and Appendix C.

---

[5] Empty microcavity is understood here as a microcavity without quantum wells and not strongly coupled to the bulk exciton resonance

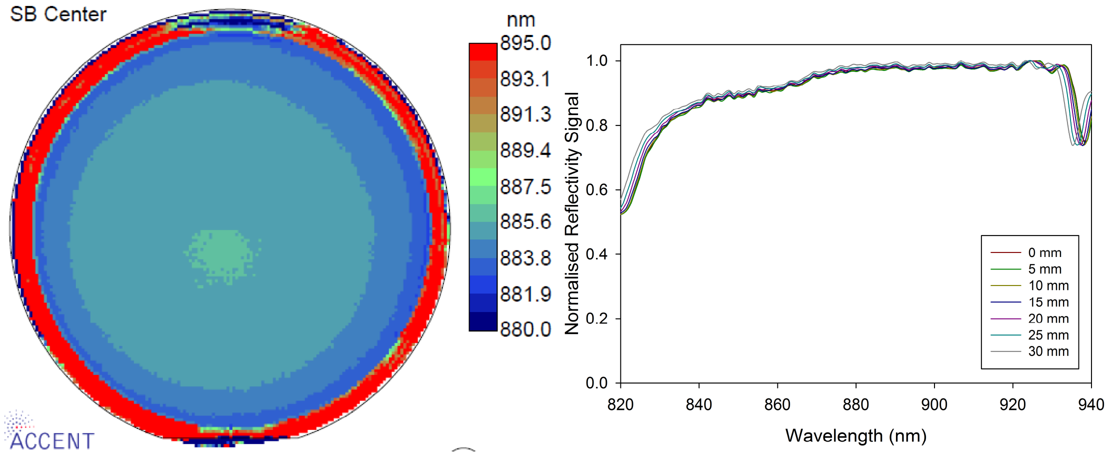

Figure 1.4: Example of the room temperature reflectivity map for GaAs microcavity with InGaAs quantum well, sample VN2303. The reflectivity of a stop band center (SB center) is mapped over the wafer using the color scale as shown. Spectrally resolved reflectivity is also shown for several positions on the wafer where 0 mm position denotes the center of the wafer and the position is changed along the big flat. The stopband bending visible on the plots is due to absorbtion of GaAs in the DBRs which is at 871 nm at room temperature. Close to the wafer edge no growth takes place due to shadowing of the wafer by the wafer mount, shown in red on the plot, reflection from this area can be disregarded.

1.2.2 MBE GROWTH OF QUANTUM WELLS

InGaAs/GaAs Quantum Wells: There are two contributions to the inhomogeneous broadening of excitons in ternary alloys, firstly, it is caused by exciton localization by the surface roughness in the quantum well plane, secondly, it arises due to surface segregation of compounds and randomness in the alloy. The surface segregation is caused by the net migration of compounds between crystalline sides in the growth direction which results in the concentration decreasing or increasing gradually between interfaces rather than having abrupt boundaries. Segregation is mostly pronounced for In atoms in GaAs/InGaAs quantum wells while GaAs/AlGaAs quantum wells have abrupt interfaces. Additionally, lattice mismatch between $a_{\mathrm{InAs}} = 0.60583\,\mathrm{nm}$ and $a_{\mathrm{GaAs}} = 0.56503\,\mathrm{nm}$ is $\varepsilon_{\mathrm{m}} \simeq 7\%$, and growth of strained films in layer plus islands growth mode contributes to broadening of exciton linewidths [10].

AlGaAs/GaAs Quantum Wells: Microcavities with GaAs quantum wells have narrower linewidths as compared to InGaAs quantum wells , typically below 0.1 meV for well sizes higher than exciton radius. Because of reduced alloy disorder and negligible strain, heavy- and light-holes subbands couple to light causing in general more complicated polariton spectra consisting of three polariton bands, lower, upper and

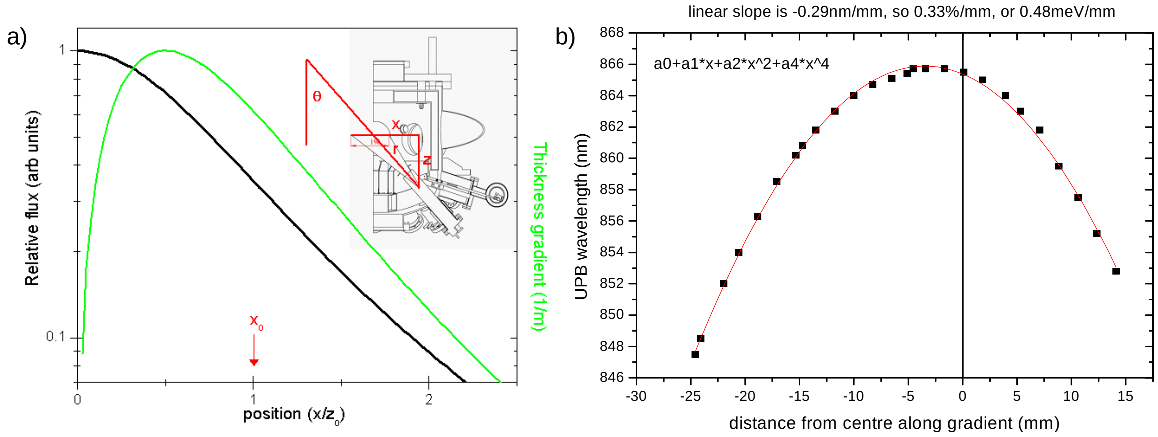

Figure 1.5: a) calculated flux and thickness gradient are plotted, in the inset geometry of sample chamber in VG V90 MBE machine. b) upper polariton peak wavelength is plotted as a function of the position on the wafer, contribution from the chamber geometry is suppressed due to wafer rotation, contribution from cell equal to 0.33%/mm is plotted, experimental points are fitted with polynomial in red on the plot.

middle polaritons, compare Chap. 5.

1.2.3 ADVANCED GROWTH TECHNIQUES

Thickness gradient: Due to the cell positioning relatively to the wafer and the cell geometry, the evaporated material flux I is non-uniform over the wafer. In particular, for the wafer positioned axially with respect to the effusion cell orifice, the material flux emitted into a solid angle Ω is constant and is given as

$$I = \int \Gamma d\Omega \simeq \Gamma \frac{S}{R^2} = const \tag{1.26}$$

where Γ is an emission rate, S is a surface area, R is distance between the cell orifice and the wafer. When the wafer is positioned nonaxially with respect to the effusion cell orifice, flux is $I \sim (R\cos(\theta))^{-2}$ where θ is an angle between normal to the wafer and the cell orifice, compare the chamber geometry in the inset to Fig. 1.5a). In Fig. 1.5a), the material flux for the VG V90 MBE machine used to grow the samples investigated during this work was calculated assuming for simplicity a cell to be a point like source, it was deduced as $h \simeq \frac{dI}{dx} = \frac{2x}{(1+x^2)^{5/2}}$ and is plotted in green. For the center of the wafer at x_0, thickness gradient can be approximated with a linear slope calculated as 5%/cm what was confirmed experimentally by measurement of the cavity mode wavelength gradient over the wafer. On the other hand, for continuous wafer rotation, thickness uniformity over the wafer is better than 1% in agrement with a manufacturer specification for this MBE machine. For continuous wafer rotation, gradient resulting from the chamber geometry is significantly suppressed, but a gradient resulting from the cell is present. During this work, two Al cells were used, the first cell had small quadratic gradient with a linear slope of 0.5%/cm, while the second cell had significant quadratic gradient with a linear slope 3.3%/cm as deduced from the energy gradient of upper polariton branch over the wafer shown in Fig. 1.5b). This gradient results from the Al cell gradient while Ga cell had negligible gradient what was deduced from the spatially invariant PL from InGaAs/GaAs quantum wells, Ga cell uniformity was better than 1% over the 3-inch wafer. Concluding, the thickness gradient resulting from the cell depends on the individual parameters of the cell and needs to be calibrated prior to the growth.

For the MBE growth of quantum wells, gradient of the well width over the wafer is undesirable and these structures are grown with continuous wafer rotation. For microcavity samples, gradient is desirable as it provides cavity mode wavelength tuning over the wafer such that the resonance with an exciton can be reached and both negative $\omega_{cav} < \omega_X$ and positive detunings $\omega_{cav} > \omega_X$ are present, see Fig. 1.5b).

Additional consideration on microcavity thickness gradient. Cavity thickness gradient over the laser spot should be less than the mode linewidth to avoid inhomogeneous broadening of the mode [34]. Taking designed linewidth of 7μeV and using laser spot of 50μm diameter on the sample, required cavity gradient is 0.14meV/mm what gives 10 meV tuning range over the 3-inch wafer. We compromised between inhomogeneous broadening and achievable tuning range within a wafer such that designed cavities with long photon lifetime have wedge of 0.6meV/mm.

1.3 MICROCAVITY POLARITONS RESEARCH TRENDS

When we trace the amount of journal articles reporting work on polaritons in microcavities over last 20 years, we observe constant growth since the key paper from C.Weisbuch [1] in 1992, see Fig. 1.6. In 2011, 73 articles about microcavity polaritons were published. Journals with maximum number of published work are Physical Review B, Physical Review Letters, and Applied Physics. The research centers which contributed most work during this period were Ecole Polytechnique Federale Lausanne (Switzerland), University of Southampton (UK), University Blaise Pascal (France).

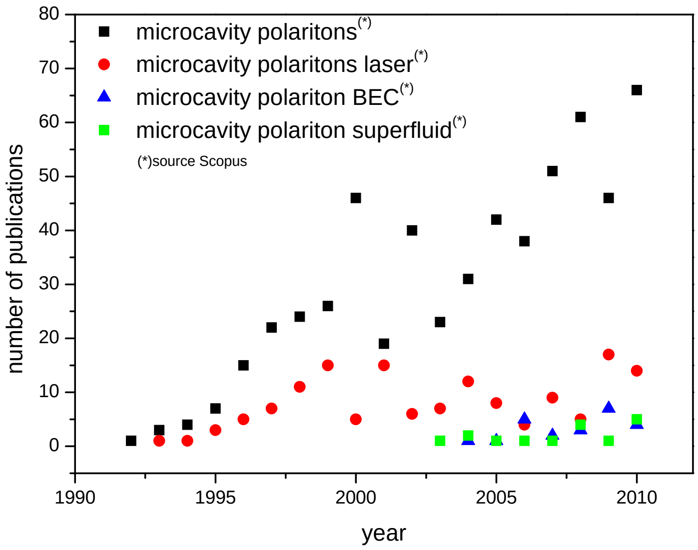

Figure 1.6: Literature on polaritons in microcavities over last 20 years.

From the fundamental physics, most publications are dedicated to polaritonic Bose-Einstein condensation (BEC)[2, 3] with the average of several articles per year since 2000, also many articles was published on polariton superfluid since theoretical work from Carussoto and Ciuti[35] from 2004, followed by experimental observation of superfluid by Amo[6] in 2009. The polaritonic applications are revisited in Ref. [7], most significant contributions include work on polaritonic lasers with several publications per year since 1994, other devices explore spin properties of cavity polaritons and multistability. Newly emerging research fields are dedicated to microcavity polaritons in ZnO and GaN based structures since 2004 with several publications per year[25]. Moreover, field of zero-dimensional polaritons resulting from a coupling between QD and micropillar cavities is emerging since 2001 with several publications per year[36]. Most recently, since 2008, there is also a research dedicated to plasmon-polariton with several publications per year[37].

2 EXPERIMENTAL METHODS

During this work, we have used several experimental techniques in order to study different properties of microcavity polaritons. Primary experimental technique was the low temperature optical imaging spectroscopy which is discussed firstly. We have been constantly developing the optical setup in order to accommodate new functionalities needed in different experiments. In this Chapter, the building blocks of this setups are described while detailed experimental conditions used in particular experiments are given in the relevant Chapters. Further to this, in collaboration with the Chemistry department in Cardiff University, we developed and used chemical etching procedures to study dislocations in microcavity samples. Moreover, we employed field-emission scanning electron microscopy (FESEM) combined with differential interference contrast (DIC) microscopy techniques to study surface properties of structural defects in microcavities, refereed as point-like-defect (PDs). Furthermore, in order to study 3-dimensional properties of PDs, in collaboration with the London Centre for Nanotechnology in University College London, we used FESEM/focused ion beam (FIB) machine. We also developed antireflection coating for microcavity samples in collaboration with the clean-room staff in Physics Department in Cardiff University.

2.1 SAMPLE PREPARATION

Microcavity samples were grown on 2- and 3-inch GaAs wafers. Wafers were cleaved along natural cleavage direction namely, big flat (110) plane of the wafer and small flat $(1\bar{1}0)$ plane of the wafer in pieces 5 x 10 mm with 10 mm along the big flat using a diamond knife. A three-inch wafer was cut into 7 pieces excluding edges which were overshadowed by the sample mount during the MBE growth. In order to avoid contaminations of the samples, they were cleaved in the clean-room, handled with tweezers and stored in secured boxes. If the sample surface was contaminated, it was cleaned using a four stages cleaning procedure, namely, it was successively immersed in trichloro-ethane, acetone, methanol and isopropanol at 80°C for 5 minutes, followed by a dip in deoxidizing 5% solution of ammonia in water at room temperature for 30 seconds. The resulting surface was assessed using an optical microscope and SEM.

2.2 Optical imaging spectroscopy setup

Table cover: The L-shaped optical table is covered with PVC frame, constructed as a part of this work, in order to isolate the optical setup from environmental influences (temperature gradient, air flow, dust, contaminations) and maintain laser safety. Table cover is mounted and supported by an aluminium frame and PVC side bars. Dimension of the frame was carefully designed to cover full table except cryostat as shown on Fig. 2.1.

Figure 2.1: Optical table cover, on the left, open, on the right, closed.

2.2.1 Low temperature measurements

The optical measurements on polaritons were conducted in the Cryovac KONTI IT Spectro 4 *bath cryostat*. The cryostat consists of a central sample chamber, a helium tank, a nitrogen shield, and the most outer vacuum shield. Helium or nitrogen liquids from the helium tank enter the sample chamber through manually regulated needle valve, they are vaporized on the heat exchanger maintaining the set-point temperature inside the chamber. The sample chamber is pumped by a membrane pump providing required cooling efficiency, pumping speed is adjusted electronically. Temperature inside the chamber is monitored using Si diodes on the sample holder and on the heat exchanger. Vacuum shield is evacuated using two stage pumping system which consist of a membrane and a turbo pump to a pressure of 10^{-6} mbar to ensure thermal isolation of liquid gasses. Worsening of the vacuum indicates a leak between shields and vacuum, most likely due to wear of the sealing due to thermal expansion during thermal cycles of the cryostat windows, the sealing is made of In wires.

2.2.2 EXCITATION

2.2.2.1 Lasers

We used two lasers in different *optical excitation configurations.* Firslty, a mode-locked Ti:Sapphire laser was used. The laser system consists of a solid state Verdi V5 laser which pumps an ultrafast Mira 900F laser, made by the manufacturer Coherent. The Verdi is a solid state laser with the Nd:YVO4 crystal as the active medium. The Nd:YVO4 is pumped by high power semiconductor diodes at the common pump wavelength of about 800 nm, and emits at 1064 nm. This frequency is doubled giving emission at 532 nm by the second harmonic generation in lithium triborate (LBO) crystal. The laser output power is 5 W. Verdi pumps a Titanium sapphire crystal in the Mira oscillator. The Mira output is tunable between 710 and 1000 nm, it works in CW and pulse modes, laser polarization is horizontal. The pulse mode was used in our experiments with pulse duration of 100 fs and 76 MHz repetition rate. Stability of the output power of the Mira is given by manufacturer as 3% or better. The FWHM of the spectral width of the signal is 20 meV.

Secondly, a single-mode external cavity diode laser (Sacher Lynx) was employed to excite polaritons with well-defined energy. The nominal lasing mode linewidth is 20 neV (5 MHz), 100 times weaker is a broadband amplified spontaneous emission (ASE) with a spectral width of 50 meV [38]. The wavelength of this continuous wave (CW) laser is tuneable from 795.7 to 853.1 nm, as specified by the manufacturer [38]. Wavelength tuning is realized by tilting the grating inside the laser cavity, what can be made manually for a coarse wavelength tuning, and using piezoactuator for a fine wavelength tuning. The laser output power was 110 mW at the maximum driving current of 250 mA for the 810 nm wavelength. Laser output is s-polarized(vertical). The spatial intensity distribution of the laser beam was elliptical and had to be compensated with cylindrical lens, see discussion on the beam compensation in Sec. 2.2.2.1.1.

Microcavity samples resonance wavelength was centered around 850 nm and we worked with IR viewers, IR sensitive cards and IR USB cameras in order to align optical setup.

2.2.2.1.1 Ellipticity compensation The CW diode laser has elliptical beam with horizontal to vertical size ratio $\frac{1.3\,\mathrm{mm}}{2.9\,\mathrm{mm}}$ at the distance of 1.67m from the laser head. To compensate for the beam ellipticity, we used a cylindrical lens. In order to calculatethe required focal length L_C of the cylindrical lens, we used the Gaussian beam approximation.

$$E(r,z) = E_0 \frac{w_0}{w(z)} exp\left(\frac{-r^2}{w^2(z)}\right) exp\left(-ikz - ik\frac{r^2}{2R(z)} + i\zeta(z)\right) \tag{2.1}$$

where r is a radial distance from the center axis of the beam, z is an axial distance from a beam waist, w_0 is the beam size, $w(z) = w_0\sqrt{1+(\frac{z}{z_R})^2}$, where the Rayleigh length $z_R = \frac{\pi w_0^2}{\lambda}$, is a spot size[1], $R(z) = z[1+(\frac{z_R}{z})^2]$ is a radius of curvature, $\zeta(z)$ is the Gouy phase shift.

The position z' along the beam propagation axis where vertical and horizontal beam waists are equal is calculated as

$$w_{0_H}\sqrt{1+\left(\frac{z'+\Delta}{z_{R_H}}\right)} = w_{0_V}\sqrt{1+\left(\frac{z'}{z_{R_V}}\right)} \tag{2.2}$$

where $\Delta = z(w_{0_H}) - z(w_{0_V})$ is a relative distance between horizontal and vertical waists.

Cylindrical lens is placed at z', and it transforms the radius of curvature of the first beam in the radius of the second beam, which is calculated from the formula on the complex Gaussian beam radius:

$$\frac{1}{q_{OUT}} = \frac{1}{q_{IN}} - \frac{1}{f}, \text{ where } \frac{1}{q_{OUT}} = \frac{1}{R(z)} - i\frac{\lambda}{\pi \cdot w^2} \tag{2.3}$$

from where, for equal waists we get

$$\frac{1}{R_{OUT}} = \frac{1}{R_{IN}} - \frac{1}{L_C} \text{ for } z' = z(w_{0_H} = w_{0_V}) \tag{2.4}$$

Calculated focal length of cylindrical lens was $L_C = 1128\,\text{mm}$, the closest available match was $L_C = 1000\,\text{mm}$, beam quality after compensation is shown in Sec. 5.5.1.

2.2.2.2 Dual lens holder

A dual lens holder was designed by the author in order to accommodate two high numerical aperture(NA) (0.5), 8mm focal length (6 mm working distance) lenses inside the sample chamber in the cryostat for coupling from both sides of the sample, and focus adjustment of the lenses at low temperature. Dual lens holder assembly is mounted onto the existing sample holder frame, for detailed sketches of this design

---

[1] Spot size is defined here as $I(\pm z_R) = \frac{1}{e^2}$ for normalized intensity

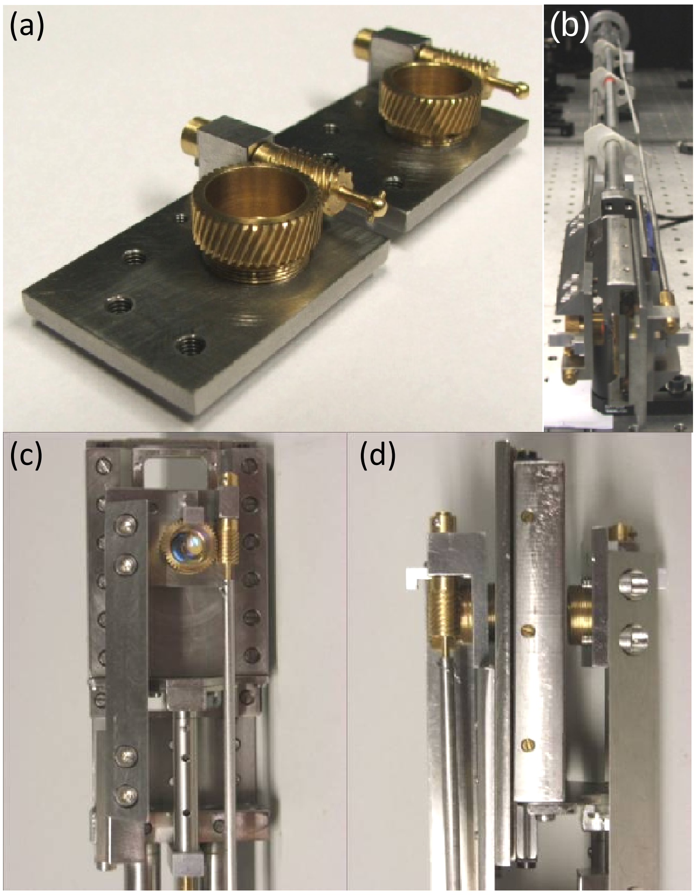

Figure 2.2: Dual lens holder, in a) worm wheel assembly, in b) sample holder inset, in c) and d) dual lens holder mounted on the sample holder frame, the front and side view respectively.

see Appendix A. Fine focusing of the lens is achieved by placing it inside a worm-wheel and driving with worm. One rotation of the worm-wheel moves lens by 0.5mm[2] ensuring overall focusing adjustment range of 5 mm. The worm-wheel is supported by an aluminium plate. Assembled worm and worm-wheel is shown on Fig. 2.2a). Bars, driving worms, are guided using feed-throughouts outside the cryostat. Assembled dual lens holder is shown on Fig. 2.2c) and d), view from the top and from the side respectively. Worm and worm-wheel were manufactured from brass to match their thermal expansion coefficients in low temperatures[39] and because brass has a self-lubrication effect (contains a soft metal), remaining parts were manufactured from stainless steel and aluminium, compare sketches in Appendix A. The small parts were manufactured in the departmental workshop, while worms and worm-wheels were fabricated externally using computer numerical controlled (CNC) processing machine in

---

[2] 0.5 mm is a tread size of the worm-wheel.

order to achieve high accuracy of processing. Moreover, a silicon temperature sensor was installed on the holder 1 cm away from the sample in order to monitor temperature inside the sample chamber, it has a temperature range between 1.5 and 500 K.

2.2.2.3 Acousto-optic modulator

In order to avoid sample heating for the experiment on parametric scattering of polaritons described in Chap. 5, the excitation was digitally modulated by an acousto-optic modulator providing pulses with 10 kHz frequency and 1% duty cycle resulting in 1 μs pulse duration. AOMs used here are from Intraaction. The ME-792E modulator driver with crystal oscillator frequency 79MHz and RF power capability of 2 Watts was used with pulse laser, while the ME-802E modulator driver with crystal oscillator frequency 80MHz and the same output power was used with the CW laser. AOMs have digital and analog inputs both of which were used here for the RF laser modulation. Digital input was taken from PC through Data Acquisition (DAQ) board and controlled by software interface written in LabWindows for the purpose of this work, software provides duty cycle adjustment between 0 and 100% in steps of 1%. The DAQ board was used as it ensures fast switching with frequency up to 100 kHz, for higher frequencies transit times are visible on the pulse trace on the oscilloscope, namely, transit times at 1MHz frequency were resolved as $\simeq 0.1\,\mu$s. DAQ board was connected with the AOM driver via the impedance matched chip SN74128 designed for high frequencies. AOM's analog input was driven from Lock-In Amplifier SR844 from Stanford Research which acted as a function generator with a static wavefront in order to provide an amplitude modulation of the RF wave. All electrical connections between elements described above were impedance matched to the input impedance of AOM, which was 50Ω, to avoid electro-magnetic reflections.

2.2.3 Detection

The emission from a microcavity was detected spectrally integrated in real or reciprocal space using video CCD Sony cameras 620E and 340E, called CCD/NF for the near-field camera and CCD/FF for the far-field camera in Fig. 2.3. The DCR-TRV series from Sony gives optical zoom of 25x, and uses a 1/6-inch CCD chip as detector. It has a night-shot (IR sensitive), and super-night-shot (extended exposure times) mode for high sensitivity imaging.

For spectrally resolved detection, two spectrometers were used. We used the Horiba Jobin-Yvon iHR 550 imaging spectrometer with three gratings of 150, 600 and 1800

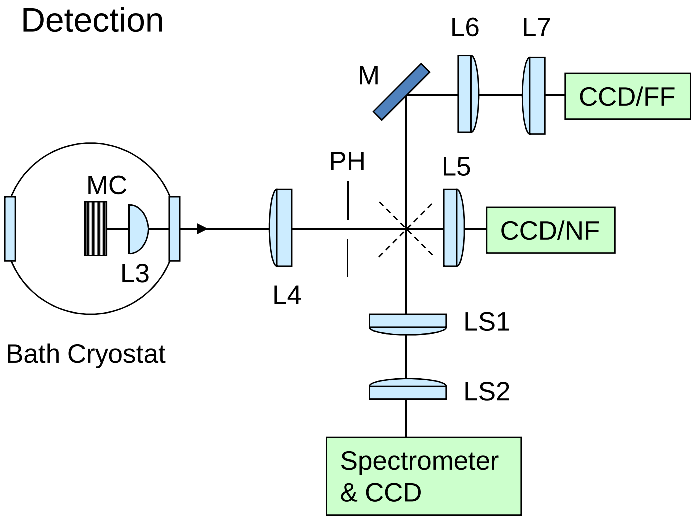

Figure 2.3: Detection setup, L-lens, MC-microcavity sample in a bath cryostat, PH-pin-hole, M-mirror, LS1,LS2-lenses on transition stages, FF-far-field plane image, NF-near-field plane image.

grooves/mm providing resolution of 0.72, 0.18, and 0.06 nm respectively, blazed at 500 nm the first one, at 450-850 nm for the later two. The architecture of the spectrometer is the Czerny-Turner type with focal length of 550 mm. This spectrometer worked with the Roper Andor CCD with 1600 x 400 pixels array, pixel size 16 μm x 16 μm. Camera was air cooled down to T=-80°C.

2.2.3.1 IRIS spectrometer

The emission was imaged in real or reciprocal space into the input slit of an *imaging spectrometer* which was designed and built by Wolfgang Langbein and Stephan Schneider[40], it is called the IRIS spectrometer, designated 'Spectrometer' in Fig. 2.3. This is a high resolution grating spectrometer in Littrow configuration[3]. Spectrometer consist of a long focal length lens, $f = 1900$ mm, which images the input slit of the spectrometer onto the Roper Scientific PIXIS:100BR Spectroscopy CCD-camera with chip consisting of 1340-100(horizontal-vertical) pixels, pixel size 20 μm x 20 μm. Spectrometer grating is 1200 grooves/mm blazed at 1 μm from the Jobin Ivon. Maximum aperture opening is 120 mm. Considering the finite width b of the entrance slit, spectrometer resolution is calculated using diffraction theory as[**?**]

$$\Delta\lambda = (f\lambda/a + b)\frac{d\lambda}{dx} \tag{2.5}$$

---

[3] The Littrow configuration meaning that light reflected from the grating propagate back into the same direction as incident light such that Littrow-grating acts as wavelength selective reflector.

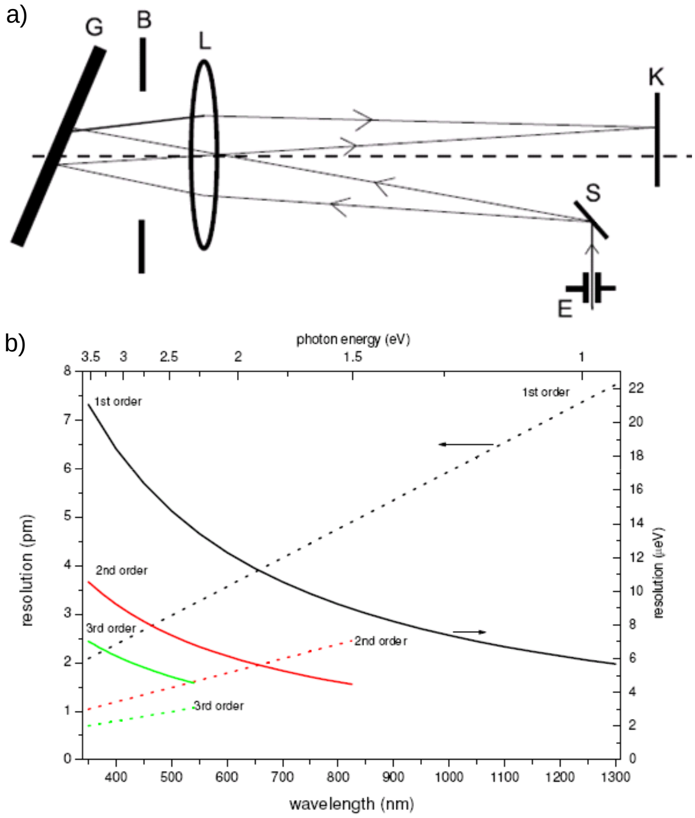

Figure 2.4: In a), sketch of the IRIS spectrometer design, E entrance slit, S reflecting mirror, G grating, B aperture, L lens, K CCD camera. In b), energy and wavelength dispersion inside spectrometer, after Ref. [40].

where f is the focal length of the lens, a is the aperture size, b is the width of the slit, $d\lambda/dx$ is a linear dispersion of a spectrometer. Taking experimental values $a = 120\,\mathrm{mm}$, $b = 30\,\mu\mathrm{m}$, $d\lambda/dx$ measured as 5.8 pm/mm for 800 nm, we obtain $\Delta\lambda = 3\,\mathrm{pm}$ or $8\,\mu\mathrm{eV}$, compare with Fig. 2.4b). This does not account for abberation errors, from detailed analysis, spectrometer response line-shape was deduced as Voigt function with $18\,\mu\mathrm{m}$ Gaussian and Lorenzian FWHM each, see Sec. 3.4.1 for details.

2.2.3.2 2-dimensional spectrally resolved imaging

Real $I(x, y, \omega)$ and reciprocal $I(k_x, k_y, \omega)$ space transmission spectra were recorded using two different lens sets, LS1 and LS2 on Fig. 2.3, which imaged PH plane onto the entrance slit and the grating of the IRIS spectrometer. Two-dimensional images were acquired by translating the image across the spectrometer slit using lateral movements of two lenses. The position and movement of the optical elements were calculated using the transfer matrix formalism for paraxial rays after [41, 42]. In this formalism, a ray of light is represented by a vector l with two components, the distance r from the optical axis, and the angle α relative to the optical axis. The optical elements are described by 2 x 2 matrices (M). In particular, lens with focal length f, distance d in free space between elements are represented as

$$M_f = \begin{pmatrix} 1 & 0 \\ -1/f & 1 \end{pmatrix}, M_d = \begin{pmatrix} 1 & d \\ 0 & 1 \end{pmatrix} \tag{2.6}$$

Light ray transformed by the optical elements is found as $l' = [r'; \alpha] = M_n....M_2M_1l$ with M_1 being a matrix of the first element. Conditions used for the near field (NF, real space) imaging was such that the position on the sample was imaged onto the input slit of the spectrometer while direction on the sample was imaged onto the spectrometer grating. In order to satisfy the first of these conditions, real space component of the image r' on the entrance slit has to be independent from the angular component α of the object. On the other hand, in order to image the far field of the sample (FF, directional space) onto the the input slit of the spectrometer, the real space component of the image r' has to be independent from the real space component r of the object. If both from above conditions are satisfied, imaging of the position and direction is made simultaneously and the configuration is called 4f, it is used in order to translate unchanged image of the object over a distance. Analogous conditions have to be satisfied for NF or FF imaging onto the grating. In order to translate the image across the entrance slit of the spectrometer, synchronized movement of two lenses LS1 and LS2 need to be made. The lenses are translated by s_1,s_2, the translated image is defined as $l' = M_f l + [0; s/f]$ where s_1,s_2 are calculated from the condition that the image of the object on the detector's aperture does not depend on s_1,s_2. In order to ensure translation of the lenses, they are placed on the translation stages driven by the stepper motors through computer interface program.
Resolution of scans discussed in this work is in order of 0.5 μm (real space) and 0.05 μm^{-1} (reciprocal space).

2.3 CHEMICAL ETCHING

Techniques used to reveal dislocations can be categorized into thin films methods such as chemical etching[23, 43], transmission electron microscopy (TEM)[44], scanning electron microscopy (SEM)[45], and bulk methods, such as decoration[44], X-ray diffraction[44], optical birefringence[46], and photoluminescence[47].
We employed chemical etching and polarization measurements. For the latter, dislocations are visible due to induced birefringence around TD[46]. The setup used in

this experiment was a modified version of the setup shown on Fig. 3.1 extended by two $\lambda/2$ plates in excitation and detection, in order to introduce a phase shift of the linearly polarized laser, and analyzer in detection. We measured the QW sample at nitrogen temperature. However, high density of misfit dislocations along $[1\bar{1}0]$ and [110] directions dominated light polarization from the structure, and no threading dislocation induced birefringence was observed.

Chemical etching reveals dislocations by enhanced material removal around a threading dislocation core. This is a consequence of impurity atoms present at the dislocation which changes its chemical composition and reactivity as compared to the surroundings. The advantage of this method is that it requires less equipment and sample preparation as compared to the alternative method of TEM. It also allows to investigate large surface areas, which is necessary considering the small defect density. It also gives the one-to-one correspondence between etched pits and treading dislocations. In order to investigate if the observed PD are related to threading dislocations, we used an etching procedure [43, 48]. Since the sample is not destroyed in the process, it is possible to spatially correlate the etched pits corresponding to the treading dislocations with the PDs. Prior to etching, the sample surface is cleaned by successively immersing in trichloroethane, acetone, methanol and isopropanol at 80°C for 5 minutes, followed by a dip in deoxidizing 5% solution of ammonia in water at room temperature for 30 seconds. The resulting surface was assessed using an optical microscope and SEM. The KOH etch was prepared from granules which were melted in a test tube under open flame. To avoid cool down and recrystallization of the etchant, the baker with the KOH etch was placed on the hotplate heated to 360°C. The temperature was monitored using a thermocouple. Sample was kept inside the molten KOH etch for 2 minutes. The etched pits were counted using a reflective optical microscope.

We also measured TDs propagation inside epilayer using *selective etching*. In order to selectively remove GaAs and AlAs layers, two etchants were prepared as described in Ref. [48]. Prior to etching, samples were cleaned in four solvents and ammonia solution as described above. GaAs etchant consisted of citric acid and hydrogen peroxide in 4:1 ratio, it removes GaAs with a rate greater than 4000 Å/min while AlAs with the rate less than 3 Å/min at room temperature. AlAs etchant consisted of phosphoric acid, hydrogen peroxide and water in a 3:1:50 ratio. It etches GaAs at 800 Å/min, and AlAs at a rate greater than 16000 Å/min. The etching of layers was timed according to Ref.[48], and assessed visually, as due to the broadband absorption, a GaAs layer is metallic, while a AlAs layer is blueish. After selective etching of several GaAs/AlAs double $\lambda/4$ layers with overall thickness higher than 2μm [49], KOH etching was repeated.

2.4 DIFFERENTIAL INTERFERENCE CONTRAST MICROSCOPY

Differential interference contrast microscopy (DIC), also know as Nomarski microscopy, is a bright field microscopy technique which exploits a difference in reflective indexes between specimen and its environment. For DIC used in transmission, the optical assembly consist of two polarizers and two Nomarski filters. Light from a Tungsten lamp is linearly polarized and transmitted through the first Nomarski prism, made of birefringent material, which separates ordinary and extra-ordinary rays into two beams and displaces them vertically (in the plane perpendicular to the sample plane, position axis in Fig. 2.5) by a shear displacement Δ. After passing through the specimen, beams are recombined in the second Nomarski prism and pass through the second polarizer which is orthogonal to the first one in order to remove directly transmitted light.

In this experiment, DIC in reflection was used. A Nomarski prism assembly (DIC Slider U-DICT with Polarizer U-ANT) is mounted in an Olympus BX-50 upright microscope which provides Köhler illumination[4] from a mercury arc lamp filtered using a green filter and further split by the Normarski prism into two beams 1,2 shifted by the shear displacement $\mathbf{\Delta}$ in the object plane, with linear polarizations along and orthogonal to $\mathbf{\Delta}$. The reflected beams are recombined by the same prism, creating a polarization state depending on their relative phase $\varphi_1-\varphi_2$. The transmission through the polarizer depends on the polarization state, such that the intensity depends on the relative phase in the way

$$2I_{\mathrm{DIC}} = I\left(1 - \cos\left(\phi_{\mathrm{o}} + \varphi_1 - \varphi_2\right)\right) \tag{2.7}$$

where the offset phase ϕ_{o} is introduced by an adjustable spatial offset of the Normarski prism along the optical axis from its nominal position for which the beams are not displaced in the directional space (objective back focal plane). The shear $\mathbf{\Delta}$ is similar to the optical resolution of the microscope objective, which allows to approximate the phase difference between the two beams in first order as the shear times the phase

---

[4] Köhler illumination provides a homogenous sample illumination and prohibits the light source image formation on the sample. Köhler illumination requires a high intensity illumination source, collector lenses, an adjustable field diaphragm, a condenser diaphragm, and condenser lenses in order to illuminate sample, field diaphragm and condenser diaphragm regulate the size and intensity of the illumination spot on the specimen, respectively.

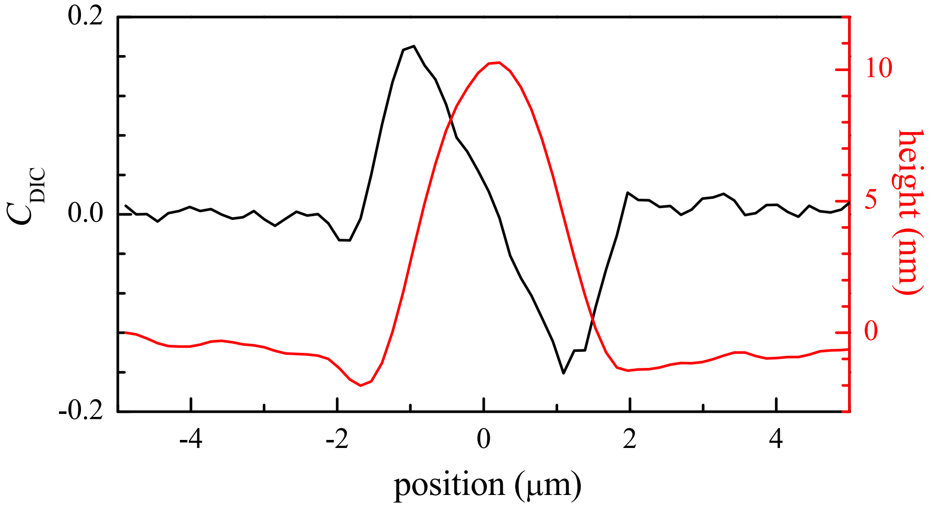

Figure 2.5: DIC contrast $C_{\rm DIC}$ (black line) as function of the sample position s along the shear direction, and resulting height profile h (red line) calculated using Eq.(2.9).

gradient at the observed position, $\varphi_1 - \varphi_2 \approx \mathbf{\Delta} \cdot \nabla\varphi$, such that Eq.(2.7) can be written as $2I_{\rm DIC} = I\,(1 - \cos{(\phi_{\rm o} + \mathbf{\Delta} \cdot \nabla\varphi)})$. Choosing $\phi_{\rm o} = \pm\pi/2$, and developing up to first order in the phase difference, we get $2I^{\pm}_{\rm DIC} = I\,(1 \pm \mathbf{\Delta} \cdot \nabla\varphi)$. Measuring $I_{\rm DIC}$ for both offset phases, we determine the contrast

$$C_{\rm DIC} = \frac{I^{+}_{\rm DIC} - I^{-}_{\rm DIC}}{I^{+}_{\rm DIC} + I^{-}_{\rm DIC}} = \mathbf{\Delta} \cdot \nabla\varphi \tag{2.8}$$

We can now integrate the contrast along the shear direction to retrieve the phase φ. In reflection, the phase is related to the surface height h by $\varphi = 4\pi h/\lambda$ with the wavelength λ of the light, such that we arrive at

$$h(s) = \frac{\lambda}{4\pi|\mathbf{\Delta}|}\int_0^s C_{\rm DIC} ds' \tag{2.9}$$

where s denotes the position in the sample plane along the direction of the shear $\mathbf{\Delta}$. We assumed here that sample is not birefringent and that the phase shift of the reflected light is given by the height of the sample surface only, neglecting internal interfaces. The latter is justified as the green light is absorbed strongly by the structure. The height $h(s)$ was determined using Eq.(2.9) with s along the direction of the shear $\mathbf{\Delta}$. In the measurements presented in this work we used a UplanFL 20x/0.5NA objective, for which the shear was determined to be $|\mathbf{\Delta}| = 0.55\,\mu$m using a calibration slide in transmission DIC consisting of a PMMA pattern of a 200 nm thickness on a glass coverslip, in which case the phase is given by $\varphi = 2\pi h(n_1 - n_2)$ with the refractive index difference $n_1 - n_2 = 0.48$ between PMMA and air. To compensate for systematic errors, the measured C_{DIC} across the center of the defect was corrected by the C_{DIC} along a line displaced perpendicular to the shear, just outside of the defect. An examples of a measured C_{DIC} and the resulting height profile $h(s)$ for defect PD4 are shown in Fig. 2.5.

2.5 DUAL FIB/FESEM MACHINE FOR VOLUME IMAGING

To investigate the sample structure below the surface, we used a Carl Zeiss XB1540 Cross-Beam focussed-ion-beam (FIB) microscope which combines an ion-beam milling/ imaging column with field-emission scanning electron microscope (FESEM) [50], providing an imaging resolution of about 50 nm for the samples studied. This system operates in ultra-high vacuum in order to avoid contamination of the source, and to prevent electrical discharge in the high voltage column. Ions extracted from the liquid Ga source are accelerated in the high voltage column ($5-50$ kV), and focused by electromagnetic lenses through the set of apertures. Beam shaping provides beams with currents between several pA and 30 nA. When Ga^+ hits the surface of the specimen, different species are generated including sputtered atoms and molecules, secondary electrons (SE), and secondary ions (SI). For imaging, secondary electrons or ions are used. Secondary electrons provide images with good depth of field, while ions penetration length for maximum applied voltages of 30-50 keV will be limited to few nanometers. The bombardment of charged species onto the surface of an insulator can result in a distortion of the image due to charging effects. Charged regions will appear black when imaged with secondary electrons, as electrons will be deflected from the surface and do not reach detector. In order to minimize charging, samples are coated with a thin metal layer, e.g. Au, Cr.

2.6 ANTIREFLECTION COATING

In order to minimize back-reflection on the interface between air $n_1 = 1$ and the GaAs wafer $n_3 = 3.6$, we developed antireflection coating. Material for coating was chosen such that its refractive index satisfies the Fresnel formula $n_2 = \sqrt{n_1 n_3} = 1.9$. Hafnium dioxide was used for the coating, its refractive index is written using the

Sellmeier formula

$$n^2(\lambda(nm)) = 1 + \frac{B_1\lambda^2}{\lambda^2 - C_1} + \frac{B_2\lambda^2}{\lambda^2 - C_2} + \frac{B_3\lambda^2}{\lambda^2 - C_3} \tag{2.10}$$

with parameters deduced as $B_1 = 1$, $B_2 = 0.85$, $B_3 = 0.82$, $C_1 = 21367$, $C_1 = 20000$, $C_1 = 1000$ [51]. From Eq.(2.10), the refractive index of hafnium dioxide at 850 nm was calculated as $n_2 = 1.93$. Hafnium dioxide coating was deposited on the sample by thermal evaporation in the Edward Auto 306 electron-beam(EB) evaporator. We used HfO_2 powder with purity $> 99,8\%$ from the company GfE Nürnberg. In the electron-beam evaporators, the material for the coating is sputtered from the crucible due to the bombardment with high energy electrons (3 kW) emitted by a tungsten filament and focused by electromagnetic lenses [52]. The thickness L of the deposited coating layer is controlled by a quartz balance detector. Evaporation takes place under the pressure of 10^{-6} bar with the evaporator's bell-jar pumped down by a diffusion pump with oil as the active medium. Evaporation of a HfO_2 layer of thickness $\lambda_{cav}/4 \simeq 230$nm takes 30 min.

In order to calibrate the deposition rate, firstly, hafnium dioxide was deposited onto a microscope glass slides. The thickness of the deposited layer was measured using the surface profilometer Dectac[53], and white light reflectometry. Dectac profilometer measures a surface thickness profile using a diamond stylus with 12.5 μm radius, a surface area imaged during one measurement is in the range of 10 to 50 μm with a vertical resolution specified by the manufacturer as 1 nm. Results obtained using a Dectac profilometer are combined with white light reflectometry which utilize the interference principle between the white light beam reflected from the surface of an investigated coating layer and reference beam reflected from the mirror, the two beams have a relative phase shift of $\varphi = \frac{2\pi}{knh}$, where $n \cdot h$ is an optical path difference, they are described by Fresnel equations for the reflection on multiple interfaces[21]

$$R = |r^2| \text{ where } r = \frac{r_{12} + r_{23}e^{2i\beta}}{1 + r_{12}r_{23}e^{2i\beta}} \tag{2.11}$$

where $r_{ij} = \frac{n_i cos\theta_i - n_j cos\theta_j}{n_i cos\theta_i + n_j cos\theta_j}$, $\beta = \frac{2\pi}{\lambda_0} n_2 h cos\theta_2$, $n_{1,2,3}$ are as defined above, $\theta_{1,2,3}$ are angles of incidence for materials $1, 2, 3$ which were air, coating layer, and glass slide. Spectrally resolved interference was recorded by the spectrometer USB2000/Ocean Optics with 10nm resolution, and a wavelength range between 200 and 1100nm. Fit was made in the following steps, firstly, spectrometer response was deconvoluted from the data and a Gaussian response was convoluted, in order to remove the tails of the response. Secondly, data is divided by the reference signal, finally, fit with Eq.(2.11)

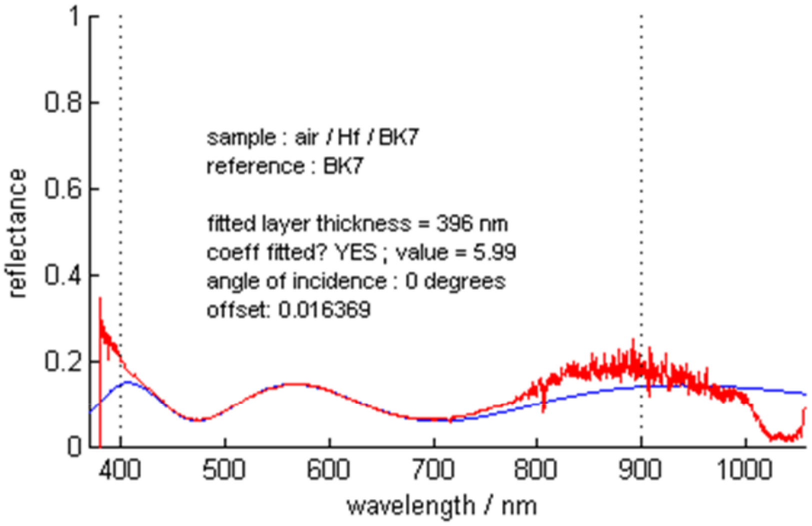

Figure 2.6: Data measured with white light reflectometry, red line, data fitted using Eq.(2.11) in red.

is done using thickness, initialized by the value measured with Dectac profilometer. Example of a fitted data is shown in Fig. 2.6. Reflective index of a thin film is lower than for a bulk material, and it was found here as $n_2 = 1.75$.

In order to improve the control over the growth and the quality of the coating, we studied the influence of a substrate temperature[54] and oxygen pressure on the Hafnium coating properties[55]. In general, after Ref.[56], refractive index of HfO_2 thin film increases with the substrate temperature and decreases with the oxygen pressure. However, this study was not conclusive as a cleanroom technician co-conducting the project could not commit more time to this project.

2.7 OTHER TECHNIQUES

Also atomic force microscopy images of the surface were obtained using Digital Instruments/Nanoscope SPM system in the collaboration with Nanophysics group in Cardiff University, some of these results will be discussed in Chap. 3

3 POINT-LIKE DEFECTS

Optical disorder in MBE grown GaAs based microcavities is typically dominated by point-like defects (PDs) and a cross-hatch dislocation pattern. PDs are discussed in the following chapter for two microcavity samples MC1 and MC2. Chapter is organized as follows. Firstly, in Sec. 3.1, an overview of defects and mechanisms of their formation will be presented. Secondly, in Sec. 3.1, details on experimental techniques will be discussed followed by the description of the investigated samples in Sec. 3.3. Further to this, in Sec. 3.4.1, results of an optical investigation on the sample MC1 will be presented followed by optical, surface and structural data on samples MC1 and MC2 together with results of the simulations in Sec. 3.4.2. In the end of sec 3.4.2 we discuss the 3-dimensional volume reconstruction of PDs in Sec 3.4.2.4 and growth kinetics in Sec 3.4.2.5. Finally, a summary will be given in Sec. 3.5.

3.1 INTRODUCTION

Point-like defects (PD) are commonly observed in GaAs based MBE grown microcavities with a surface density of about $10^4/\mathrm{cm}^2$ and sizes and shapes typical of those ascribed to oval defects [57]. These defects produce rather extended surface modulations. Polariton modes in MCs have typical extensions of 10 micrometers, limited by mirror transmission[1] or residual disorder. These modes are therefore sensitive to the lateral inhomogeneities in the length-scale of 1-100 micrometer, making an excellent probe for structure quality. The resonant local transmission of the MC is modified by the PDs and spatially confined cavity modes are created, typically visible as a series of spectrally narrow localized modes, as will be shown here. Point-like-defects observed in MBE-grown GaAs based heterostructures are classified into several types, with the most common type being oval defects. According to Ref [58, 59], oval defects

---

[1] Due to total internal reflection, polariton wavevectors coupled radiatively are $\mathbf{k} \leq 7.4/\mu\mathrm{m}$ for GaAs cavity with AlAs/GaAS DBRs, while $\mathbf{k} > 7.4/\mu\mathrm{m}$ are guided modes.

originate from an excess of Ga, Ga droplets, or surface contamination. Furthermore, low growth temperatures as reported in Ref. [60, 61] can lead to their formation. Oval defects were extensively studied in the 1990s as they were responsible for the failure of electronic devices, for example field-effect transistors [58]. These defects have typical sizes in the order of several μm and a roughly 3:1 aspect ratio along the $[1\bar{1}0]$:[110] crystal directions [59]. Their height on the surface were found to be several tens of nanometers. We observed in this work that the aspect ratio of these defects is decreasing with increasing growth temperature, producing nearly round defects of similar diameters and heights as oval defects but grown at higher wafer temperature. Round defects were previously attributed [62] to Ga oxide or effusion cell spitting. We found that both oval and round defects investigated in our work originate from a GaAs thickness modulation in an underlying GaAs layer, which we attribute to Ga droplets with sizes in the order of 100 nm emitted by the Ga source and impinging on the surface during growth.

The mechanism resulting in the presence of Ga droplets, of a size in the order of 100 nm, in the molecular beam of the source was previously ascribed [58] to an inhomogeneous temperature distribution in the Ga crucible of the source. Namely, Ga cools near the orifice of the crucible and forms droplets since it does not wet the pyrolytic Boron Nitride (PBN) crucible surface. These droplets can fall back into the liquid Ga causing a spray of secondary Ga droplets. Recommended methods to reduce this mechanism include: 1) use solid instead of liquid Ga; 2) modification of the orifice geometry of the Ga cell to inhibit condensed Ga droplets entering into the Ga source; 3) creating a positive axial temperature gradient toward the orifice to prevent condensation of Ga; 4) treating the crucible with Al, which forms a AlN layer which Ga is wetting, suppressing the formation of droplets. Another mechanism explaining the formation of an oval defect precursors is suggested in Ref [63] referred to as Ga source spitting. It was observed [63] that during heating of the Ga source up to 1200°C , within the range of Ga evaporation [57], explosions in the Ga liquid were resulting in Gallium droplets on the MBE chamber walls. It was speculated that these explosions were due to Ga_2O_3 shells encapsulating Ga which create an effusion barrier. Another possible mechanism[64] is that particulates released from the walls of the MBE chamber are entering the molten Ga in the crucible causing a turbulent reaction. Summarizing, a variety of mechanisms for the Ga nano-droplet formation have been suggested, and the specific mechanism dominating in given growth will depend on a number of factors.

3.2 SETUP

3.2.1 OPTICAL IMAGING

The measurements described in this Chapter were made with the samples held in a cryostat in nitrogen gas at $T = 80\,\mathrm{K}$ and gas pressure of 100-300 mbar. The samples were mounted strain-free on a $x - y$ mechanical translation stage. Real space $I(x, y, \omega)$ and reciprocal space $I(k_x, k_y, \omega)$ transmission spectra were taken in the low-intensity regime, here I denotes intensity and ω the optical angular frequency. A sketch of the setup used for the measurements described in Sec. 3.4.1 is shown in Fig. 3.1a).

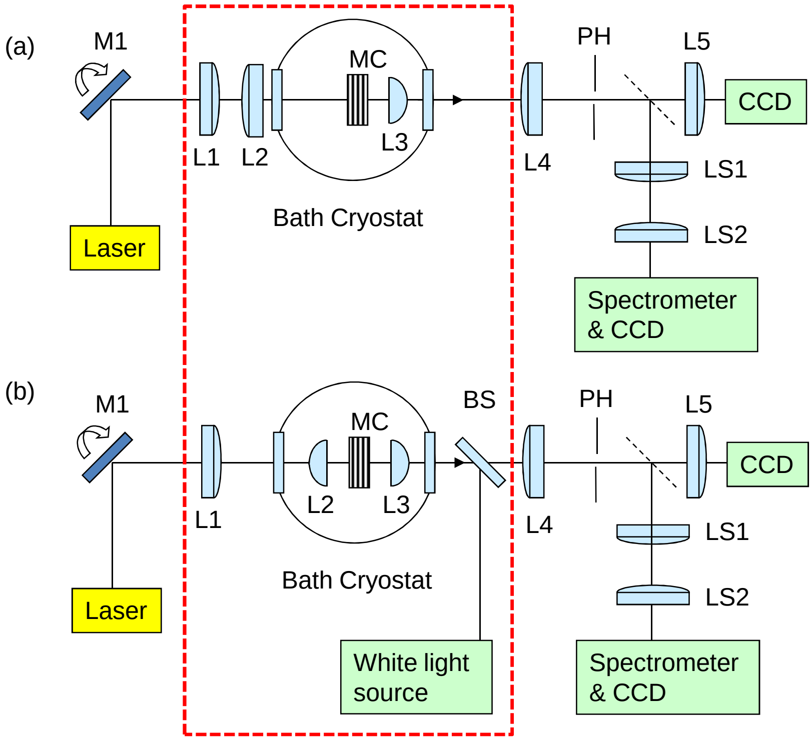

Figure 3.1: Sketch of the optical setups used to measure the localized polariton states. In (a), setup used for the measurements discussed in Sec. 3.4.1. In (b), setup with dual lens holder used for the measurements discussed in Sec. 3.4.2. L1-L5 Lenses, MC: Microcavity sample LS1,LS2 moving lenses for imaging, BS Beam splitter.

The single mode laser, compare Sec. 2.2.2.1, was used to excite the polaritons at normal incidence ($\mathbf{k} = 0$) over a large size in real space ($\sim 1\,\mathrm{mm}$) from the substrate side. The Ti:Sapphire pulse excitation was spatially focussed to a spot of about $3\,\mu\mathrm{m}$ diameter using a lens of 0.15 numerical aperture, corresponding to an excitation wavevector range of $|\mathbf{k}| < 1.1/\mu\mathrm{m}$. The emission was collected from the epi-side by an aspheric lens of 0.5 NA (L3 in Fig. 3.1) with a wavevector range of $|\mathbf{k}| < 4/\mu\mathrm{m}$, providing a spatial resolution of about 1 μm. For the measurements described in Sec. 3.4.2, the optical imaging setup was extended by the dual lens holder which accommodates two aspheric lenses of 0.5 NA mounted at opposing faces of the sample inside the cryostat to focus the excitation and collimate the emission, respectively, see Sec. 2.2.2.2. The axial positions of both lenses are controlled at low temperatures to adjust the focus of excitation and detection. Additional modification of the setup was an introduction of a white light source in order to make correlative low temperature measurements on defects. The picture of the optical setup is shown on Fig. 3.1b) with a modified part inside the red rectangular frame.

3.2.2 FIB milling and FESEM imaging

This measurements were performed in London Centre for Nanotechnology (LCN) by the author. The internal epi-layer structure was exposed by FIB milling using FIB/FESEM machine as described in Sec. 2.5. Smooth cross-sections were obtained using a two stage milling procedure. In the first step, a high ion beam current of 2 nA, was used, resulting in fast milling but leaving a rough and inhomogeneous interface due to sputtering and redeposition of the material. In the second step, the surface was polished with a lower beam current of 200 pA removing a layer of about 500 nm per cut resulting in a negligible surface roughness. In the next steps, layers with a thickness of 1 μm or less were removed using the low beam current. Different stages of this milling procedure are shown in Fig. 3.2. Before milling, the oval defect (PD3) is seen in SEM (Fig. 3.2a), with the vertical image scale corrected for the viewing angle of 36° to the sample surface. A rectangular well of about 6 μm width and 7 μm depth is milled into the surface to one side of the defect (Fig. 3.2b), exposing a cross-section through the epi-layers to be measured at its side walls. After imaging the exposed cross-section with SEM, the subsequent cross-section at a controlled distance further into the structure is milled. Steps sizes of about 1 μm were used at the outskirts of the defect, reducing down to 100 nm at its center to resolve the defect source. The cross-sections were $6 - 7\,\mu$m deep to expose the complete epitaxial structure, and their width was adjusted to the lateral extension of the defect observed at the surface. During these measurements, we used 10 kV on the SEM gun for imaging, 30 μm SEM aperture, for imaging we used secondary electrons, the vacuum chamber was at pressure of $4 \cdot 10^{-9}$ bar.

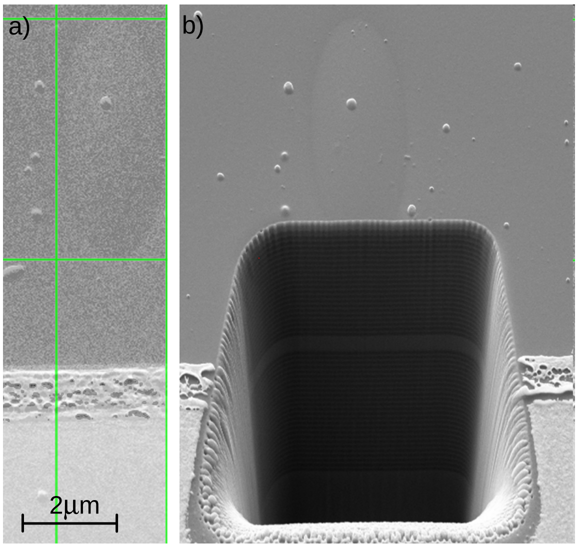

Figure 3.2: SEM images of oval defect PD3. a) prior to milling, green lines indicate defect extension on the surface. b) after milling the well exposing the epilayer cross-section at its side wall. On the lower part of the images, the edge of the alignment photomask is visible, details in text.

In order to mark defects on the sample surface for the correlative studies, a gold alignment mask was fabricated on the surface by photolithography. The mask consisted of a grid of 400 μm $\times$ 400 μm squares with column and row indexing. Considering the defect density in the order of $10^3/\text{cm}^2$, this mask allows to trace individual defects through the different measurement techniques used in the present investigation.

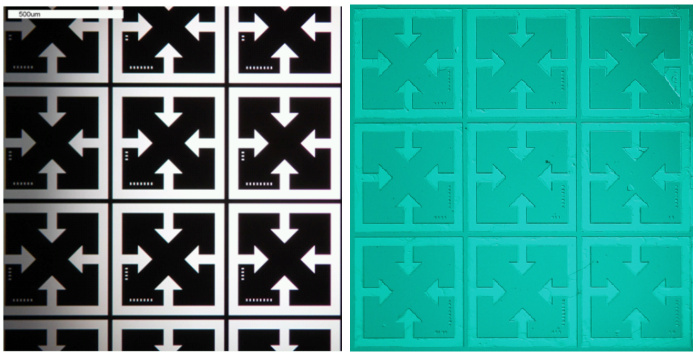

Figure 3.3: Negative of the mask (left), DIC microscopy photo of a sample surface after photolithography (right), one square corresponds to 400 x 400 μm.

3.3 INVESTIGATED MICROCAVITY SAMPLES

In this work we investigated two microcavity samples, MC1 and MC2, grown in a VG Semicon V90 MBE machine with a hot-lip Veeco 'SUMO' cell as Ga source, samples details are given in Table 3.1. The sample MC1 was studied in [23, 65] and these studies will be presented in Sec. 3.4.1 and Sec. 3.4.2, while sample MC2 was studied in [65] and these results will be discussed in Sec. 3.4.2. During the growth of MC1, the wafer temperature was ramped up to 715 °C for the AlAs Bragg layers and down to 660°C for GaAs Bragg layers, while the cavity layer was grown at 630 °C. During the growth of MC2 instead, the growth temperature was 590 °C for all layers. The two samples show a significantly different aspect ratio of defects on their surface. In MC1 they are essentially round (see Fig. 3.15), while in MC2 they have an aspect ratio between 3:1 and 2:1 along the $[1\bar{1}0]$: $[110]$ direction as shown in Fig. 3.17. At a temperature of T=80 K, the cavity mode energy in the center of the wafer of MC1 (MC2) is at $\hbar\omega_c = 1.480(1.431)$ eV, respectively, while the bulk GaAs exciton resonance of the cavity layer is at 1.508 eV.

Sample		MC1	MC2
cavity length		$1\lambda_c$	$2\lambda_c$
DBR periods top(bottom)		24(27)	23(26)
growth temperature (°C)	DBR AlAs	715	590
	DBR GaAs	660	590
	cavity GaAs	630	590

Table 3.1: Parameters of samples MC1 and MC2.

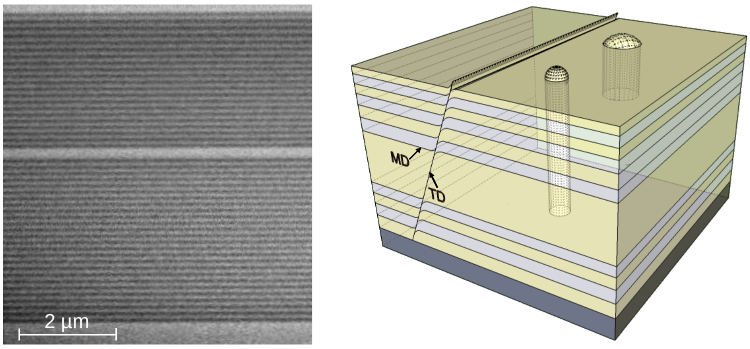

Figure 3.4: Scanning electron micrograph of the studied microcavity MC1 (left), and a sketch of the sample structure (right) showing examples of defects, starting from different layers across the structure.The MD and TD are examples of misfit and threading dislocations respectively which propagate across the structure.

3.4 RESULTS

3.4.1 OPTICAL AND SURFACE STUDIES

3.4.1.1 Disorder variation versus growth temperature

During the growth of the MC1 sample, the temperature was changed for the growth of different components as discussed in Sec. 3.3. For comparison, in Ref. [31] the sample was grown at a constant temperature of 620°C. A radial non-uniformity of the back-surface roughness due to As evaporation from the back-surface and resulting Ga-droplet formation was observed (see Fig. 3.5g). This indicates that the growth temperature was non-uniform across the wafer, an effect which is significant due to the usage of an undoped and back-side polished 3-inch wafer, leading to a weaker radiative coupling to the surrounding compared to doped wafers, increasing the infrared absorption, and unpolished wafers, decreasing the reflection and avoiding radiation trapping by total-internal reflection. The cavity resonance energy was varying by only 0.5 % over the wafer, indicating an exceptional flux homogeneity of the Ga and Al cells. The polariton disorder instead was found to vary significantly as function of radial position R on the wafer, as shown in Fig. 3.5a)-f) where transmission images and spectra are shown at different R. Close to the center ($R = 4\,\mathrm{mm}$), a cross-hatch pattern is visible and the polariton states excited at $k = 0$ show an inhomogeneous broadening of $\sim 100\,\mu$eV. This cross-hatch disorder decreases with increasing radius, and is not discernible at $R = 32\,\mathrm{mm}$ close to the edge of the wafer. The cross-hatch disorder is described in Chap. 4. In the wafer region with low cross-hatch disorder ($R = 32\,\mathrm{mm}$) the inhomogeneous broadening of the polariton line is only about 30 μeV over millimeter sized regions. This exceptional spatial homogeneity is confirmed by the propagation of polaritons over hundreds of micrometers visible in Fig. 3.5 h) where the interference pattern of freely propagating polaritons with the ones scattered by the PDs is observed for oblique excitation a few degrees from normal corresponding to $\mathbf{k} \approx (-0.3, 0)/\mu\mathrm{m}$. PDs are visible in all sample regions, and form natural defects which we investigate further in the subsequent sections. The homogeneous polariton linewidth can be estimated by spectral speckle analysis [66] from the spectral speckle width in the spatially resolved transmission spectra shown in Fig. 3.5 d-f) which are found to be similar to the spectrometer resolution. In the region $R = 32\,\mathrm{mm}$, positions with a single peak were present, which we fitted with a Voigt function. The full width at half maximum (FWHM) of Gaussian and Lorentzian parts of the spectrometer response, which are equal to 18 μeV each, were subtracted from the fitted broadenings of the measured lineshapes. The deduced homogenous (Lorentzian) FWHM linewidths

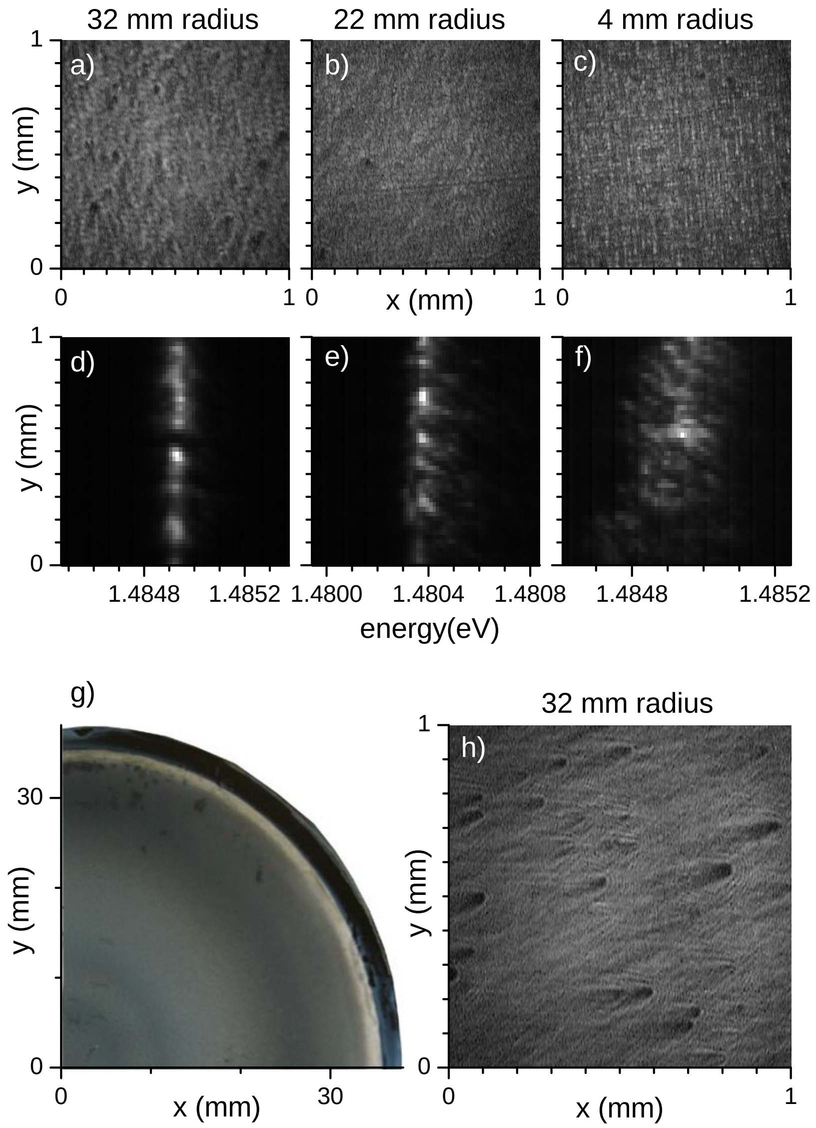

Figure 3.5: Disorder variation across the 3 inch wafer. Transmitted intensity for excitation at $\mathbf{k} = 0$ with 100 fs pulses resonant to the cavity mode for samples from different radial positions on the wafer as indicated. a),b),c) spatially resolved, spectrally integrated. d),e),f) spectrally resolved as function of y at a given x position. Linear gray scale from zero (black) to white. g) Image of the back side of the wafer. h) as a), but for excitation at $\mathbf{k} \approx (-0.3, 0)/\mu$m.

Γ were between 10 μeV and 20 μeV, corresponding to lifetimes $T_1 = \hbar/\Gamma$ of $30-60$ ps.

3.4.1.2 Polariton states bound to point-like defects

The spatial distribution of polariton energies can be visualized by resonant excitation with a spectrally narrow source. We used a single-mode external cavity diode laser (Sacher Lynx) with 5 MHz linewidth, compare Sec. 2.2, to excite the polaritons at normal incidence ($\mathbf{k} = 0$) over a large size in real space ($\sim$ 1 mm) from the substrate side. The emission from the epi-side was imaged onto a CCD. By tuning the excitation photon energy below the band edge of the extended cavity polaritons, individual localized states can be excited resonantly and appear as bright spots. By scanning the photon energy, the localized defect states within the excited area are sequentially addressed according to their eigenenergy. This excitation allowed to selectively image a specific polariton energy with a spectrally integrating detector. An example is shown in Fig. 3.6, where images corresponding to three different excitation photon energies are overlayed into a color image. The different colors of the localized states show their different eigenenergies $\hbar\omega_n$. Different shapes of the localized states are also visible, and we find an average distance of a few 10 μm between the PDs with localized states separated by more than 1 meV from the band edge. To gain more detailed information about the set of states bound to an individual PD, we change excitation and detection setup to the pulsed 100 fs source centered $\sim$ 10 meV below

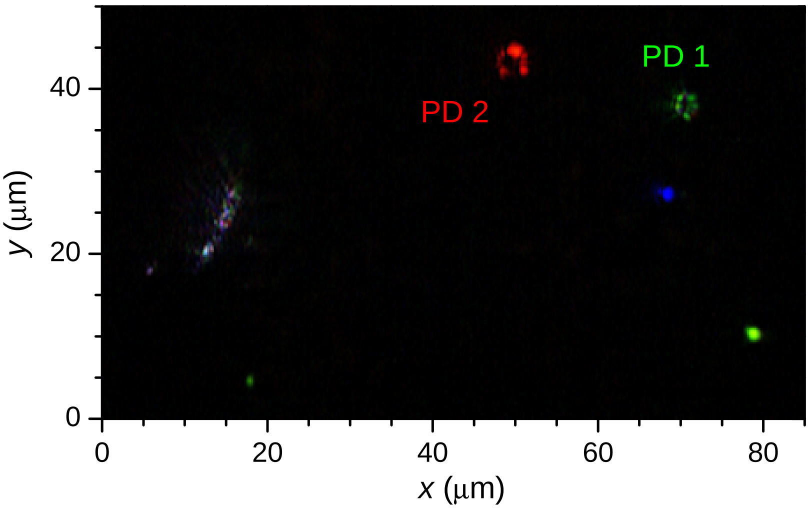

Figure 3.6: Spatially resolved color coded transmission intensity for photon energies of 1482.1 meV (red channel), 1482 meV (green channel), and 1473.8 meV (blue channel). Two localized states are labeled PD 1 and PD 2 for later reference. Animations of the data over the photon energy are available in Ref. [23].

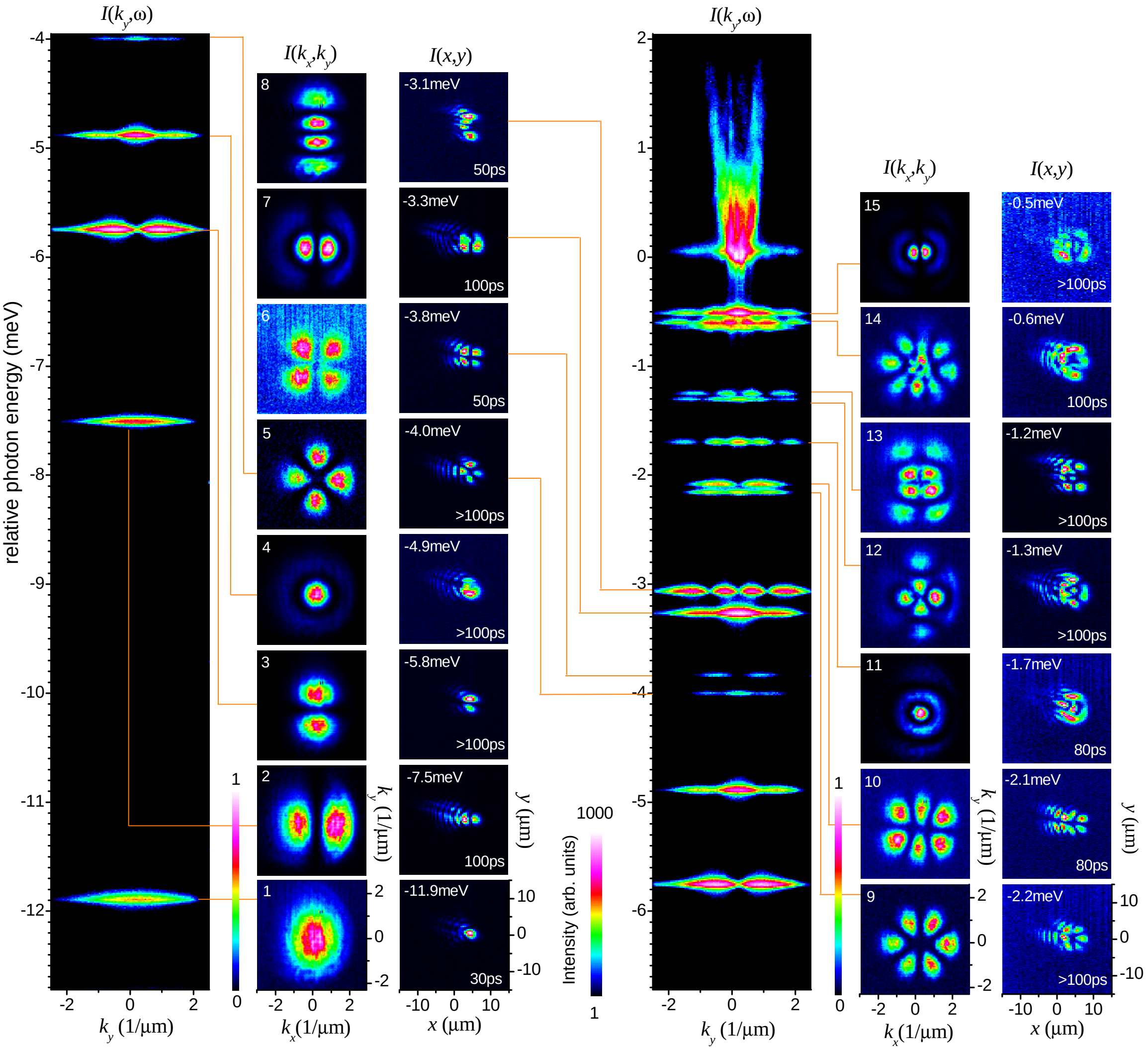

Figure 3.7: Spectral imaging of the emission from polariton states close to PD 1 of Fig. 3.6 in real and reciprocal space. The figure is split into two columns for space reasons. Each column shows on the left the intensity $I(k_x = 0, k_y, \omega)$ on a logarithmic color scale as indicated. The energy $\hbar\omega$ is shown relative to the polariton band edge at $\hbar\omega_\mathrm{c} = 1.4833\,\mathrm{eV}$. The intensity of the individual states is given the middle in reciprocal space $I(k_x, k_y, \omega_n)$, and on the right in real space $I(x, y, \omega_n)$, using a linear color scale normalized to the maximum for each state. The state wavefunction number Ψ_n is shown in the left upper corner of the 2-dimensional k-space images, the resonance energies relative to the band edge $\hbar\omega_n - \hbar\omega_\mathrm{c}$ are shown in the left upper corner of the 2-dimensional real space images and the lifetimes are shown in the right lower corner of the 2-dimensional real space images for each state. The connection lines indicate the corresponding state in $I(k_x = 0, k_y, \omega)$. The tails visible in $I(x, y, \omega_n)$ are due to imaging abberations relevant at large $\mathbf{k}$.

the polariton band-edge, spatially focussed onto the PD. The emission was measured using spectrally resolved imaging in either real or reciprocal space, as discussed in section Sec. 2.2. The resulting data for the polariton states bound to PD 1 are shown in Fig. 3.7. On the left the directionally and spectrally resolved intensity $I(k_x = 0, k_y, \omega)$ is given on a logarithmic scale showing bound resonances and the continuum. A series of $n_1 = 16$ discrete resonances is discernable, at frequencies ω_n, $n = 1..n_1$. The intensity distributions at these resonances in real and reciprocal space, $I(x, y, \omega_n)$ and $I(k_x, k_y, \omega_n)$, respectively, are proportional to the probability distributions $|\Psi_n|^2$ of the corresponding state wavefunctions Ψ_n (assuming that the Bragg mirror reflectivity is independent of $\mathbf{k}$ and all relevant emission directions $\mathbf{k}$ are imaged). For convenience we show the localization energy $\Delta_n = \hbar\omega_n - \hbar\omega_\mathrm{c}$ of the states, where $\hbar\omega_\mathrm{c}$ is the band edge given by the minimum of the parabolic dispersion of free polaritons. The lifetime of each state is also shown, deduced from the linewidth by correcting for the spectrometer response, using a Voigt-fit as described in section 3.4.1.1. From the systematic error in the fit we estimate an error of $5\,\mu$eV in the deduced linewidths, limiting the maximum measurable lifetime to about 100 ps. Many of the states show lifetimes in the order of 100 ps, corresponding to a Q-factor of $4 \cdot 10^5$, one order of magnitude higher than measured in mesa microcavity defects reported in Ref. [67]. In Fig. 3.7, the ground state Ψ_1 is observed at $\Delta_1 = -11.9\,\mathrm{meV}$. The shapes of the wavefunctions reveal a nearly cylindrical symmetry of the effective confinement potential $V_1(x, y)$ created by PD 1. The first excited state Ψ_2 is found at $\Delta_2 = -7.6\,\mathrm{meV}$, and shows a p_x-like symmetry, with a node at $x = 0$. Ψ_3 has $\Delta_3 = -5.8\,\mathrm{meV}$ and a p_y-like symmetry with a node at $y = 0$. The energy splitting of $\Psi_{2,3}$ shows a breaking of cylindrical symmetry of $V_1(x, y)$. The next 3 states correspond to d-states, Ψ_4 having zero angular momentum and 2 nodes in radial direction, and $\Psi_{5,6}$ being superpositions of angular momentum 2. The non-degeneracy of the different n=2 states shows the non-parabolicity of the confinement. The higher states can be classified in a similar way with increasing number of nodes in the wavefunction.

PD 2 instead is not cylindrically symmetric as shown in Fig. 3.8a). The two lowest states $\Psi_{1,2}$ are separately localized to the left and the right of the defect center with a s-like wavefunction, indicating two separate minima of the potential. The left minimum confines also a p-like excited state Ψ_3, while the corresponding excited state on the right Ψ_4 is already extended along a horseshoe-shaped region, coupling to a d-like state of the left minimum. The next state Ψ_5 is a mixture of the left f-like state with the right d-like state. Ψ_6 is mostly localized on the tip of the horseshoe, possibly due to a local potential maximum close to the state energy, which is supported by the relatively small wavevector spread in k_x. A total of $n_3 = 11$ states are visible.

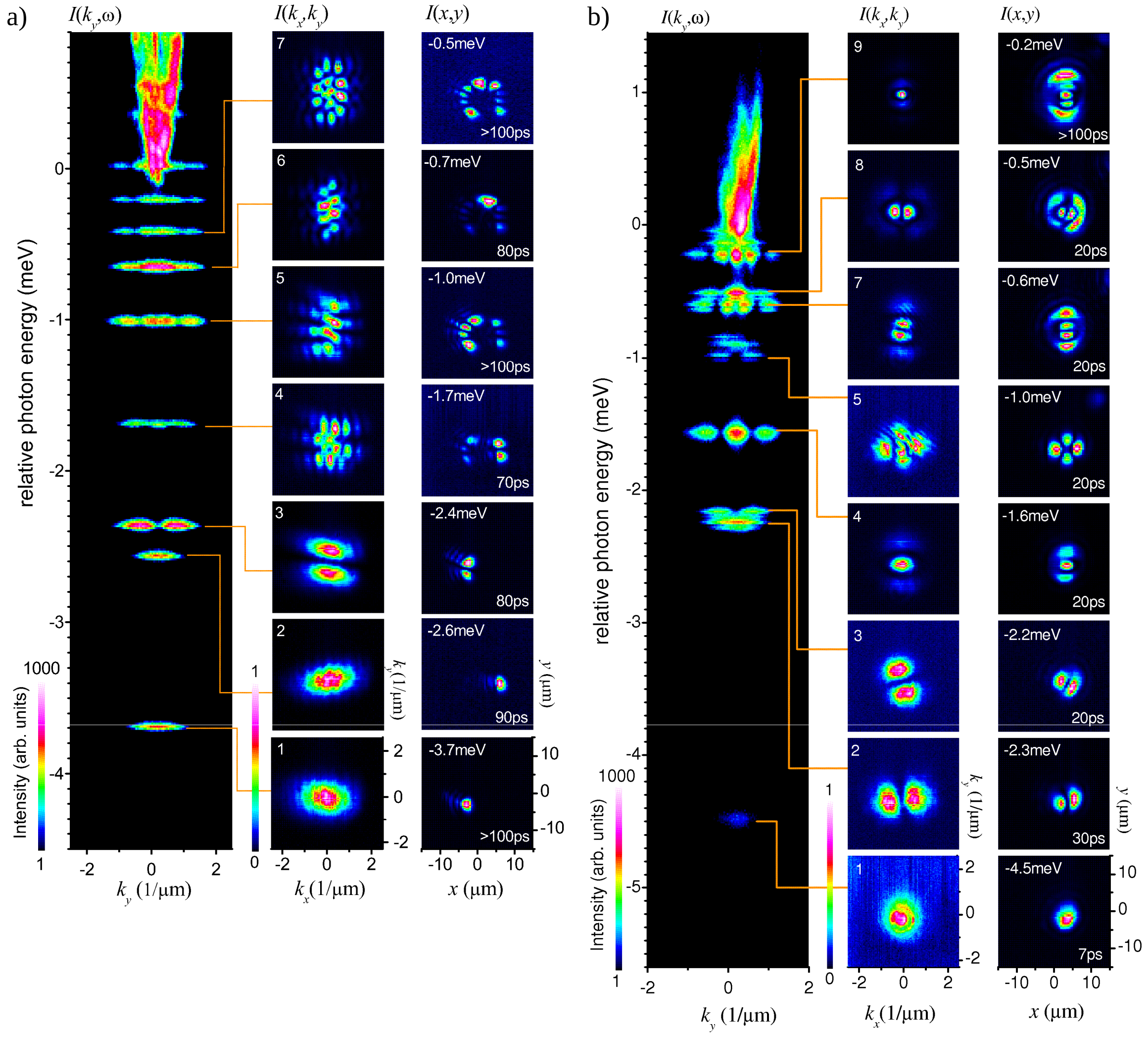

Figure 3.8: a) as figure 3.7, but for PD 2 of Fig. 3.6 and $\hbar\omega_c = 1.4826\,\mathrm{eV}$. b) as figure 3.7 but for PD 3, (not shown on Fig. 3.6), and $\hbar\omega_c = 1.4815\,\mathrm{eV}$.

Some resonances are observed even above the continuum, indicating the presence of a potential barrier between the defect region and the surrounding continuum. The last reported defect, PD 3 (see Fig. 3.8b), not shown in Fig. 3.6), is similar to PD 1 in being approximately circular symmetric, but about a factor of 3 shallower. The ground state Ψ_1 is s-like, and shows a larger extension in real space and a smaller extension in reciprocal space than the ground state of PD1, as expected from the weaker confinement. A total of $n_3 = 12$ states are visible.

3.4.1.3 Coherent wavepacket dynamics

In the transmission experiment, all states are excited simultaneously and coherently to each other by the focussed femtosecond laser pulse as was discussed in Sec. 2.2. The resulting transmission is accordingly a coherent superposition of the emission by the states after excitation. As seen on Fig. 3.8b), some states have a small energy difference, comparable to their linewidth. The emission at an energy close to their eigenenergy is thus a coherent superposition of the states, with an initial phase and amplitude determined by the spatial overlap between the state and the excitation field. We illustrate the effect of such a coherent superposition here with two examples. Firstly, we note the two p-like excited states $\Psi_{2,3}$ of PD 3 which are nearly degenerate ($\approx 100\,\mu$eV separation). The emitted field close to their energy is a coherent superposition of the two wavefunctions $a\Psi_2+b\Psi_3$, with amplitudes determined by the excitation. To compare the measurements with the theoretically expected result, we assume harmonic confinement and p-like wavefunctions $\Psi_{2,3} \propto (k_x, k_y) \exp\left(-\frac{k_x^2+k_y^2}{a^2}\right)$ with frequencies $\omega_{2,3}$ and linewidths $\gamma_{2,3}$ which are a sum of the state linewidth and spectrometer resolution. The measured wave-function can be modeled as a coherent superposition of the two near-resonant states with a relative phase ϕ and amplitude η given by the excitation conditions. This superposition can be written as

$$\Psi(\mathbf{k},\omega) \propto \left(\frac{k_x}{\omega-\omega_2+i\gamma_2} + \eta e^{i\phi}\frac{k_y}{\omega-\omega_3+i\gamma_3}\right) e^{-\frac{k_x^2+k_y^2}{a^2}} \tag{3.1}$$

Similarly, for the d-like $l = 2$ states

$$\Psi_{5,6} = (k_x k_y, k_x^2 - k_y^2) \exp\left(-\frac{k_x^2+k_y^2}{a^2}\right) \tag{3.2}$$

with frequencies $\omega_{5,6}$ and linewidths $\gamma_{5,6}$,

Simulations according to these wavefunctions, using parameter values taken from the experiment as indicated in Fig. 3.9, give a qualitative agreement with measurements. Animations of the data over the photon energy are available in Ref.[23]. Some results showing localization of polariton condensates in defects exhibiting d-like symmetry was discussed in Ref. [68].

3.4.1.4 Confining potential

The observed localized polariton states can be related to an effective confinement potential $V_m(\mathbf{r})$ for the in-plane polariton motion where m is the PD state number. We can estimate $V_m(\mathbf{r})$ using the spectrally integrated density of states $D_m(\mathbf{r})$ created

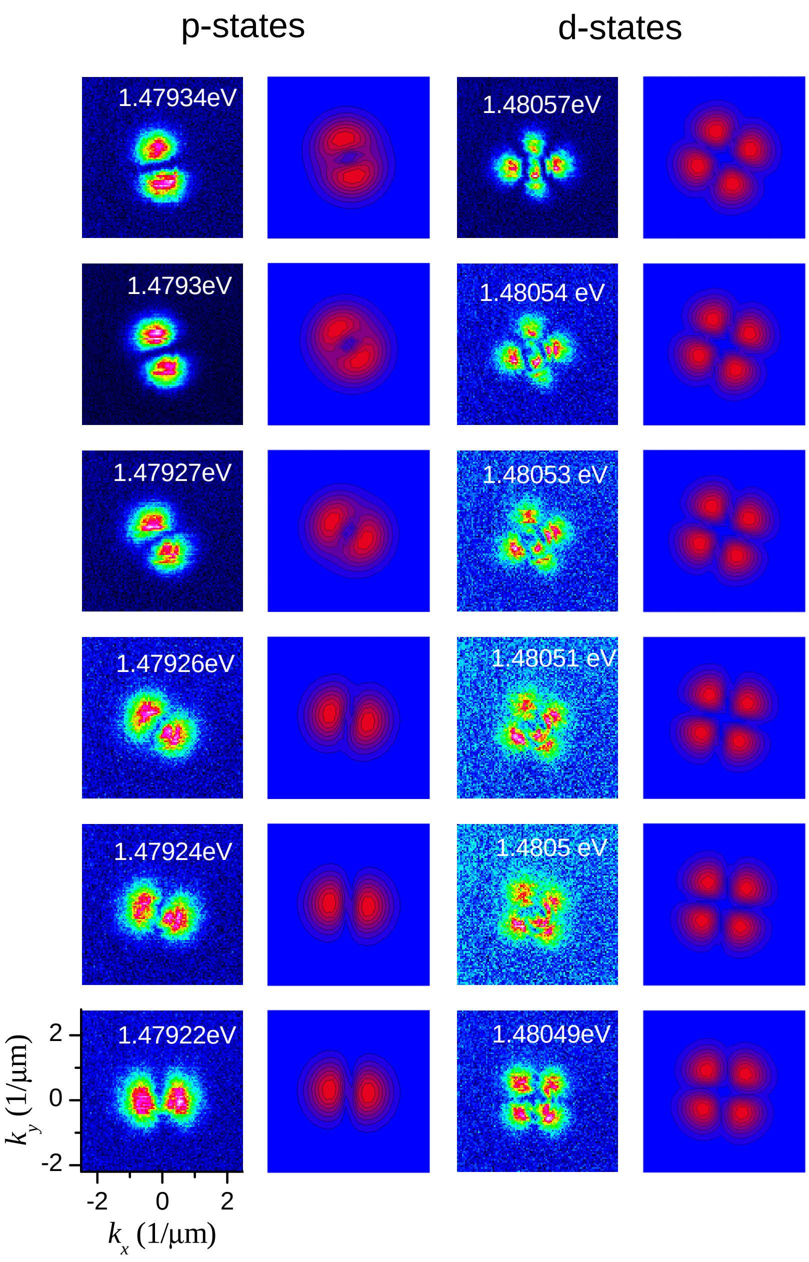

Figure 3.9: Measured intensities $I(\mathbf{k},\omega)$ from the same experiment as shown in Fig. 3.8b), for energies $\hbar\omega$ as labeled, using fine steps across the p-states (left) and d-state (right) resonances. The corresponding calculated $|\Psi(\mathbf{k},\omega)|^2$ for the same energies are given to the right of each experimental intensity image. The energy is given in the upper part of each image, and increases from lower to upper panels as labeled. The parameters used in simulations according to Eq.(1) and (2) were $\hbar\omega_2 = 1.479115\,\text{eV}$, $\hbar\omega_3 = 1.479295\,\text{eV}$, $\hbar\gamma_2 = 58\,\mu\text{eV}$, $\hbar\gamma_3 = 73\,\mu\text{eV}$, $\eta = 1$, $\phi = 0$ for the p-state simulation, and $\hbar\omega_5 = 1.480381\,\text{eV}$, $\hbar\omega_6 = 1.480559\,\text{eV}$, $\hbar\gamma_5 = 37\,\mu\text{eV}$, $\hbar\gamma_6 = 50\,\mu\text{eV}$,$\eta = 1$, $\phi = 0$ for the d-state simulation.

by $V_m(\mathbf{r})$ below the continuum edge in the following way. On the one hand, this density can be calculated from the spatially resolved bound density of states

$$D_m(\mathbf{r}) = \sum_{n=1}^{n_\mathrm{m}} |\Psi_n(\mathbf{r})|^2 \tag{3.3}$$

where the bound state probability densities $|\Psi_n(\mathbf{r})|^2$ are taken as the normalized measured intensity

$$|\Psi_n(\mathbf{r})|^2 = \frac{I(\mathbf{r}, \omega_n)}{\int I(\mathbf{r}, \omega_n) d\mathbf{r}^2}. \tag{3.4}$$

This expression assumes that the emitted field is proportional to the polariton wavefunction, which is valid for a cavity lifetime which is constant for the in-plane wavevector components of the bound states. This is a good approximation for the data shown here since the maximum in-plane wavevector of about $2/\mu$m is only 8% of the light wavevector in the Bragg Mirrors.

On the other hand, $D_m(\mathbf{r})$ is given by the integral of the free density of states from zero kinetic energy at the potential floor to the continuum when neglecting the spatial variation of the confinement potential, *i.e.* in the limit of small level splitting compared to the confinement potential. In two dimensions the density of states is constant and given by $D_{2D} = m/(2\pi\hbar^2)$, such that the integral over the density of states is given by $-V_m(\mathbf{r})D_{2\mathrm{D}}$, and we find $V_m(\mathbf{r}) = -D(\mathbf{r})/D_{2\mathrm{D}}$. We use the effective mass of the polaritons from the measured dispersion $m = 2 \cdot 10^{-5}\, m_\mathrm{e}$, where m_e is the free electron mass. The resulting confinement potentials for the three investigated PDs are shown in Fig. 3.10. The symmetry of the potentials reflect the symmetry of the localized states. Comparing with the energies of the confined states, $V_m(\mathbf{r})$ seems about factor of 2 to small. Errors in the scaling of $V_m(\mathbf{r})$ are due to the length calibration of the imaging, which we estimate to have an accuracy of 30%, yielding a 70% error in $V_m(\mathbf{r})$, and to the effective mass m which we estimate to have an error of 10%. Furthermore, the approximation of a small level splitting compared to the confinement potential yields an error intrinsic to the model. Using numerical simulations for a square well potential we find that the finite number of levels n_m leads mostly to spurious spatial oscillations in the predicted potential, while the average is reproduced to a relative error of $1/n_\mathrm{m}$, so about 10-20% in our case. A direct comparison of the polariton states and their energies in the confining potential $V_m(\mathbf{r})$ could be used to determine the $V_m(\mathbf{r})$ more accurately.

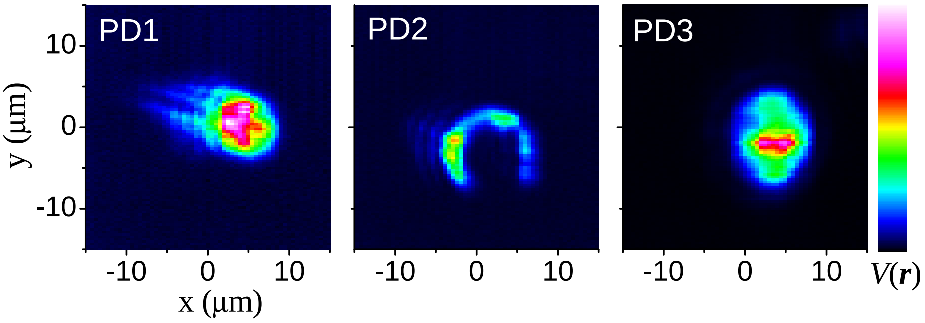

Figure 3.10: Confinement potential $V_m(\mathbf{r})$ estimated from the bound density of states $D_m(\mathbf{r})$ for the three PDs, on a color scale as given from 0 (black) to -5.4 meV (white).

3.4.1.5 Origin of the point-like defects

In order to investigate if the observed PDs are related to threading dislocations, we used an etching procedure as described in Section 2.3. The sample surface after etching is shown in Fig. 3.11. Each rectangular etch pit marks a threading dislocations in its center. We found an etch-pit density of about $10^3/\,\mathrm{cm}^2$, consistent with the manufacturer specification of the threading dislocations density for the GaAs wafer used as a substrate. The lines are scratches on the sample surface and/or misfit dislocations. Subsequently, low temperature transmission measurements were made together with reflection microscopy. The positions of the PDs was found to be not correlated to the etch-pits. Instead, the PDs coincide with the round to oval structures of 7-10 micrometer diameter on the sample surface, as demonstrated in Fig. 3.12. These defects are thus the origin of the localization potentials for the polaritons. An overview of several defects and their height profiles obtained using DIC microscopy is shown in Fig. 3.13.

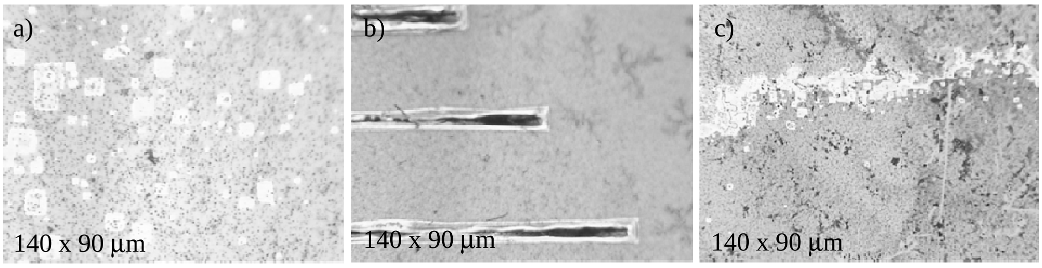

Figure 3.11: Sample surface under optical microscope after chemical etching with KOH, a) regions with high density of dislocations, b) surface misfit dislocation, c) dislocations pinned along a line

.

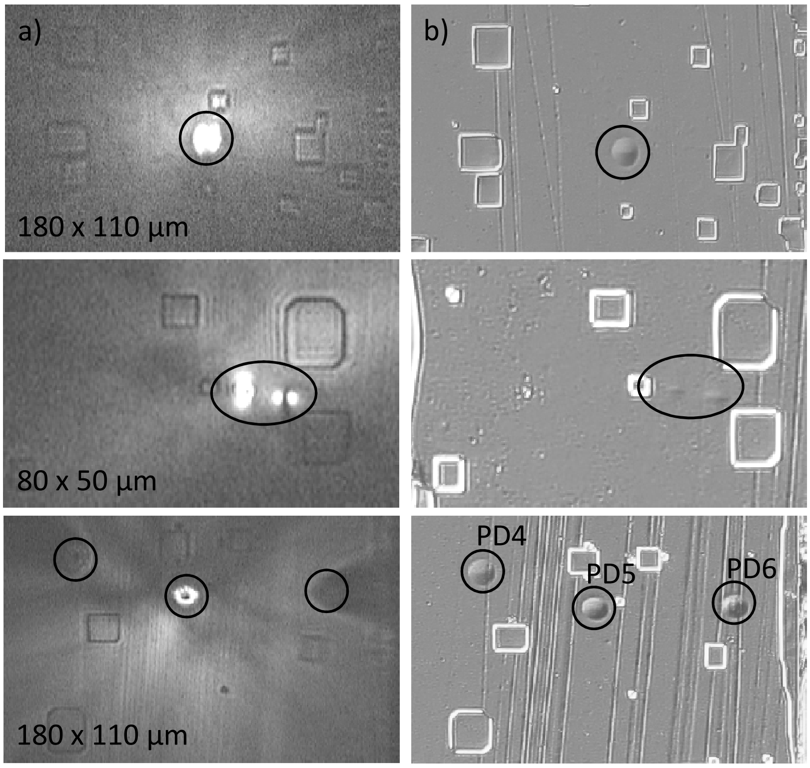

Figure 3.12: The same area of the sample surface was imaged using optical imaging spectroscopy, shown in column a), and DIC microscopy, shown in column b). No correlation is observed between etched pits and PDs. On the contrary, correlation between localized polaritons states and surface modulation is clearly observed. Defects marked PD4-6 are investigated further in Fig. 3.13. Rectangular shapes on the surface are etched pits.

From the DIC images, we have quantitatively extracted the surface profile of the PDs. They show a typical surface height modulation of several tens of nanometers, being approximately parabolic with a small depression about 10% of the height below the original surface at the edge, and a width of a few μm. The energy barrier to the continuum observed in the localized states (see Section 3.4.1.2) is likely to be related to this edge depression.

Also atomic force microscopy images of the surface were obtained, but due to the large extension and small height of the PDs no reliable results of the large scale topology could be extracted. Using field emission scanning electron microscopy(FESEM), the structures were imaged under grazing angle of incidence (70° to the surface normal) to enhance the contrast for the flat surface topology, and results are shown in Fig. 3.13. The shape is consistent with the DIC images. A ridge shaped structure close to the center of the dome is also visible. Growth related defects were categorized in Ref. [62], showing some defects which qualitatively resemble the ones discussed here.

We observed defects with different shapes, with the most common being nearly round defects with a weak ridge in the center, as shown on Fig. 3.13. According to Ref. [62] round defects with a nucleus originate from Ga oxide or spitting, while obscure ovals arise from Ga droplets, oxides or particle contaminants.

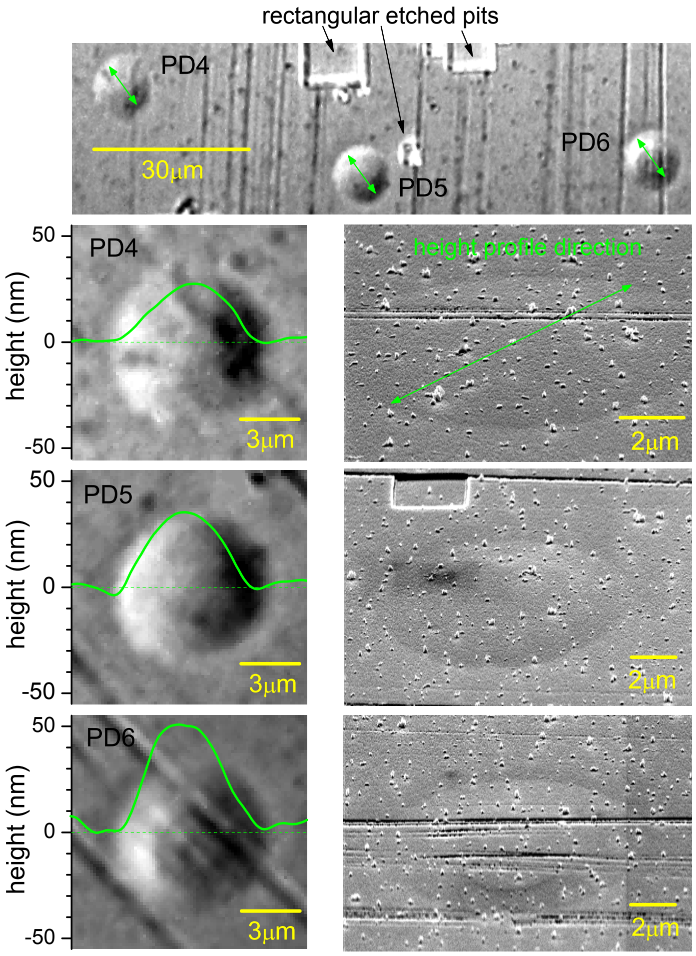

Figure 3.13: Top: Sample surface after KOH etching imaged with DIC. Round defects corresponding to PDs are labeled. Below in the left column, individual height profiles of PDs obtained using DIC with the corresponding DIC images. In the right column, corresponding FESEM images of the PDs obtained under grazing angle of incidence (70° to the surface normal) to enhance the contrast for the flat surface topology. The grains on the surface are due to post-growth contamination. Sizes of defects obtained using different methods agree as shown on the pictures.

3.4.2 Optical, surface and volume structure studies

3.4.2.1 Sample MC1

The localized polariton states in the round defects of sample MC1 were examined in the previous section. Here we discuss the correlation between the states and the three-dimensional structure of these defects using two defects, PD1' and PD2', as examples. The localized polariton states of PD1' are observed in the hyperspectral transmission images shown in Fig. 3.14. The defect shows 16 localized modes down to $-9\,\mathrm{meV}$ below the polariton continuum. It can be noted that the lowest state observed here is of p_x-type symmetry. We expect to have 2 states with lower energies, another p_y-state and an s-state. These were not observed. To qualitatively model the states bound to this defect, we compare them with solutions of the 2D time dependent wave equation $\left(\partial_x^2+\partial_y^2-\partial_t^2/v^2\right)\Psi=0$ with the velocity v for elliptical boundary conditions. Using elliptical coordinates $x=c\cosh(\xi)\cos(\eta)$, $y=c\sinh(\xi)\sin(\eta)$ with the focus distance c, and the ansatz $\Psi(x,y,t)=R(\xi)\Phi(\eta)e^{i\omega t}$ results in the ordinary and modified Mathieu equations for the angular part $\Phi(\xi)$ and radial part $R(\xi)$, respectively [69]

$$\left(\partial_\eta^2+\lambda-2q\cos(2\eta)\right)\Phi=0 \tag{3.5}$$

$$\left(\partial_\xi^2+\lambda-2q\cosh(2\eta)\right)R=0 \tag{3.6}$$

where $q=(\omega c/2v)^2$ is the square of the normalized frequency. The solutions of Φ and R are angular and radial Mathieu functions. For a given q, the periodic boundary condition of the angular part Φ in Eq.(3.5) determines a series of $\lambda_m(q)$ with ascending number of nodes $m=0,1,2,...$, each of which except $m=0$ is a doublet, having an odd (o) or even (e) symmetry for inversion of y.

The elliptical boundary is given by a unique c and ξ_0, at which the boundary condition, for example $R(\xi_0)=0$, holds. This condition and Eq.(3.6) using $\lambda=\lambda_m(q)$ determines the mode frequencies $q_{n,m}$ corresponding to modes with ascending number of nodes $n=0,1,2,..$ in radial direction. Analytic expressions for the solutions are given in Ref. [70].

Since the polaritons show a quadratic in-plane dispersion for small wavevectors, their in-plane motion is well described by the Schrödinger equation [67]. By modifying the definition of q, the above solutions for the Helmholtz equation are also solving the Schrödinger equation for elliptical boundary conditions , such as the elliptical quantum well with infinite barriers [71].

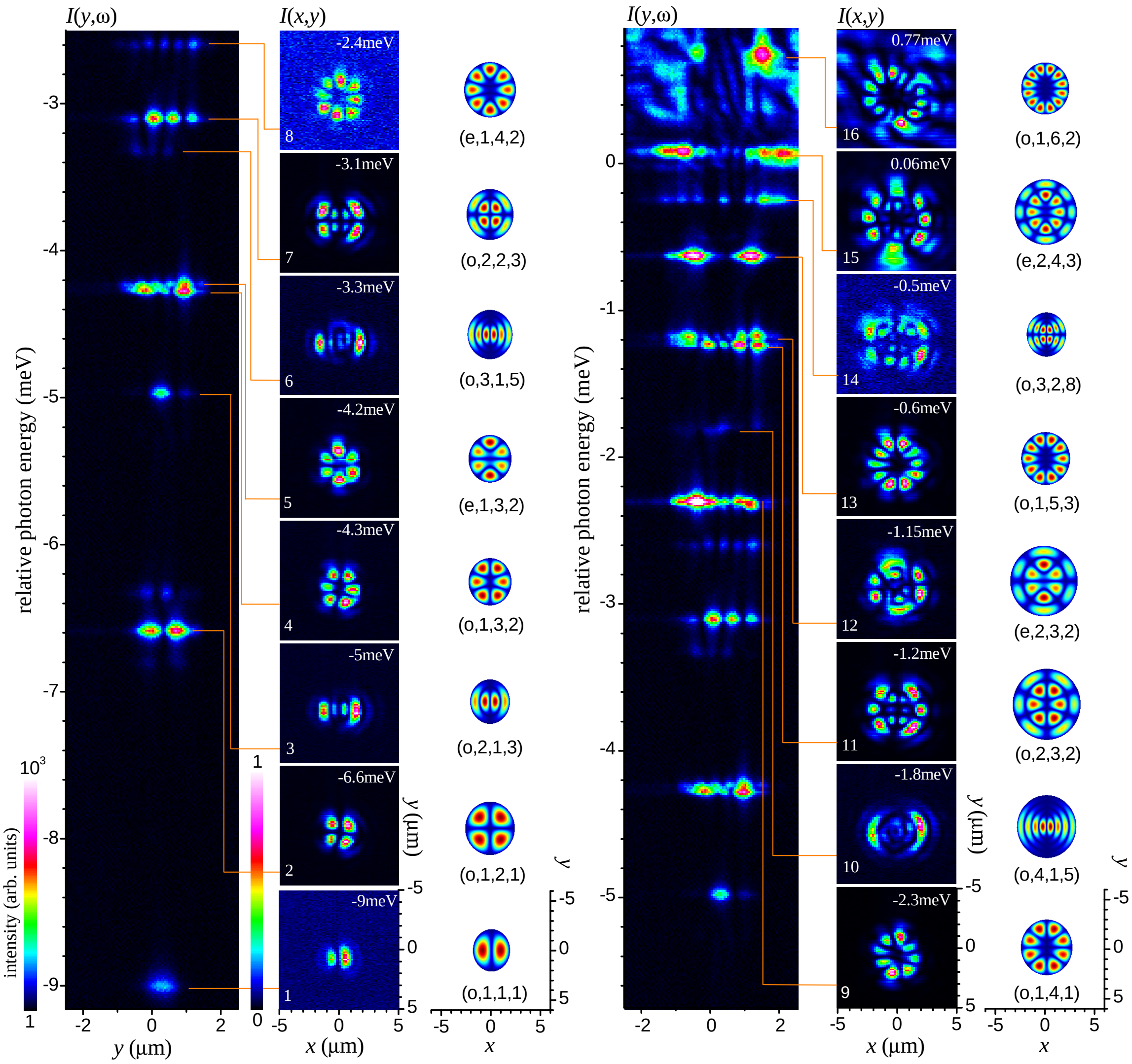

Figure 3.14: Hyperspectral imaging of polariton states bound to PD1' in MC1, measuring the spatially and spectrally resolved transmission intensity $I(x, y, \omega)$. First and fourth column: $I(0, y, \omega)$. The energy is shown relative to the polariton band edge at $\hbar\omega_c = 1.4789\,\text{eV}$. Intensity on logarithmic color scale as indicated. Second and fifth column: Real space intensity maps of individual states $I(x, y, \omega_l)$. The state number n and the relative energy $\hbar(\omega_l - \omega_c)$ are given, and the orange lines indicate the related peaks in $I(0, y, \omega)$. Third and sixth column: Real space distributions of corresponding squares of Mathieu functions, labeled by their parity ('e': even, 'o': odd), radial (n) and angular (m) order, and parameter q (see Eq.(3.5) and Eq.(3.6)). Color scale as for measured data indicated in the first column.

.

The solutions to the problems exhibiting elliptical symmetry such as a particle confined in an elliptical infinite potential well are given by the Mathieu functions [71]. The solutions[72] $|\Psi_{n,m,q}|^2$ for the boundary conditions corresponding to the elliptical quantum well with infinite barriers with the mode orders n, m assigned to the measured states of intensities $|\psi_l|^2$ are shown in Fig. 3.14. For each energy state a qualitative agreement is observed, where q was adjusted to approximately match the ellipticity of the simulation to the measured states. The structural characterization of PD1' by DIC and FIB/SEM is given in Fig. 3.15. The DIC data shows a diameter of the defect on the surface of about 6 μm, similar to the extension of the spatially resolved transmission from this defect, and a height up to about 15 nm. The FIB/SEM cross-sections show the origin of the defect - a thickened GaAs layer with a center depression in the third DBR period above the cavity, extending over 4 μm in x, and adding about 60 nm in thickness in the center, visible in the $y = 2.7\,\mu$m cross-section. Further discussion of the defect growth dynamics will be given later.

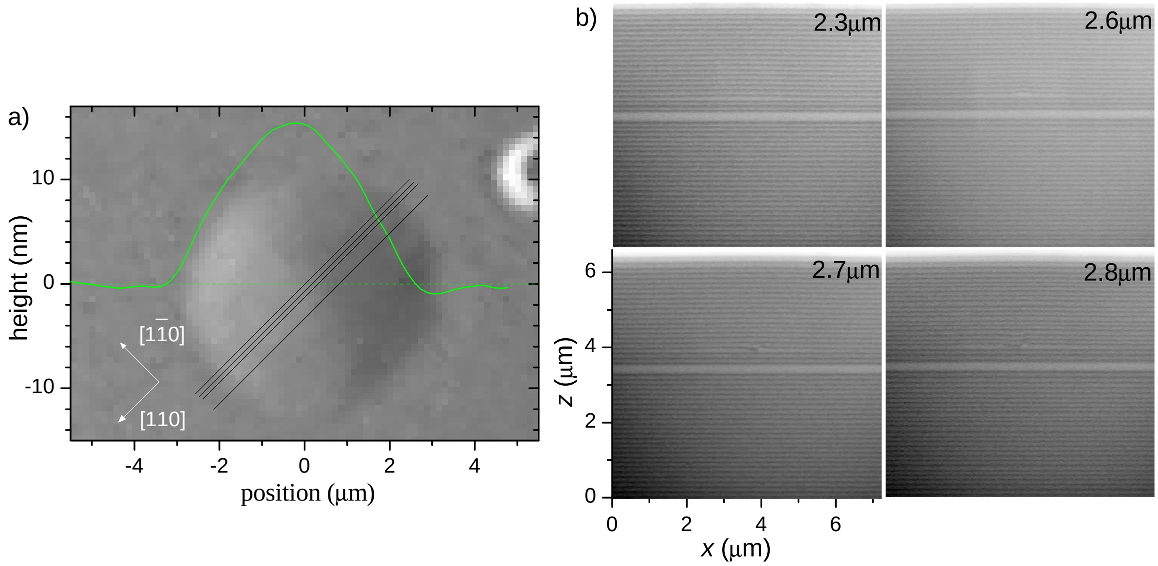

Figure 3.15: Structural characterization of PD1'. In a), DIC image of the sample surface (linear grey scale), and resulting height profile across the defect (green line). In b), SEM images of the cross-sections through the epitaxial structure are shown, taken along the black lines given in a). The relative distances from the edge of a defect are indicated.

We now move to the second defect PD2' on MC1, for which the hyperspectral transmission images are shown in Fig. 3.16a). The states are arranged along a ring of about 6 μm diameter, with the lowest state localized at small y, and higher states gradually extending along the ring, as in a one-dimensional harmonic oscillator, until the whole ring is filled. The underlying potential for the polaritons appears to be a ring-shaped

well, with a depth decreasing with increasing y. The analysis of the potential from the states shown in Sec. 3.4.2.3 confirms this interpretation.
The structural characterization of PD2' by DIC and FIB/SEM is given in Fig. 3.16b). The surface profile is similar to PD1', with a size of about 7 μm diameter. The defect source is much deeper in the structure than for PD1', in the 23rd period of the DBR below the cavity, and has a larger height of about 90 nm. This height is about twice the nominal height of the GaAs $\lambda_c/4$ layer, and leads to discontinuities of the DBRs for about 4 layers above the defect. The deep center depression of the defect is consistent with the ring-shaped polariton confinement potential shown in (see Fig. 3.21).

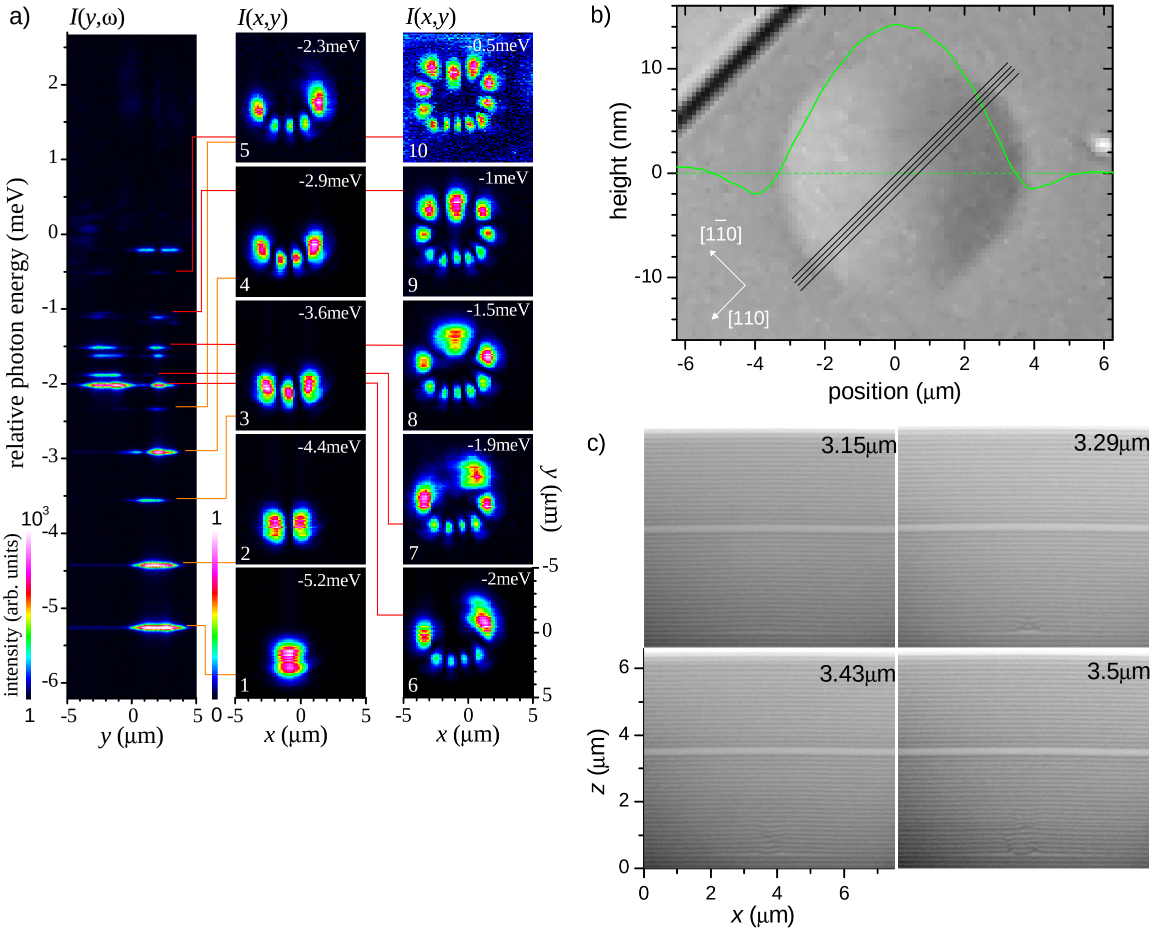

Figure 3.16: In a), polariton spectrum of PD2' with $\hbar\omega_c = 1.4787\,\text{eV}$, detailed description as for Fig. 3.14. In b) and c), structural characterization of PD2', detailed description as for as Fig. 3.15

3.4.2.2 Sample MC2

This sample was grown at lower temperature than MC1 (see Table 3.1), and exhibits oval-shaped defects. Two examples of defects for this samples are given here, referred to as PD3' and PD4'. The polariton states of PD3' are visible in the hyperspectral transmission images in Fig. 3.17a). The states come in nearly degenerate pairs with point reflected wavefunctions, extended along the x-axis ($[1\bar{1}0]$), for example the state pairs (1,2) and (3,4), (5,6). The states also have an approximate mirror symmetry about the x axis. Similar "double-well" eigenstates were observed for several other oval defects in this sample. All of them exhibit the same sequence of states, while the number of confined states was varying.

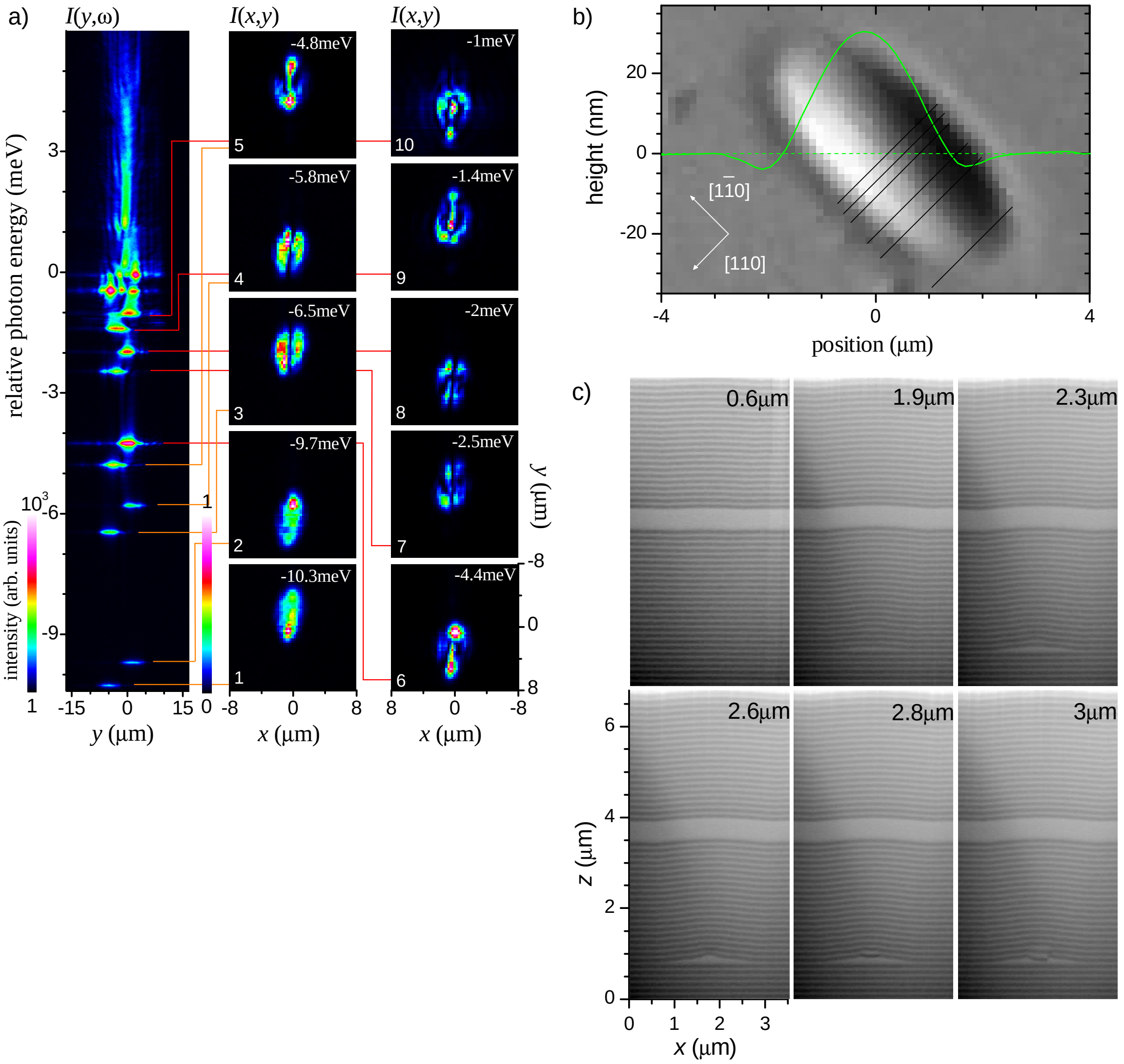

Figure 3.17: In a), polariton spectrum of PD3' with $\hbar\omega_c = 1.4353\,\mathrm{eV}$, detailed description as for Fig. 3.14. In b) and c), structural characterization of PD3', detailed description as for as Fig. 3.15.

Localization of the states close to the center of the defect, and the absence of mixed states of different parities indicate a very high potential barrier in the middle, and deep wells on both sides, with the corresponding potential in y direction could be written as $V(y) \propto \delta(y/b) + a/(|y/b| + 1)$ with the scaling constants a, b. The resulting states of the two sides $y \lessgtr 0$ do not mix significantly. The states for $y < 0$ are shifted by $< 1\,\mathrm{meV}$ to higher energies. In both wells we observe a ground state, followed by the first excited state some 4 meV above having one node and the second excited state some 2 meV further having two nodes, the third excited state some 2 meV with 3 nodes, and higher states.

The structural characterization of PD3' is given in Fig. 3.17b) and c). The surface profile is oval, with the extension along [110] of 3 μm, reduced by a factor of two compared to the one of PD1', while the extension along $[1\bar{1}0]$ of 6 μm is similar to one of PD1'. The height of the surface modulation is about 140 nm, twice the value seen for PD1' and PD2', and about twice the nominal height of the GaAs Bragg layer. The height increase is consistent with the reduced lateral size when accommodating

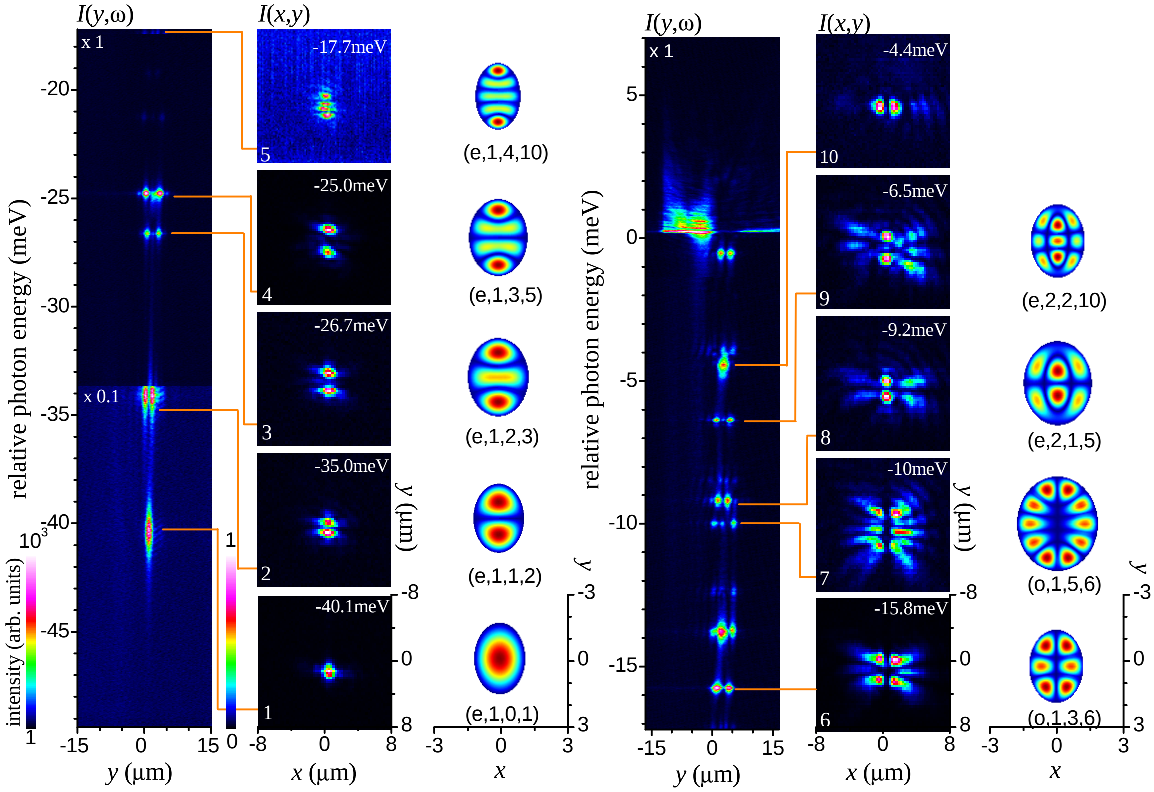

Figure 3.18: Polariton spectrum of PD4' with $\hbar\omega_c = 1.4343\,\mathrm{eV}$, detailed description as for Fig. 3.14. Data consist of three merged spectrometer positions and covers around 50 meV energy range. Corresponding calculated squared Mathieu functions of different orders and parity, as indicated on the plot, are shown in the third column.

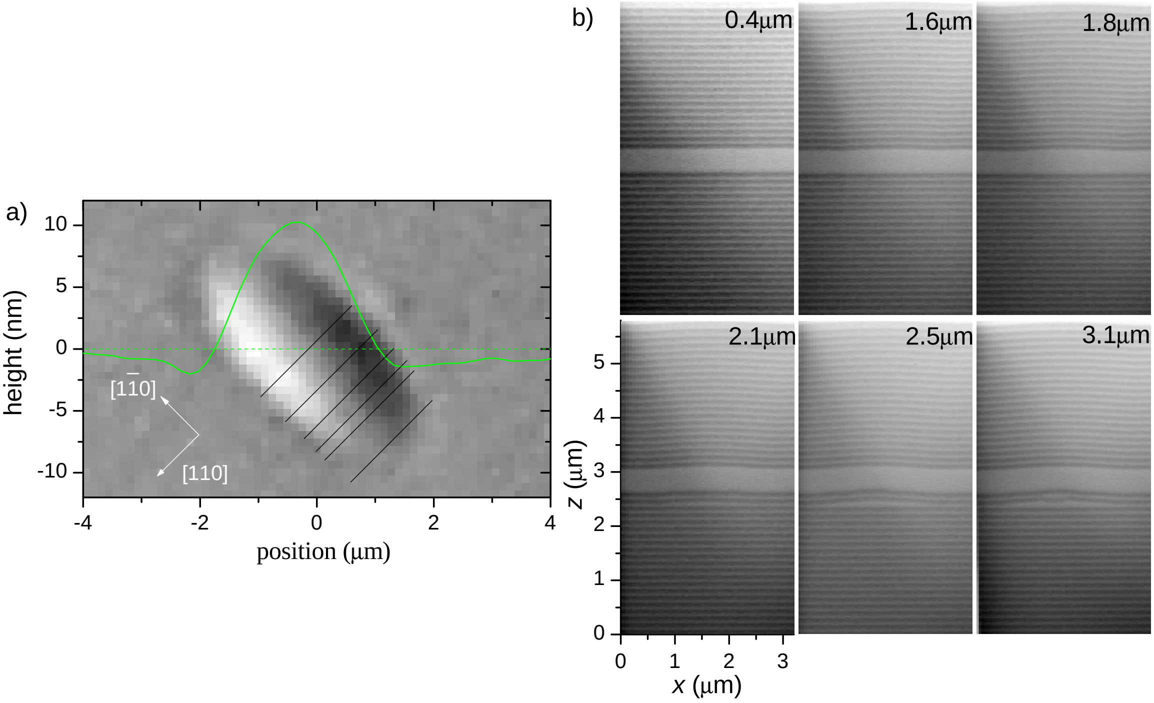

Figure 3.19: Structural characterization of PD4’, detailed description as for as Fig. 3.15.

the same volume. The defect source is in the 20th DBR period below the cavity.

We now move to the second defect PD4’ on MC2, for which the hyperspectral transmission images are given in Fig. 3.18. It shows the deepest localized states of all PDs studied, with the ground state 40 meV below the continuum. The states show an approximate mirror symmetry along the x and y axis. We can model them with Mathieu functions as shown in Fig. 3.18, using a strong ellipticity. The structural characterization of PD4’ is given in Fig. 3.19. The surface profile is oval as PD3’, but with a 20% smaller extension and a three time smaller height. The defect source is in second period of the DBR below the cavity, and has a height of about 100 nm. Being so close to the cavity, the additional GaAs has a strong influence on the polariton states, and the crater in the middle gives rise to a confinement potential with a barrier between the center and the peripheral area, as evidenced by the spatial distribution of the confined wavefunctions.

Moreover, we obtained AFM data on defects for this sample, example data is shown in Fig. 3.20. Defects height on the surface is in the order of 100 nm indicating that deposition of the droplet took place close to the surface.

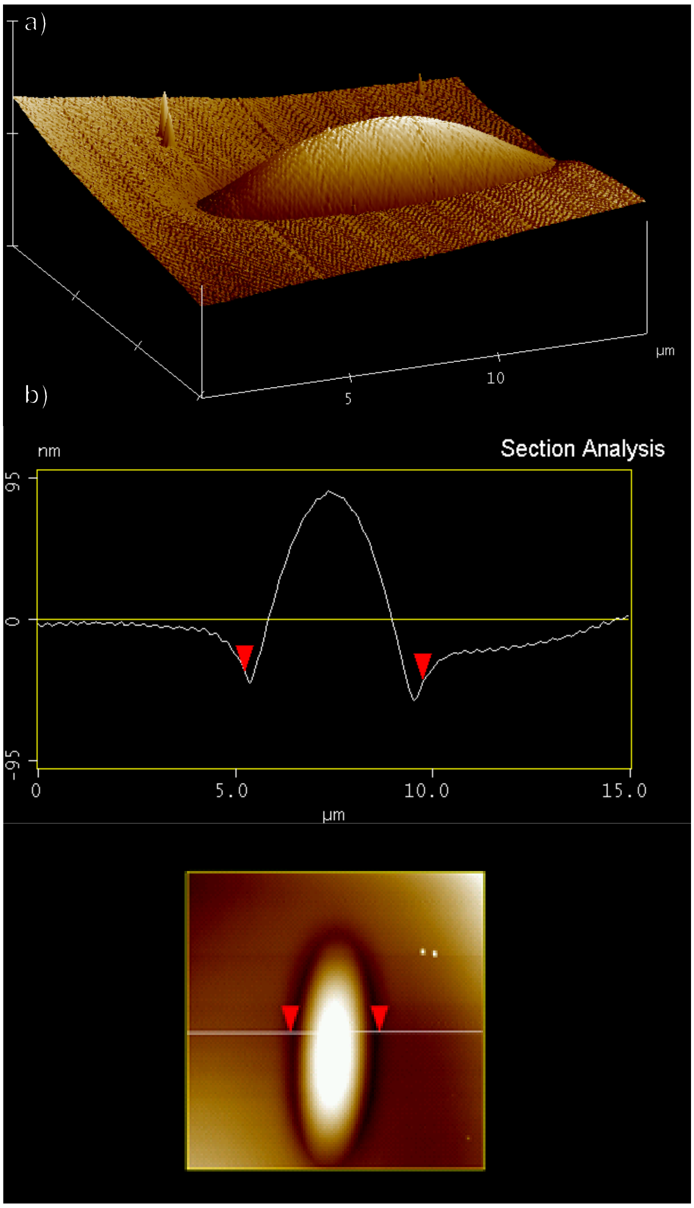

Figure 3.20: Oval defect measured under AFM, a) 3-dimensional profile of the defect on the surface, b) the central cross-section of the defect surface profile along [110].

3.4.2.3 Potential Reconstruction

The observed localized polariton states can be related to an effective confinement potential $V_m(\mathbf{r})$ for the in-plane polariton motion. We can estimate $V_m(\mathbf{r})$ using the spectrally integrated density of states $D_m(\mathbf{r})$ created by $V_m(\mathbf{r})$ below the continuum edge as introduced in Sec. 3.4.1.4. The resulting confinement potentials for the investigated PDs are shown in Fig. 3.21. The symmetry of the potentials reflect the symmetry of the localized states.

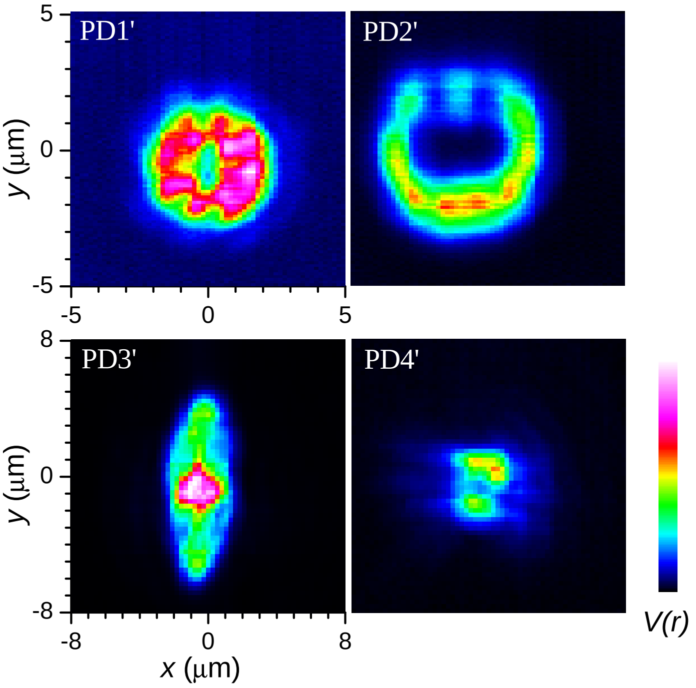

Figure 3.21: Potentials $V_m(\mathbf{r})$ of PDs calculated using formulas as discussed in Sec. 3.4.1.4. The color scale is given, covering 0 to -24 meV for PD1' and PD2' and 0 to -46 meV for PD3' and PD4'.

3.4.2.4 Surface Reconstruction

The series of SEM cross-section images $S(x, y_n, z)$ taken at various y_n (see Figs. 3.15, 3.16, 3.17, 3.19), provide volume information of the defects. To reconstruct the shape of the defects in three dimensions, we determine the position of the interfaces between the GaAs and AlAs layers in the SEM image. We use PD3' (see Fig. 3.17) as an example here. The SEM images show a signal S, which is proportional to the detected secondary electron current, differing by about 10% between AlAs and GaAs surfaces. The RMS noise in S was about 5% of the GaAs signal. SEM images were taken with a nominal magnification between 65600 and 79500. We calibrated the vertical (y) axis to match the nominal Bragg period, yielding pixel sizes between 10 nm and 12 nm with 2% error. The noise of S is limiting the precision with which the layer interface positions can be determined. To enable a reliable fit of the interface positions, we have averaged the data over 5 pixels (60 nm) along x, orthogonal to the growth direction z. The resulting $\bar{S}(x, y_n, z)$ was fitted with a model function $S_\mathrm{m}(z)$ of the epitaxial structure along z. The model assumes a Gaussian resolution of the imaging with a variance of $r/\sqrt{2}$, and a constant thickness d of the $\lambda_\mathrm{c}/4$ AlAs layers, not affected by the defect, which is motivated by the small surface diffusion length of AlAs compared to GaAs. The sequence of L AlAs layers in GaAs is then described by

$$\begin{aligned} S_\mathrm{m}(z) &= a_0 + a_1 z + a_2 z^2 + A \times \\ & \sum_{l=1}^{L} \left[\mathrm{erf}\left(\frac{z - z_l}{r} \right) - \mathrm{erf}\left(\frac{z - z_l - d}{r} \right) \right] . \end{aligned} \tag{3.7}$$

The polynomial coefficients $a_{0,1,2}$ describe the background, A is half the signal difference between AlAs and GaAs, and z_l are the positions of the lower interfaces of the AlAs layers. The layer index l is the AlAs layer number in growth direction. The topmost 3-4 layers were excluded from the fitted region as the background varied strongly due to the change in secondary electron collection efficiency (see *e.g.* Fig. 3.15b). The resolution parameter r was 40 nm corresponding to a FWHM of 67 nm. The fitted layer positions z_l show a noise of a few nm. An example of such a fit is given in Fig. 3.22. Using the $z_l(x, y_n)$ for the different cross-sections n, we can

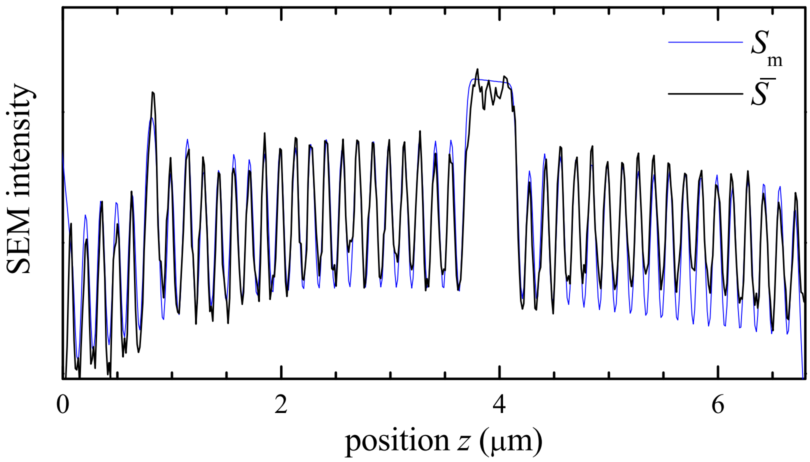

Figure 3.22: Example of a fit (blue line) $S_\mathrm{m}(z)$ to the SEM profile $\bar{S}(z)$ (black line) of PD3', position $(x, y_n) = (1.5\,\mu\mathrm{m}, 2.5\,\mu\mathrm{m})$ in Fig. 3.17. A linear offset has been subtracted for better visibility.

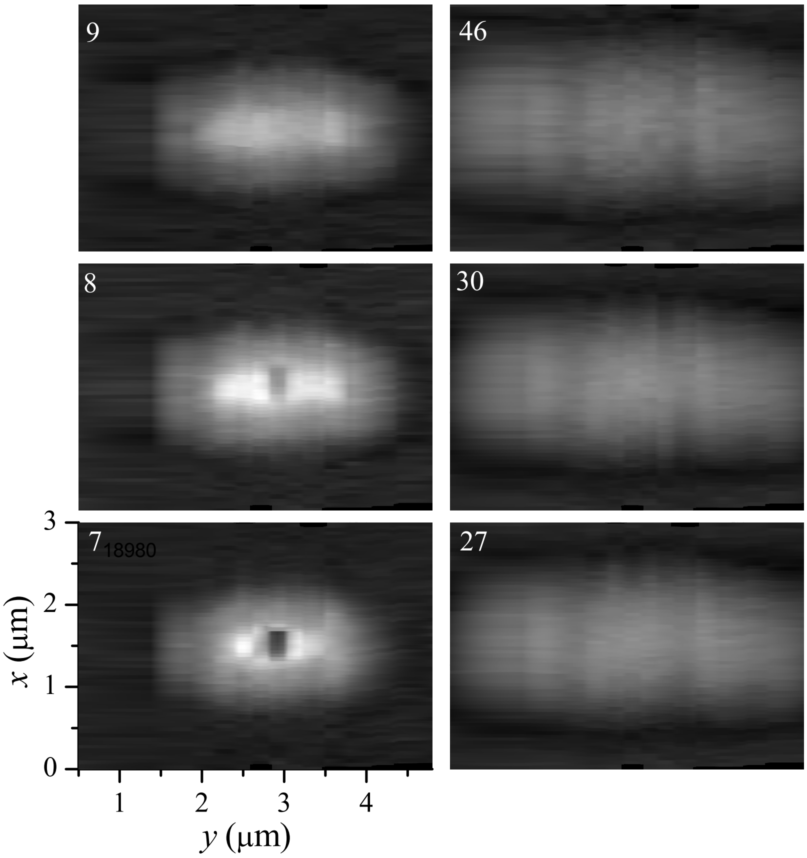

Figure 3.23: Height maps of AlAs layers in PD3'. The sequential numbers of the layers n are given. Linear grey scale from -20 nm (black) and +140 nm (white) relative to the nominal layer position. The layer 7 is the first above the GaAs layer containing the droplet, layer 27 is the first layer above the 2λ GaAs cavity layer, and layer 46 is the last fitted layer.

reconstruct height maps of the AlAs layers within the structure across x and y. A linear slope and an offset along x were subtracted from each $z_l(x, y_n)$ of an individual cross-section n to reproduce the nominal position outside the defect.

The height maps of PD3' reconstructed from 15 cross-sections (see lines in Fig. 3.17, not all shown) are displayed in Fig. 3.23. The evolution of the surface modulation can be followed. The first layer above the defect source ($l = 7$) shows the center depression of the GaAs, similar to what observed in liquid droplet epitaxy [73]. Two maxima of the thickness are observed along the preferential surface diffusion direction $[1\bar{1}0]$. With increasing layer number, first the depression disappears ($l = 9$), followed by a general extension and flattening of the structure. By integrating height profiles of defect for different cuts we have determined the volume of the additional GaAs material as constant within the error. From this volume, we can deduce the radius of the deposited Ga droplet which is 86 ± 6 nm.

3.4.2.5 Growth kinetics

For all of the 15 PDs investigated by FIB/SEM in this work, of which four have been shown as examples, we find a similar origin - a local increase in a GaAs layer thickness with a depression in the center. The additional GaAs volume can only be created by a local deposition of Ga, as the growth is limited by the group III element, while the group V element As is provided in a much larger amount given by the V/III flux ratio of about 50, and desorbs if not bound to the surface with a Ga atom to form GaAs. The only available source for this excess Ga deposition are Ga droplets from the Ga source.

The shapes of the polariton potentials created by the PD are a consequence of the Ga droplet size, and its deposition position relative to the cavity layer. In order to simulate the 0-dimensional polariton states quantitatively, a full three-dimensional simulation of the mode structure in the cavity would be needed, which is beyond the scope of the present work. For a qualitative argument, one can use a first-order perturbation picture. The polariton intensity is decaying exponentially into the Bragg mirror with a decay length of about 400 nm. For PD2', the GaAs layer thickening is 50 nm, but it is separated by 23 DBR periods, about 3 μm, or 8 decay lengths from the cavity, where the polariton intensity has decayed to 0.02%. This results in a small influence to the polaritons and a small localization energy of the ground state of 5 meV. For this defect we observe a large central crater and DBR layer discontinuities, as can be seen on the central cut in Fig. 3.15. This could give rise to a repulsive central part of the PD2' potential as observed in Fig. 3.10.

In PD1', the Ga droplet had a similar size as in PD2' (GaAs thickening 90 nm), but it hit the surface only three DBR periods above the cavity layer. Even though the induced structural perturbation propagates away from the cavity layer, is has a much larger influence, with the third excited state at -9 meV and an estimated ground state confinement energy of 20 meV. The significantly smaller lateral extension of the defects in MC2 leads to a larger height of the perturbation, which in turn results in stronger confinement of polariton states with shapes as seen for PD3' and PD4'.

The evolution of the defect structure during growth can be pictured as follows. After a Ga droplet was deposited on the surface, Ga diffuses over the surface from the droplet to the surrounding areas. Due the large V-III flux ratio, there is sufficient surplus of As_2 impinging onto the surface to convert the diffusing Ga into GaAs, leading to an additional GaAs thickness which decays with the distance from the deposition spot, according to the Ga diffusion length. The depression in the center of the resulting profile is due to reduced GaAs growth below the Ga droplet, which requires the diffusion of As through the Ga droplet to the GaAs surface. Once the droplet has been consumed, the subsequent GaAs growth generally tends to smooth the surface due to the Ga surface diffusion and the preferential attachment of Ga at monolayer steps, which have a density proportional to the surface gradient for gradients superseding the gradient due to monolayer islands (for a island size of 20 nm a gradient of 1%). Al instead has a much shorter diffusion length, and therefore the surface profile is essentially conserved during the growth of the AlAs layers. For Ga grown on (001) oriented substrate at 590°C at a V/III flux ratio of 2 and a growth rate of 0.25 μm/h the diffusion length was reported[32] to be 1 μm and 0.02 μm for Ga and Al, respectively.

The observed PD anisotropy of 1:2 to 1:3 along the [110]:[1$\bar{1}$0] directions for MC2 grown at a temperature of 590°C reduces to less than 1:1.1 for MC1 grown at 715°C. This finding can be explained by temperature dependent diffusion lengths D for these two crystallographic directions. In [74] $D_{[1\bar{1}0]} = 4D_{[110]}$ was found resulting in diffusion lengths of $L_{[1\bar{1}0]} = 2L_{[110]}$ for a V/III flux ratio of 1.5 and growth temperatures in the range of 600°C, in agreement with the aspect ratio of the defects found in MC2. The reduction of the anisotropy for the higher growth temperature of MC1 indicates an activated diffusion with different activation energies in the two directions. At higher temperatures, the thermal energy supersedes the activation energies and a kinetically limited isotropic diffusion is recovered. The presence of different activation energies for diffusion in the two crystallographic directions is plausible as during growth the GaAs surface shows a reconstruction [75] giving rise to a channel-like structure along [1$\bar{1}$0].

3.5 CONCLUSIONS

We have shown that oval or round defects in MBE grown GaAs microcavities create zero-dimensional polariton states of narrow linewidths. We have revealed their three-dimensional structure and their formation mechanism, an impinging Ga droplet during growth. While we have deduced effective confinement potentials for the defects, a quantitative modeling of the polariton spectra from the three-dimensional structural information obtained by the FIB/SEM data is presently missing. In the context of polaritonic devices [7] our work indicates an approach to manufacture two-dimensional polaritonic traps by intentional creation of Ga droplets at a specific position during the MBE growth of a microcavity, rather than ex-situ etching as described in [76].

This can be done by Ga droplet epitaxy [77] with a low density to create well-defined localized polariton states in microcavities. The narrow linewidths of the polariton states formed in this way are favorable for zero-dimensional polariton switches after Ref. [78].

4 Strain compensation

4.1 Strain in GaAs/AlAs microcavities

The lattice constants of GaAs and AlAs layers differ by 0.14% at room temperature, leading to strain in AlAs layers grown on GaAs substrates, which for a film thickness above a critical thickness [45] relaxes by the formation of a cross-hatch dislocation pattern. In GaAs/AlAs microcavities, such cross-hatches influence the propagation of polaritons, and give rise to the elastic scattering and the appearance of a cross-shaped signature in the far-field emission from a microcavity [41, 79–82]. Furthermore, they can cause a localization of polariton condensates observed in such microcavities in the strong coupling regime [3]. In order to observe polariton fluid propagation over distances exceeding hundreds of μm, and spontaneous vortex dynamics in a homogeneous polariton superfluid, the cross-hatch pattern needs to be suppressed. One possibility to reduce the strain and thus avoid misfit dislocation formation is p or n-type doping with small atoms [83], such as carbon or silicon, respectively. This can be used in electrically pumped structures such as vertical cavity surface emitting lasers (VCSELs). However, the doping gives rise to free-carrier absorption, limiting the lifetime and thus the propagation length of polaritons. Moreover, the doping introduces electric fields which cause energy shifts of the quantum well (QW) excitons due to the Stark effect, and free carriers which broaden the QW exciton due to carrier-exciton scattering. In the following section, we propose and demonstrate the suppression of the cross-hatch dislocation pattern by the incorporation of strain compensating AlP layers into the AlAs layers of the DBRs.

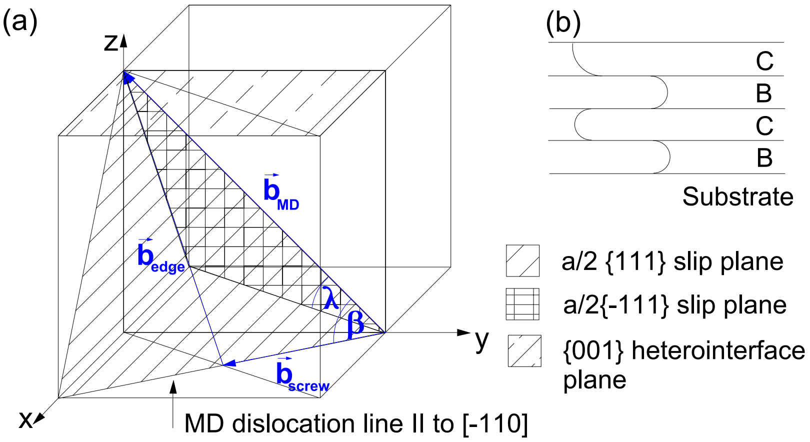

Figure 4.1: a) Sketch of the MD development in GaAs/AlAs heterostructures. The angle between the dislocation line and its Burgers vector is $\beta = 60°$, and the angle between the Burgers vector and a line in the plane of the heterointerface perpendicular to the dislocation line is $\lambda = 60°$. b) Sketch of the dislocation array development on the (111) slip plane, B and C denote different layers.

4.2 STRAIN RELAXATION BY DEVELOPMENT OF CROSS-HATCHES

Thin films of cubic semiconductors grown on (001) substrates with a moderate lattice mismatch $\varepsilon_{\mathrm{m}} < 2\%$ grow in a layer-by-layer mode. For layer thicknesses exceeding the critical thickness [45], the strain relaxes by the formation of misfit dislocation arrays. A misfit dislocation (MD) is a mixed edge and screw dislocation [84], as shown in Fig. 4.1a) where the Burgers vector $\mathbf{b}_{\mathrm{MD}}$ of the MD is decomposed into an edge dislocation ($\mathbf{b}_{\mathrm{edge}}$), and a screw dislocation ($\mathbf{b}_{\mathrm{screw}}$). The MD line lies in the heterointerface plane, while the accompanying threading dislocation (TD) line lies in a plane perpendicular to the heterointerface. TDs either propagate from the substrate or are created in the epilayers. In GaAs/AlAs multilayers, the TDs propagation from the substrate is suppressed [49] by a deflection into the interface plane along the $\langle 110\rangle$ directions.

The mechanism behind the formation of the hatches parallel to the $[1\bar{1}0]$ and $[110]$ directions was identified in Ref. [45] for GaAs/GaAs$_{0.5}$P$_{0.5}$ heterostructures grown on a (100) GaAs substrate with $\varepsilon_{\mathrm{m}} = 1.8\%$. Using TEM and SEM, bending of threading dislocations on the heterointerfaces on {111} slip planes was observed, providing a mechanism for the formation of MD arrays sketched in Fig. 4.1b. Following the notation given in Fig. 4.1a, the critical thickness is deduced by comparing strain force

Parameter	GaAs	AlAs	AlP
a (nm)	0.56533 [85]	0.566162 [85]	0.54635 [14]
α (10^{-6}/K)	6.24 [85], 6.86 [85]	5.2 [86]	4.5 [9]
n	3.567 [13]	2.97 [13]	2.775 [87]

Table 4.1: GaAs, AlAs, and AlP lattice constants a, thermal expansion coefficients α and refractive indices n at 850 nm wavelength at room temperature.

of the grown layer to the line tension of misfit dislocation, and is written as [45]

$$h_{\mathrm{c}} = \frac{b}{4\pi\varepsilon_{\mathrm{m}}}\left(1+\ln\frac{h_{\mathrm{c}}}{b}\right)\frac{1-\nu\cos^2(\beta)}{(1+\nu)\cos(\lambda)} \tag{4.1}$$

where $b = |\mathbf{b}|$, we took $\mathbf{b} = \mathbf{b}_{\mathrm{MD}}$, $\varepsilon_{\mathrm{m}} = (a_{\mathrm{s}} - a_{\mathrm{f}})/a_{\mathrm{f}}$ is the misfit strain where a_{s} and a_{f} are the lattice constants of the substrate and the film respectively, $\nu = C_{12}/(C_{11}+C_{12})$ is the Poisson ratio of the film, β is the angle between the dislocation line and $\mathbf{b}$, and λ is the angle between $\mathbf{b}$ and the direction in the film plane perpendicular to the intersection of the slip plane with the interface.

Due to the different thermal expansion coefficients α of GaAs and AlAs (see Table 4.1), they are expected to be lattice matched [86] around 900°C. The critical thickness for the growth of AlAs on a GaAs substrate at a temperature of 590°C calculated using Eq.(4.1) is $h_{\mathrm{c}} \sim 0.6\,\mu$m, with $b = a/\sqrt{2}$ as shown in Fig. 4.1a. For a full GaAs/AlAs Bragg period instead, using its average lattice constant, we find $h_{\mathrm{c}} \approx 1.1\,\mu$m.

Strain relaxation occurs gradually with increasing thickness $h > h_{\mathrm{c}}$, creating an equilibrium MD density [84]

$$\rho_{\mathrm{MD}} = \frac{\varepsilon_{\mathrm{m}}}{b_{||}}\left(1-\frac{h_{\mathrm{c}}}{h}\right) = \frac{\varepsilon_{\mathrm{m}}}{b_{||}}R\,, \tag{4.2}$$

where $b_{||} = b\,cos\,(\lambda)$ and R being the fractional strain relaxation. For a AlAs/GaAs Bragg mirror of $h = 3.5\,\mu$m, we find $\rho_{\mathrm{MD}} = 2/\mu$m corresponding to $R = 68\%$. We measured a cross hatch density of $\rho_{\mathrm{MD}} \sim 30$/mm, corresponding to $R = 1.5\%$. The MD formation thus remained far from equilibrium during the growth.

However, even this small MD density is affecting the polariton propagation in the MC. In order to reduce the MD density one needs to reduce the lattice mismatch of the DBR.

P content in $\mathrm{AlAs}_{1-x}\mathrm{P}_x$ (%)	0	1	1.5	2	3
AlP layer thickness (nm)	0	0.8	1.1	1.5	2.2
matching temperature (°C)	1100	830	700	560	300
cavity mode wavelength λ_c (nm)	866	873	851	856	855

Table 4.2: Parameters of the investigated microcavity samples

4.3 Cross-hatches suppression by strain compensation of DBRs

In order to suppress cross-hatches, we grow $\mathrm{AlAs}_{1-x}\mathrm{P}_x$ to obtain an effective lattice matched ternary alloy as low index layer. $\mathrm{AlAs}_{1-x}\mathrm{P}_x$ is grown as a pseudo-alloy, namely, a superlattice of binaries AlAs and AlP instead of ternary alloy. For sufficiently thin layers resulting material has a bulk properties[31]. Thin AlP layer is sandwiched into the center of each AlAs layer of the DBR. This growth procedure provides a better control over the composition, specifically for the group V alloys. Additionally, we avoid interfaces in which elements of both groups III and V change, which can lead to interface layers modifying the band offset. Furthermore, by adding the lower index material AlP in the center of the low index layer, we enhance its reflectivity.

The values of the phosphorus fraction x used in our study were chosen to lattice-match $\mathrm{AlAs}_{1-x}\mathrm{P}_x$ to GaAs at different temperatures as given in Table 4.2. The temperature dependent lattice constant $a(T)$ was calculated using the linear thermal expansion

$$a(T) = a(T_0)(1 + \alpha(T - T_0)) \tag{4.3}$$

where α is the thermal expansion coefficient. Using α_GaAs from Ref. [85], GaAs and AlAs are lattice matched at $T = 1400$°C, while for α_GaAs from Ref. [86] they are matched at $T = 900$°C. In the sample design, we used the average of both values. The lattice constant of the ternary alloy was calculated using Vegard's law for the lattice constants of the binary alloys and thermal expansion coefficients as listed in Table 4.1. Five microcavity samples with nominal phosphorus contents of $x = 0..3\%$ were grown (see Table 4.2). They consist of a bare $2\,\lambda_\mathrm{c}$ GaAs cavity layer surrounded by $\mathrm{AlAs}_{1-x}\mathrm{P}_x$/GaAs DBRs with 26 and 23 $\lambda_\mathrm{c}/4$ pairs on the bottom and top, respectively. The calculated temperature dependence of the lattice mismatch ε_m of $\mathrm{AlAs}_{1-x}\mathrm{P}_x$ corresponding to the different samples is shown in Fig. 4.2a.

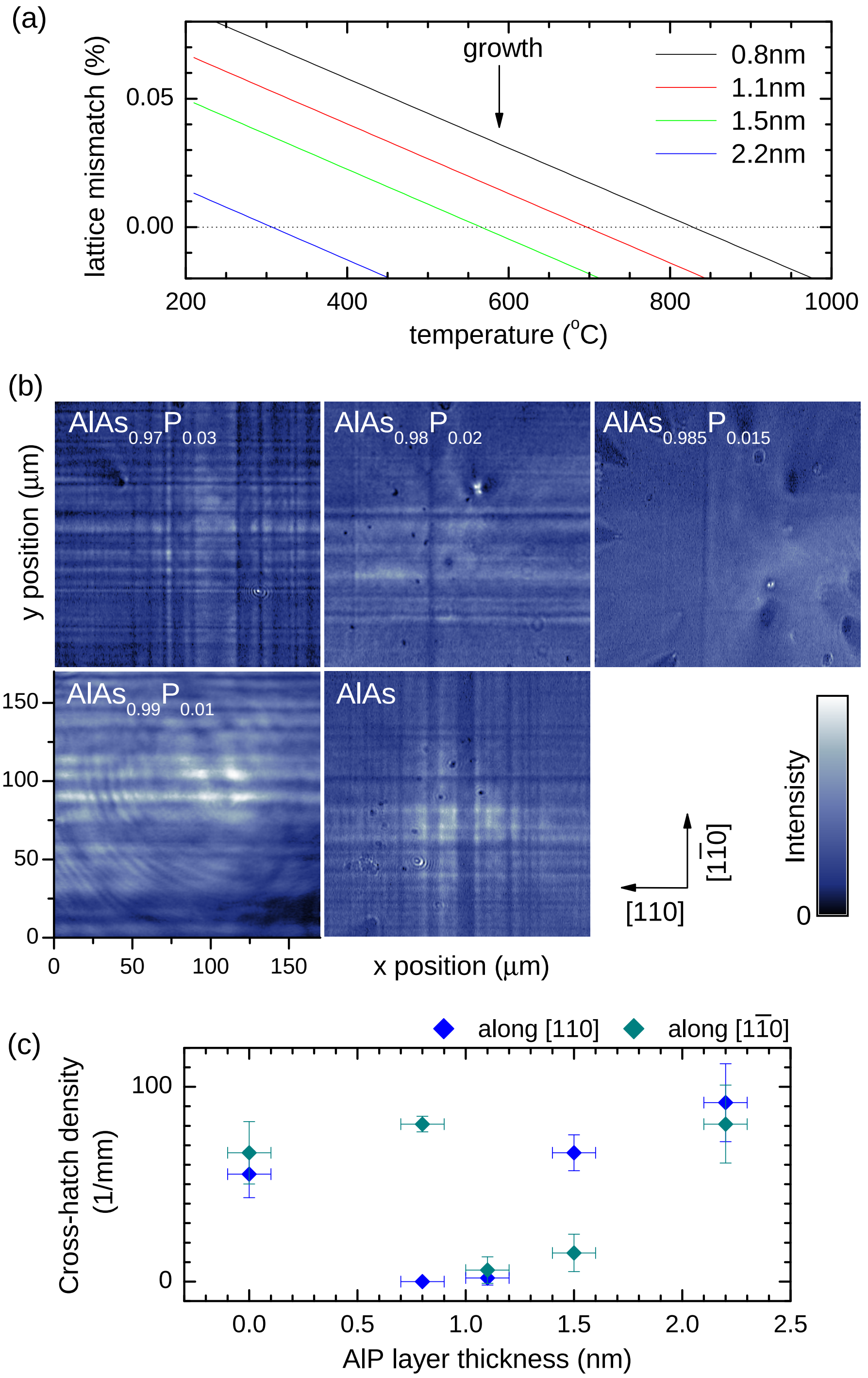

Figure 4.2: (a) Calculated temperature dependence of the lattice mismatch ε_m of AlAs$_{1-x}$P$_x$ for different AlP layer thicknesses as indicated. Parameters are taken from Table 4.1. (b) Real space transmission images of the investigated microcavities with different strain compensation. Intensity on a linear color scale as indicated. (c) cross-hatch density as function of AlP layer thickness. Error bars for the layer thickness are estimated from the shutter transit times.

Resonant transmission was measured in order to determine the average density of cross-hatches. The samples were held in a bath cryostat at a temperature of $T = 80\,\mathrm{K}$ to avoid GaAs absorption at the cavity resonance. The samples were illuminated from the substrate side and imaged from the epi-side using 0.5NA lenses. A detailed description of the setup can be found in Sec. 3.2.1, and Ref. [23]. The measured cavity mode wavelengths are shown in Table 4.1 and are red detuned by 50-80 meV from the bulk GaAs exciton [29] of the cavity layer at 1.508 eV. The real space transmission images of the samples under illumination with a nearly collimated beam of resonant 150 fs pulses and 250 μm diameter are given in Fig. 4.2b. The observed cross-hatch density shows a clear dependence on the strain compensation. The resulting measured cross-hatch density versus the thickness of the AlP layer (see Fig. 4.2c) shows a minimum at 1.1 nm corresponding to a low index layer of $\mathrm{AlAs_{0.985}P_{0.015}}$, which is nominally lattice matched at 700°C, close to the growth temperature of 590°C. Furthermore, the density reduction has a wider range for the $[1\bar{1}0]$ compared to the [110] direction. The non-equivalence of the two directions can be related to the breaking of the inversion symmetry by the lattice basis, and is not observed in Si/SiGe structures [88]. The varying density of point-like defects seen in the images - specifically the high density in the $\mathrm{AlAs_{0.985}P_{0.015}}$ sample is attributed to a faulty lip heater in the Ga Veeco 'SUMO' cell of the VG V90 MBE (molecular beam epitaxy) machine. The influence of such defects on the polariton states are characterized in Ref. [23].

4.4 Polariton propagation in strain compensated structures

To exemplify the effect of the suppressed cross-hatch disorder on the polariton states, we compare in Fig. 4.3 the polariton propagation in 0% and 1.5% samples. Without disorder, they exhibit a in-plane quadratic dispersion with a minimum at the band edge $\hbar\omega_\mathrm{c}$ at 1.4330 (1.4565) eV for the 0% (1.5%) sample, respectively, and an effective mass of $m = 2 \times 10^{-5}\, m_\mathrm{e}$ determined from the measured dispersion, where m_e is the free electron mass. We use a focussed excitation with a diffraction limited spot of about 25 μm size, containing wavevectors $|\mathbf{k}| < 0.3/\mu\mathrm{m}$. Exciting with a cw-laser at the polariton band-edge, we select the polariton states close to zero momentum. The excited polariton states (Fig. 4.3a) are strongly affected by the cross-hatch disorder, being localized between hatches. In the 1.5% sample instead, the virtual absence of the cross-hatch disorder enables the nearly free propagation of the excited polaritons. The interference fringes created by the scattering from the defects show a period of about 20 μm, corresponding to $|\mathbf{k}| = 0.16/\mu\mathrm{m}$, and a kinetic energy of 47 μeV. The

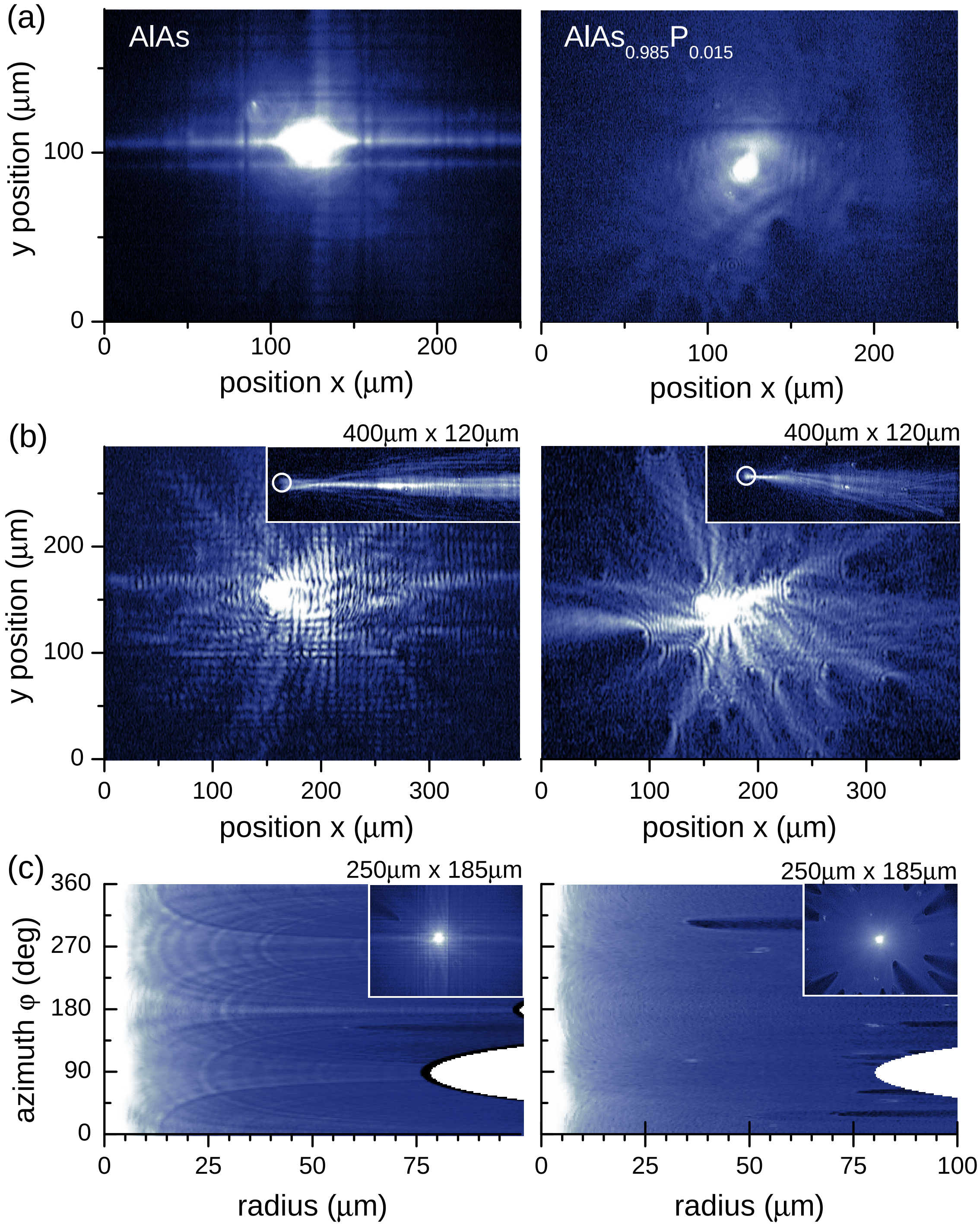

Figure 4.3: Real space transmission images of the samples with no strain compensation (left column) and optimum strain compensation (right column). Color scale as in Fig. 4.2. Excitation energy relative to band edge were 0 meV in (a), 1 meV in (b), 6 meV in the inset of (b), and 0-10 meV in (c). Excitation wavevectors were $|\mathbf{k}| < 0.3/\mu$m in (a), $|\mathbf{k} - (1.1, 0)/\mu\mathrm{m}| < 0.3/\mu$m in (b), $|\mathbf{k} - (2.3, 0)/\mu\mathrm{m}| < 0.3/\mu$m in the inset of (b), and $|\mathbf{k}| < 4/\mu$m in (c). Dislocation distribution is spatially anisotropic what give rise to anisotropic polariton propagation from the excitation spot along $[1\bar{1}0]$ and [110] directions, compare plot in c) first column for 0° and 90°,180°,270° angles.

free propagation at such a low kinetic energy gives an upper limit of about 20 μeV for the residual disorder taking into account accuracy with which we could estimate kinetic energy. The single horizontal MD hatch present in the investigated region leads to the reduction of the emission in the hatch, evidence for an attractive potential increasing the local wavevector and a group velocity and thus reducing the polariton density in the hatch. Tuning the excitation energy about 1 meV above the polariton bandgap, polaritons propagate over distances in the order of 200 μm as seen in Fig. 4.3b. Polaritons excited with even higher kinetic energies of 6 meV and a wavevector $\mathbf{k}$ centered at $(2.3, 0)/\mu$m (see insets of Fig. 4.3b, the excitation position is indicated as a circle) propagate over hundreds of micrometers in the x direction. Fitting the data we deduced exponential decay lengths in the order of 1 mm. In the 0% sample, the propagation proceeds along the waveguide channels [41] provided by the cross-hatches, while in the 1.5% sample, the excited wavepacket is spreading according to its free propagation. Exciting instead with 150 fs pulses covering kinetic energies from zero to 10 meV, and focusing in real space to a diffraction limited spot of 1.5 μm size covering $|\mathbf{k}| < 4/\mu$m, polaritons with a large range of kinetic energies are propagating away from the excitation spot (see inset of Fig. 4.3c). The interference pattern is suppressed by the short coherence length of the excited polariton wavepacket. To observe the omnidirectional propagation, we show the data in cylindrical coordinates centred at the excitation spot in Fig. 4.3c. In the 0% sample the propagation is anisotropic with the longest propagation length along the hatch directions $[1\bar{1}0]$ and $[110]$. In the 1.5% sample instead, an isotropic propagation is observed, apart from the point-like defects.

4.5 CONCLUSIONS

In conclusion, we have proposed and demonstrated the suppression of the cross-hatch disorder in GaAs/AlAs microcavities by strain compensation, which was realized by incorporating thin AlP layers into the AlAs layers of the DBRs. Using an AlP layer thickness of 1.1 nm, corresponding to an effective $\mathrm{AlAs_{0.985}P_{0.015}}$ alloy of the low-index layer, a reduction of the cross hatch density by an order of magnitude is achieved, which reduces the residual polariton disorder potential to the 10 μeV range. This progress is important for the study of intrinsic collective polariton phenomena such as superfluidity, vortices and solitons.

5 POLARITON PARAMETRIC SCATTERING

5.1 PARAMETRIC PROCESSES IN A NONLINEAR CRYSTAL

Parametric process denotes a process in which light interacts with matter such that the initial and final quantum-mechanical states of the matter are identical [89] meaning that there is no energy and momentum transfer between light and matter as opposed to non-parametric processes.

Polarization of a continuous medium is written as a response to an applied electric field E as

$$\begin{aligned} P(t) = \; & \epsilon_0[\chi^{(1)}E(t) + \chi^{(2)}E(t)^2 + \chi^{(3)}E(t)^3 + ...] \\ & = \tilde{P}^{(1)}(t) + \tilde{P}^{(2)}(t) + \tilde{P}^{(3)}(t) + ... \end{aligned} \tag{5.1}$$

where

$$E(t) = E_1 e^{-i\omega_1 t} + E_2 e^{-i\omega_2 t} + c.c. \tag{5.2}$$

and $\chi^{(i)}$ and $\tilde{P}^{(i)}(t)$, are i-th order susceptibility and polarization respectively, ϵ_0 is the permittivity of a free-space. In the following, we assume that medium is lossless and dispersionless. The above equations are written in a scalar form so that susceptibilities are scalars also. In general, for an anisotropic medium, tensor susceptibilities need to be used. If we consider the second order susceptibility, substituting Eq.(5.2) into Eq.(5.1), we find five frequencies of the polarization of the medium, namely $2\omega_1, 2\omega_2, \omega_1 + \omega_2,\ \omega_1 - \omega_2, 0$ which describe processes of the second harmonic generation (SHG) for ω_1 and ω_2, sum-frequency generation (SFG), difference-frequency generation (DFG) and optical rectification (OR, static electric field created across the nonlinear crystal), respectively. Usually, one from above processes will be dominant in the created field resulting from the phase matching conditions for constituent waves[89].

For DFG process energy, conservation requires that $\omega_3 = \omega_1 - \omega_2$, see Fig. 5.1. When the field with frequency ω_2 is already present in the material, it will be amplified by the DFG and is called *parametric amplification*. When there are no photons with ω_2, ω_3 frequencies, and parametric process is spontaneously initiated it is called *parametric fluorescence*. When nonlinear crystal is placed in an optical cavity resonant with ω_2 and/or ω_3 this system is called *optical parametric oscillator* (OPO) with $\omega_1, \omega_2, \omega_3$ called pump, idler and signal frequencies respectively. If the cavity is resonant with all three frequencies it is called triply resonant optical parametric oscillator.

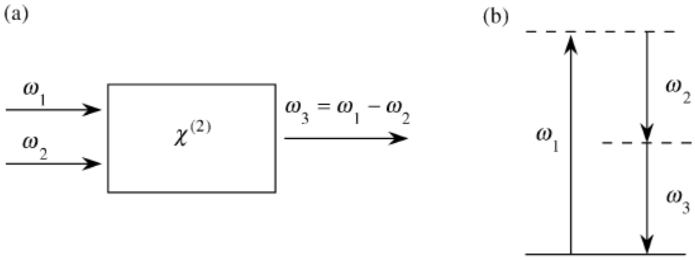

Figure 5.1: a) sketch of DFG process, b) energy level diagram of DFG.

5.2 PARAMETRIC SCATTERING OF MICROCAVITY POLARITONS

The parametric scattering of microcavity polaritons is described in the lowest order by the third-order susceptibility which is a four photon process. Given a coherent population of pump (P) polaritons, which are scattered into signal (S) and idler (I) polaritons[1], the phase matching in time and space results in the conservation of energy $2E_\mathrm{P} = E_\mathrm{S} + E_\mathrm{I}$, and momenta $2\mathbf{k}_\mathrm{P} = \mathbf{k}_\mathrm{S} + \mathbf{k}_\mathrm{I}$ where $\mathbf{k}$ is the wavevector. Polaritons scatter into eigenstates of the system $E_\mathrm{LP}(\mathbf{k}), E_\mathrm{MP}(\mathbf{k}), E_\mathrm{UP}(\mathbf{k})$ with $B = \{LP,\ MP,\ UP\}$ denoting polariton lower, middle and upper branches[2].

Polariton optical parametric amplifier (OPA) was reported in Ref. [90] for a system of 2-dimensional excitons-polaritons in a structures consisting of InGaAs/GaAs quantum wells in a GaAs cavity embedded between GaAs/AlAs Bragg reflectors. Polaritons were resonantly excited and probed with pulsed laser in a time-resolved pump-probe configuration. Probe amplification was observed for a pump at the magic angle

---

[1] Notation denoting P, S, I for pump, signal and idler polaritons is used hereafter in this chapter.

[2] Notation denoting LP, MP, UP for lower, middle and upper polariton branches is used hereafter in this chapter.

for which energy and momentum conserving scattering is satisfied for signal polaritons according to the condition $\mathbf{k}_{\mathrm{I}} = 2\mathbf{k}_{\mathrm{P}}$, $\mathbf{k}_{\mathrm{S}} = 0$, $2E_P(\mathbf{k}_{\mathrm{P}}) = E_{LP}(0) + E_{LP}(\mathbf{2k}_P)$ where E_{LP} is the energy of the lower polariton branch. Bosonic stimulation of pump polaritons by probe polaritons was deduced experimentally from the observation of an exponential dependence of the gain on the pump power above the pump threshold power. This effect originates from the bosonic enhancement, namely $\frac{dN_{final}}{dt} \propto (1 + N_{\ final})N_{pump}$, where N_{final} denotes the polariton population at the probe wavevector, N_{pump} polariton population at the pump wavevector.

CW pump-probe experiments on microcavity polaritons in OPO and OPA regimes were reported in Ref [91] demonstrating multiple scattering of polaritons.

A theoretical model describing spontaneous parametric fluorescence was discussed in Ref. [92], and extended to describe stimulated emission in Ref. [26]. This model is used here, a detailed discussion is given in Sec. 5.3.

Spontaneous parametric emission was experimentally investigated in Ref. [93, 94] providing evidence of scattering within phase-matched directional 8-shapes which were further explored as the entangled photon sources [94, 95] for the purpose of quantum information processing[96**?**]. Experiment reported in Ref. [93] was done with pulsed excitation at lower polariton branch above magic angle. Luminescence was detected temporary and directionally resolved. The energy mismatch, defined as $\hbar\omega_\delta(\mathbf{k}) = |E_{LP}(\mathbf{k}_{\mathrm{S}}) + E_{LP}(2\mathbf{k}_{\mathrm{P}} - \mathbf{k}_{\mathrm{S}}) - 2E_{LP}(\mathbf{k}_{\mathrm{P}})|$, imposes a limit on the polariton linewidth above which 8-shapes are not resolved. For the sample used in that study $|\hbar\omega_\delta(\mathbf{k})|$ was between 0.1 and 0.5 meV depending on $\mathbf{k}_{\mathrm{P}}$, while the exciton broadening in the sample was 60 μeV. Dynamics of the polariton scattering within the 8-shapes was also modeled theocratically, good agrement between theory and experiment was

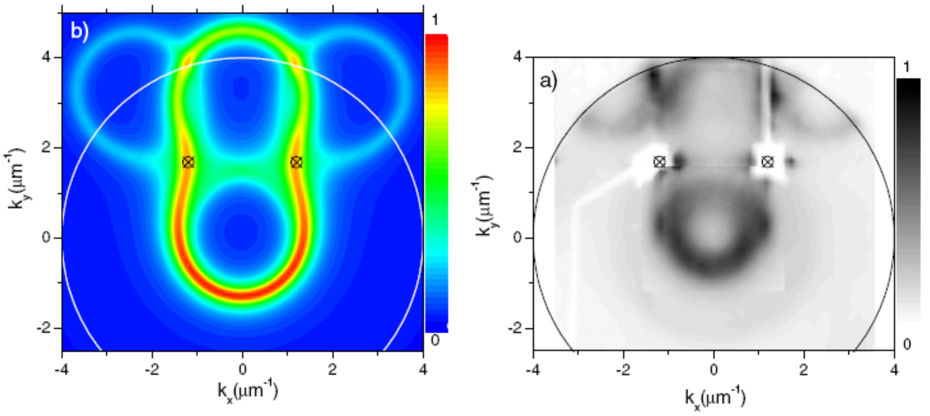

Figure 5.2: Theory (left) and experiment (right) on polariton complimentarily after Ref. [95]

found.

In Ref. [95], quantum correlations of microcavity polaritons were discussed both theoretically and experimentally. Parametric scattering of polaritons from two coherently excited pump states at magic angles $\{\mathbf{k}_{\mathrm{P}}, -\mathbf{k}_{\mathrm{P}}\}$ into two corresponding idlers $\{\mathbf{k}_{\mathrm{I}}, -\mathbf{k}_{\mathrm{I}}\}$ was considered. Interference at idlers was recorded as a function of relative phase-shift between the two pumps, compare Fig. 5.2. The quantum origin of the interference was verified by the time resolved measurement of interference fringes visibility, it agreed with theoretical predictions derived from quantum theory.

Measurements demonstrating an intrabranch OPO in a 2-dimensional semiconductor triple-microcavity in the weak coupling regime were reported in Ref. [97] where signal and idler beams were degenerate in momentum and split in energy. Most recently, the same group demonstrated an interbranch OPO of 1-dimensional exciton-polaritons and measured their time correlation [98, 99]. In this experiment, idler, signal, and pump beams were degenerate in energy and split in momentum, OPO operation was demonstrated in the same microcavity in the strong coupling regime at T=10 K, and in the weak coupling at T=100 K.

5.3 THEORY OF PARAMETRIC SCATTERING OF MICROCAVITY POLARITONS

Theoretical foundations of the parametric scattering of microcavity polaritons excited by a resonant and coherent pump laser were given in Ref. [92] where the following points were addressed: 1) the peculiar dispersion, 2) the line-shape features, 3) the two dimensional directional emission pattern. In this model, there are three contribution to the system Hamiltonian, namely, lower polariton energy (the upper polariton is neglected), polariton-polariton interaction within the lower polariton branch with spin relaxation neglected, and polariton coupling with the external photon reservoir [18, 100]. This Hamiltonian is written as

$$H = H_{LP} + H_{PP}^{eff} + H_{qm} \tag{5.3}$$

where $H_{LP} = \sum_k E_{LP}(k) p_k^\dagger p_k$ describes the lower polariton branch dispersion where $p_{\mathbf{k}}^\dagger$,$p_{\mathbf{k}}$ are polariton creation and annihilation operators.

The polariton-polariton interaction term is

$$H_{PP}^{eff} = \frac{1}{2} \sum_{\mathbf{k},\mathbf{k}',\mathbf{q}} \frac{\lambda_X^2}{A} V_{\mathbf{k},\mathbf{k}',\mathbf{q}}^{PP} p_{\mathbf{k}+\mathbf{q}}^\dagger p_{\mathbf{k}'-\mathbf{q}}^\dagger p_{\mathbf{k}} p_{\mathbf{k}'} \tag{5.4}$$

where λ_X is the exciton Bohr radius, A is the macroscopic quantization area. The interaction potential is

$$V^{PP}_{\mathbf{k},\mathbf{k}',\mathbf{q}} = \{2\left(\hbar\Omega_R/n_{sat}\lambda_X^2\right)\left(|C_{\mathbf{k}+\mathbf{q}}|X_{\mathbf{k}'} + |C_{\mathbf{k}'}|X_{\mathbf{k}+\mathbf{q}}\right) + \left(6e^2/\epsilon\lambda_X\right)X_{\mathbf{k}+\mathbf{q}}X_{\mathbf{k}'}\}X_{\mathbf{k}'-\mathbf{q}}X_{\mathbf{k}} \tag{5.5}$$

where C and X are Hopfield coefficients, n_{sat} is the exciton saturation density, ϵ is the quantum well dielectric constant. The first part of Eq.(5.5) accounts for saturation of the exciton oscillator strength, the second term describes Coulomb interaction between excitons.

The cavity system interacts with an external electromagnetic field through the quasi-mode coupling Hamiltonian [18, 92]

$$H_{qm} = \int d\Omega \left\{ \sum_{\mathbf{k}} gC_k p^{\dagger}_{\mathbf{k}} \alpha_{\mathbf{k},\Omega} + \text{H.c.} \right\} \tag{5.6}$$

where $\alpha_{\mathbf{k},\Omega}$ is the external photon destruction operator of wavevector k and frequency Ω. The spectrum of the polariton luminescence is written using a two-time correlation function[100] of the time-dependent polariton field operator $p_{\mathbf{k}}(t)$ as

$$I^{par}(\mathbf{k},t,\omega) \propto |C_k|^2 \text{Re} \int_0^{+\infty} d\tau e^{-i(\omega\tau)} \langle p^{\dagger}_{\mathbf{k}}(t+\tau) p_{\mathbf{k}}(t)\rangle \tag{5.7}$$

In the steady-state, the photoluminescence simplifies to

$$I^{par}(\mathbf{k},\omega) \propto |C_k|^2 \text{Re}\{\langle \tilde{p}^{\dagger}_{\mathbf{k}}(\omega) p_{\mathbf{k}}(0)\rangle\} \tag{5.8}$$

where $\tilde{p}^{\dagger}_{\mathbf{k}}(\omega) = \int d\tau e^{i\omega\tau} p_k(\tau)$.

To calculate the photoluminescence, we need to determine the time-evolution of the coupled polariton operators $p_{\mathbf{k}_\mathrm{S}}(t)$ and $p_{\mathbf{k}_\mathrm{I}}(t)$ where $\mathbf{k}_\mathrm{I} = 2\mathbf{k}_\mathrm{P} - \mathbf{k}_\mathrm{S}$. The following assumptions are made in order to write equation of motion for polariton populations: (1) only scattering within the lower polariton branch is considered, (2) driving pump has the form $\langle p_{\mathbf{k}_\mathrm{P}}(t)\rangle = e^{-i\omega_P t}|\langle p_{\mathbf{k}_\mathrm{P}}(0)\rangle|$ where $\omega_P = E_P/\hbar$ is the pump frequency, (3) multiple scattering is neglected. The Heisenberg equation of motion [101] for the polariton field neglecting the Langevin terms reads

$$i\hbar\frac{d}{dt}\begin{pmatrix} p_{\mathbf{k}_\mathrm{S}}(t) \\ p^{\dagger}_{\mathbf{k}_\mathrm{I}}(t)e^{-i2\omega_P t}\end{pmatrix} = \widehat{M}^{par}_{\mathbf{k}} \begin{pmatrix} p_{\mathbf{k}_\mathrm{S}}(t) \\ p^{\dagger}_{\mathbf{k}_\mathrm{I}}(t)e^{-i2\omega_P t}\end{pmatrix} \tag{5.9}$$

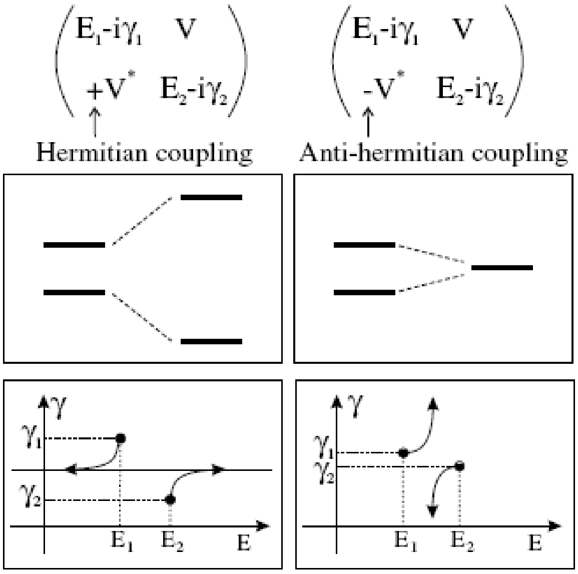

Figure 5.3: Schematic comparison of the Hermitian (left side) and anti-Hermitian coupling (right side) between two damped oscillators. The Hermitian (anti-Hermitian) coupling produces level repulsion (attraction) with increasing interaction energy $|V|$. The evolution of the eigenvalues in the complex plane is also shown at the bottom, after Ref. [26].

where the coupling matrix is

$$\widehat{M}^{par}_{\mathbf{k}} = \begin{pmatrix} \widehat{E}_{\mathrm{LP}}(\mathbf{k}_{\mathrm{S}}) & E^{\mathrm{int}}_{\mathrm{LP}} P_P^2 \\ -(E^{\mathrm{int}}_{\mathrm{LP}} P_P^2)^* & 2E_P - \widehat{E}^*_{\mathrm{LP}}(\mathbf{k}_{\mathrm{I}}) \end{pmatrix} \tag{5.10}$$

which has eigenvalues $\widehat{E}^{\pm}_{\mathrm{LP}}(\mathbf{k}_{\mathrm{S}})$, where

$$\widehat{E}_{\mathrm{LP}} = E_{LP} - i\gamma_{\mathrm{LP}} + 2V^{PP}_{\mathbf{k}_{\mathrm{P}},\mathbf{k}_{\mathrm{P}},0}|P_P|^2 \tag{5.11}$$

with $P_P = \frac{\lambda_X}{\sqrt{A}}\langle p_{\mathbf{k}_{\mathrm{P}}}\rangle$, where λ_X is the exciton Bohr Radius, A is the macroscopic quantization area, while the interaction term is given by

$$E^{\mathrm{int}}_{\mathrm{LP}} = (V^{PP}_{\mathbf{k}_{\mathrm{P}},\mathbf{k}_{\mathrm{P}},\mathbf{k}-\mathbf{k}_{\mathrm{P}}} + V^{PP}_{\mathbf{k}_{\mathrm{P}},\mathbf{k}_{\mathrm{P}},\mathbf{k}_{\mathrm{P}}-\mathbf{k}})/2 \tag{5.12}$$

The coupling to external photons is responsible for the radiative damping $\gamma_{\mathbf{k}} = 2\pi g^2|C_{\mathbf{k}}|^2/\hbar$.

The $\widehat{M}^{par}_{\mathbf{k}}$ coupling matrix is anti-Hermitian. For a Hermitian matrix, for example the exciton-photon interaction Hamiltonian in a microcavity Eq.(1.21), the two coupled modes anti-cross for an increasing interaction term, i.e. the real part of the eigenvalues repel while the imaginary parts tend to a mean value. For an anti-Hermitian matrix, the real parts of eigenvalues attract while the imaginary parts split apart A consequence, one of the mode is overdamped, while the other one is narrowed and can undergo amplification.

The equation of motion for the signal population reads

$$\frac{d}{dt}N(\mathbf{k}_{\mathrm{S}},t)=-\frac{2\gamma_{LP}(\mathbf{k}_{\mathrm{S}})}{\hbar}N(\mathbf{k}_{\mathrm{S}},t)+\frac{2}{\hbar}\Im\{E^{\mathrm{int}}_{\mathrm{LP}}P_P^2e^{-i2\omega_Pt}\langle p^{\dagger}_{\mathbf{k}_{\mathrm{S}}}(t)p^{\dagger}_{\mathbf{k}_{\mathrm{I}}}(t)\rangle\} \tag{5.13}$$

where the signal population $N(\mathbf{k}_{\mathrm{S}},t)=\langle p^{\dagger}_{\mathbf{k}_{\mathrm{S}}}(t)p_{\mathbf{k}_{\mathrm{S}}}(t)\rangle$, is driven by the *anomalous* quantum correlation $\langle p^{\dagger}_{\mathbf{k}_{\mathrm{S}}}(t)p^{\dagger}_{\mathbf{k}_{\mathrm{I}}}(t)\rangle$ which has time evolution

$$\begin{aligned} i\hbar\frac{d}{dt}\langle p^{\dagger}_{\mathbf{k}_{\mathrm{S}}}(t)p^{\dagger}_{\mathbf{k}_{\mathrm{I}}}(t)\rangle &= (-\widehat{E}^{*}_{\mathrm{LP}}(\mathbf{k}_{\mathrm{S}})-\widehat{E}^{*}_{\mathrm{LP}}(\mathbf{k}_{\mathrm{I}}))\langle p^{\dagger}_{\mathbf{k}_{\mathrm{S}}}(t)p^{\dagger}_{\mathbf{k}_{\mathrm{I}}}(t)\rangle \\ &- E^{\mathrm{int}}_{\mathrm{LP}}P_P^{*2}e^{i2\omega_Pt}[1+N(\mathbf{k}_{\mathrm{S}},t)+N(\mathbf{k}_{\mathrm{I}},t)] \end{aligned} \tag{5.14}$$

In order to extract steady state photoluminescence, the equations of motion Eq.(5.9) are rewritten in Fourier space with the solution

$$\tilde{p}_{\mathbf{k}_{\mathrm{S}}}(\omega)=i\hbar\frac{\Delta_{\mathrm{LP}}(\mathbf{k}_{\mathrm{S}},\omega)p_{\mathbf{k}_{\mathrm{S}}}(0)+E^{\mathrm{int}}_{\mathrm{LP}}(\mathbf{k}_{\mathrm{S}})P_{\mathrm{P}}^2p^{\dagger}_{\mathbf{k}_{\mathrm{I}}}(0)}{(\hbar\omega-\widehat{E}^{+}_{\mathrm{LP}}(\mathbf{k}_{\mathrm{S}})(\hbar\omega-\widehat{E}^{-}_{\mathrm{LP}}(\mathbf{k}_{\mathrm{S}}))} \tag{5.15}$$

where the emission detuning $\Delta_{\mathrm{LP}}(\mathbf{k}_{\mathrm{S}},\omega)=\hbar\omega+\widehat{E}^{*}_{\mathrm{LP}}(\mathbf{k}_{\mathrm{I}})-2E_{\mathrm{P}}$.

The steady-state polariton photoluminescence is deduced as

$$\begin{aligned} &I^{par}(\mathbf{k}_{\mathrm{S}},\omega)\propto|C_k|^2\mathrm{Re}\langle\tilde{p}^{\dagger}_{\mathbf{k}_{\mathrm{S}}}(\omega)p_{\mathbf{k}_{\mathrm{S}}}(0)\rangle= \\ &|C_k|^2\times\Im\left\{\frac{\Delta_{\mathrm{LP}}(\mathbf{k}_{\mathrm{S}},\omega)N_{\mathrm{LP}}(\mathbf{k}_{\mathrm{S}})+E^{\mathrm{int}}_{\mathrm{LP}}(\mathbf{k}_{\mathrm{S}})P_{\mathrm{P}}^2A^{*}_{\mathrm{LP}}(\mathbf{k}_{\mathrm{S}})}{\left(\widehat{E}^{+}_{\mathrm{LP}}(\mathbf{k}_{\mathrm{S}})-\hbar\omega\right)\left(\hbar\omega-\widehat{E}^{-}_{\mathrm{LP}}(\mathbf{k}_{\mathrm{S}})\right)}\right\} \end{aligned} \tag{5.16}$$

where the steady-state population $N_{\mathrm{LP}}(\mathbf{k}_{\mathrm{S}})=\langle p^{\dagger}_{\mathbf{k}_{\mathrm{S}}}(0)p_{\mathbf{k}_{\mathrm{S}}}(0)\rangle$ and the parametric correlation amplitude $A_{LP}(\mathbf{k}_{\mathrm{S}})=\langle p^{\dagger}_{\mathbf{k}_{\mathrm{S}}}(0)p^{\dagger}_{\mathbf{k}_{\mathrm{I}}}(0)\rangle$ are deduced from the steady-state solutions of Eq.(5.13) and Eq.(5.14) respectively, as

$$A^{*}_{\mathrm{LP}}(\mathbf{k}_{\mathrm{S}})=\frac{E^{\mathrm{int}}_{\mathrm{LP}}(\mathbf{k}_{\mathrm{S}})P_{\mathrm{P}}^2\delta_{\mathrm{LP}}(\mathbf{k}_{\mathrm{S}})}{|\delta_{\mathrm{LP}}(\mathbf{k}_{\mathrm{S}})|^2-\frac{(\gamma_{\mathrm{LP}}(\mathbf{k}_{\mathrm{S}})+\gamma_{\mathrm{LP}}(\mathbf{k}_{\mathrm{I}}))^2}{\gamma_{\mathrm{LP}}(\mathbf{k}_{\mathrm{S}})\gamma_{\mathrm{LP}}(\mathbf{k}_{\mathrm{I}})}|E^{\mathrm{int}}_{\mathrm{LP}}(\mathbf{k}_{\mathrm{S}})P_{\mathrm{P}}^2|^2} \tag{5.17}$$

the steady-state population

$$N_{\mathrm{LP}}(\mathbf{k}_{\mathrm{S}})=\Im\left\{E^{\mathrm{int}}_{\mathrm{LP}}(\mathbf{k}_{\mathrm{S}})P_{\mathrm{P}}^2A^{*}_{\mathrm{LP}}(\mathbf{k}_{\mathrm{S}})\right\}/\gamma_{\mathrm{LP}}(\mathbf{k}_{\mathrm{S}}) \tag{5.18}$$

and the signal-idler detuning,

$$\delta_{\mathrm{LP}}(\mathbf{k}_{\mathrm{S}}) = 2E_{\mathrm{P}} - \widehat{E}^{*}_{\mathrm{LP}}(\mathbf{k}_{\mathrm{S}}) - \widehat{E}^{*}_{\mathrm{LP}}(\mathbf{k}_{\mathrm{I}}) \tag{5.19}$$

These equations are valid below the threshold for the parametric amplification which is calculated from the condition $\Im\{\widehat{E}^{-}_{\mathrm{LP}}\} = 0$ and an assumption of equal real parts of eigenenergies of polariton real branch and corresponding ghost branch what is equivalent to phase matching for signal and idler. The threshold condition is obtained as

$$E^{\mathrm{int}}_{\mathrm{LP}}|P_P|^2 = \sqrt{\gamma_{LP}(\mathbf{k}_{\mathrm{S}})\gamma_{LP}(\mathbf{k}_{\mathrm{I}})} \tag{5.20}$$

5.4 STABILITY ANALYSIS

The theoretical treatment of parametric instabilities and quantum fluid effects in microcavities was described in Ref. [92] and Ref. [35] respectively, and is summarized in Ref.[102]. Accordingly to Ref. [102], the model of anti-hermitian coupling between signal and idler polariton branches described in Sec. 5.3 is equivalent to the Bogoliubov theory[103] which treats mathematically the phenomenological model of superfluidity proposed by Landau [102], see Chap. 6. The eigenmodes of the system are calculated from the 4 x 4 coupling matrix for exciton and photon wavefunctions with coupling between signal and idler $V = g|\Psi^{ss}_{X}|^{2}$[3], compare Eq.(5.10) where polariton basis was considered. The stability analysis is discussed for different experimental parameters. In general, stability condition requires that imaginary part of the solution is negative, $\Im\{\widehat{E}^{\pm}_{\mathrm{LP}}\} < 0$. As a consequence, polaritons exhibit bistable behavior as shown by the hysteresis in Fig. 5.4(1)(e). Measurements and simulations described in this Chapter in Sec. 5.7 were done in low intensity regime within the lower branch of the hysteresis as shown in Fig. 5.4 on the left by the point 'D'. $\Im\{\widehat{E}^{\pm}_{\mathrm{LP}}\}$ and $\Re\{\widehat{E}^{\pm}_{\mathrm{LP}}\}$ of the eigenmodes are plotted in Fig. 5.4(1)(a) and Fig. 5.4(1)(b), showing that the imaginary parts of the solutions are significantly modified around the idler $\mathbf{k}_{\mathrm{I}} = 2\mathbf{k}_{\mathrm{P}}$ and signal $\mathbf{k}_{\mathrm{S}} = 0$ wavevectors, however the solutions are stable $\Im\{\widehat{E}^{\pm}_{\mathrm{LP}}\} < 0$. Unstable solutions are shown in Fig. 5.4(1)(c),(d), the parameters of this plot correspond to the point on the hysteresis shown in Fig. 5.4(1)(e) which is to the left from the threshold point 'C', it is instability of parametric or

---

[3] subscript 'ss' denotes steady-state

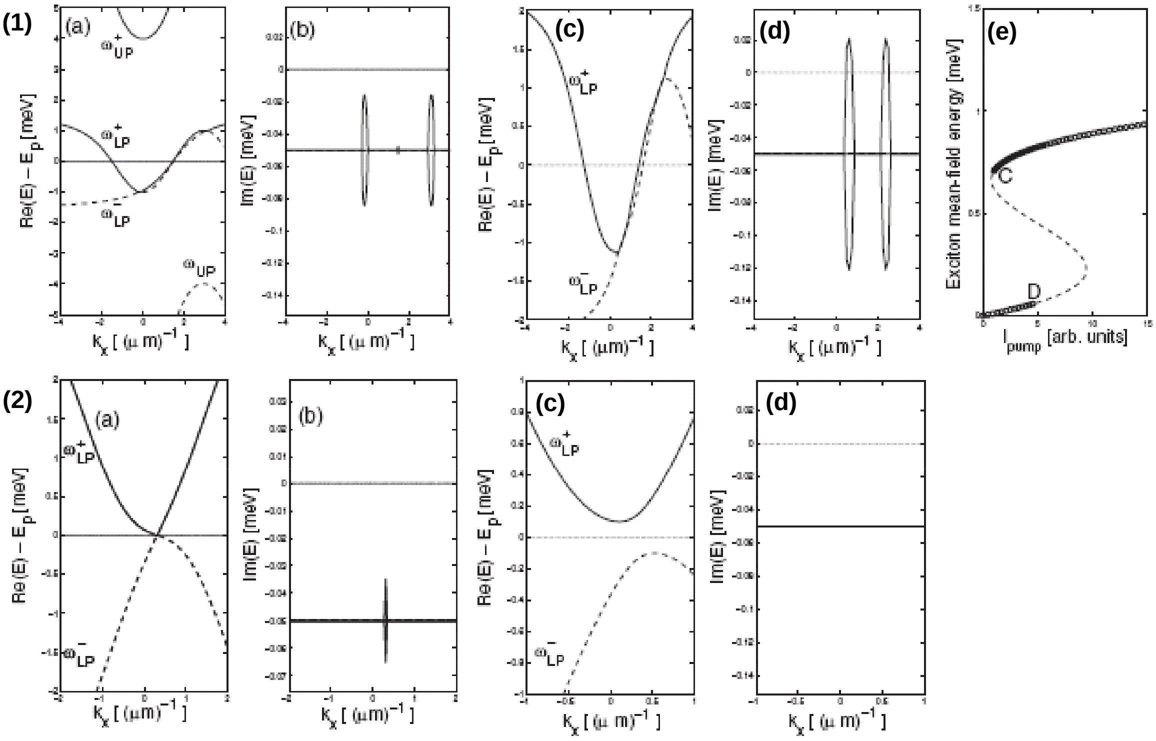

Figure 5.4: Stability analysis for the eigenvalues of coupling matrix Eq.(5.10) after Ref.[102] where $\Re\{\widehat{E}^{\pm}_{B}(\mathbf{k}_{\mathrm{S}})\}$ and $\Im\{\widehat{E}^{\pm}_{B}(\mathbf{k}_{\mathrm{S}})\}$ are plotted for different parameters, see discussion in text. In (1)(a), real part of the $\widehat{E}^{\pm}_{B}(\mathbf{k}_{\mathrm{S}})$, in (b), imaginary part of $\widehat{E}^{\pm}_{B}(\mathbf{k}_{\mathrm{S}})$ for $\mathbf{k}_{\mathrm{P}} = 1.5/\,\mu\mathrm{m}$, $\hbar\omega_P - \hbar\omega_{LP}(\mathbf{k}_{\mathrm{P}}) = 0.107$ meV, exciton mean field energy $\hbar g|\Psi^{ss}_X|^2 = 0.05$meV. In (1)(c),(d) parameters as for (1) but with $\hbar\omega_P - \hbar\omega_{LP}(\mathbf{k}_{\mathrm{P}}) = 0.47$ meV, $\hbar g|\Psi^{ss}_X|^2 = 0.699$meV. In (2)(a)(b), $\mathbf{k}_{\mathrm{P}} = 0.314/\,\mu\mathrm{m}$, $\hbar\omega_P - \hbar\omega_{LP}(\mathbf{k}_{\mathrm{P}}) = 0.47$ meV, exciton mean field energy $\hbar g|\Psi^{ss}_X|^2 = 1.02$meV. In (2)(c)(d), $\mathbf{k}_{\mathrm{P}} = 0.314/\mu$, $\hbar\omega_P - \hbar\omega_{LP}(\mathbf{k}_{\mathrm{P}}) = 0.2$ meV, exciton mean field energy $\hbar g|\Psi^{ss}_X|^2 = 0.6$meV.

multimode kind, as compared to the single mode or the Kerr instability.

In Fig. 5.4(2)(a)(b), the polariton system is close to the Kerr instability, for the $\mathbf{k}_{\mathrm{P}}$, the dispersions exhibit a linear part which is equivalent to the Bogoliubov dispersion. In Fig. 5.4(2)(c)(d), real and imaginary parts are unchanged as compared with the linear regime. For these parameters, the system is on the upper branch of the relevant bistability curve.

5.5 OPTICAL IMAGING SETUP

The measurements described in this Chapter were made with the sample held in a helium bath cryostat at a temperature of 5 K and a vapor pressure of 200 mbar, compare Sec. 2.2.1. Experiment was performed in reflection due to the significant absorption of the GaAs wafer at the quantum well energy, which is the substrate on the bottom side of the microcavity, about 500 μm thick[4]. To measure the polariton dispersion, we used a weak pulsed excitation with a mode-locked Ti:Sapphire laser delivering 100 fs pulses at 76 MHz repetition rate and a spectral width of approximately 20 meV, compare Sec. 2.2. This laser is referred hereafter as the probe laser. The excitation was focused on the sample to a diffraction limited spot of 1 μm with a 0.5NA lens having a wavevector range of $|k| \leq 4/\mu$m. In order to inject pump polaritons, we used a linearly polarized single-mode CW laser with a spectral width of 20 neV, compare Sec. 2.2. It is referred to hereafter as the pump laser. Two-dimensional excitation wavevector control was realized by imaging a collimated pump laser beam into a gimbal mirror M1 which was further imaged onto the sample [93]. The beam divergence at the mirror was adjusted to create the Gaussian waist at the sample, providing the minimum wavevector spread for a given excitation size. The beam diameter, defined here as $2\,r_D$ such that the Gaussian intensity profile on the sample $I(\pm r_D) = I_{max}/e$, was equal to 70 μm resulting in a wavevector spread of $|k| \leq 0.09/\mu$m, see discussion in Sec. 5.5.1. In order to avoid sample heating, the excitation was chopped by an acousto-optic modulator producing pulses of 1 μs pulse duration at 1% duty cycle.

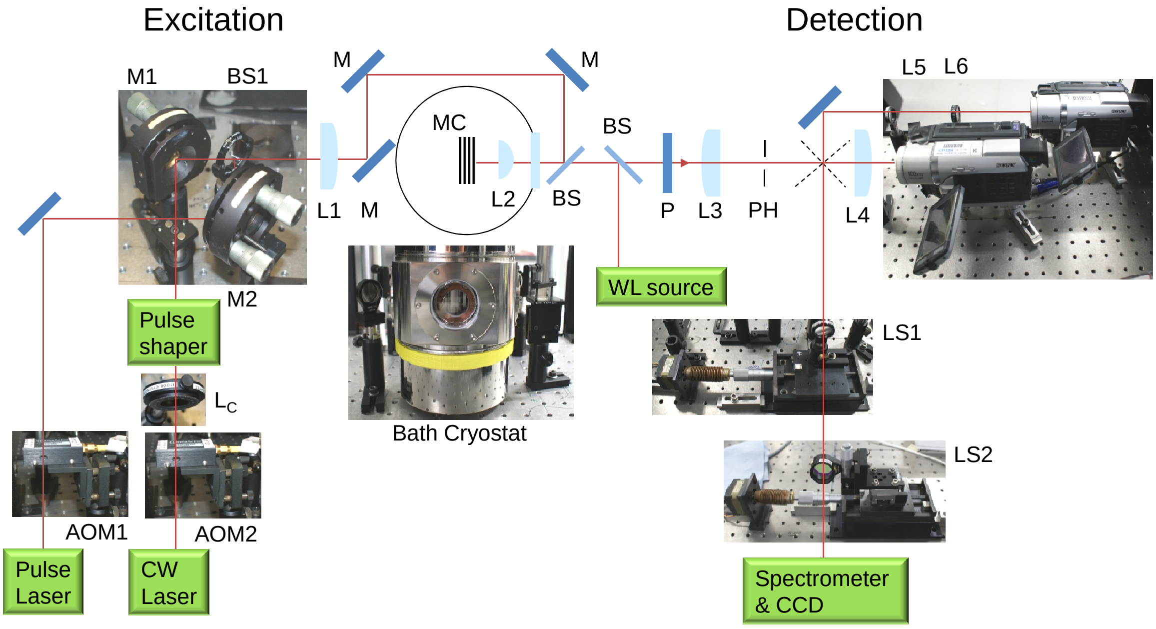

Figure 5.5: Setup used in polariton parametric scattering experiment, M-mirror, L-lens, L_c-cylindrical lens, BS-beam-splitter, P-polarizer, LS-lens on transition stage, AOM-acousto-optic modulator, MC-microcavity sample, WL-white-light source, FF-far-field plane.

---

[4] The GaAs energy gap at $T = 5K$ is $E_g = 1.5209$ eV, the quantum well heavy-hole energy is at $E_{hh} = 1.5331$ eV

5.5.1 PUMP-PROBE OPTICAL IMAGING SETUP

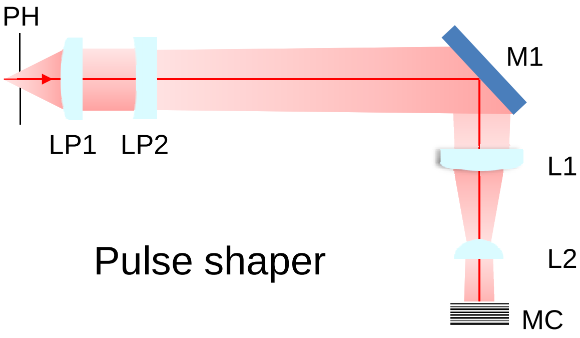

Figure 5.6: The pump laser beam shaping provides a wavevector selection on the sample by adjusting the position of the mirror M1, see text.

The setup described above was designed for the pump-probe experiment on superfluidity of microcavity polaritons, compare Appendix C, and the functionality of this setup was not fully used in the experiment on the parametric scattering of polaritons and is described below.

The pump-probe experiment on a polariton superfluid required a small spectral width of the pump laser combined with a small directional width to allow for a fine wavevector tuning and high power in order to inject resonantly polariton condensate. The probe laser, on the other hand, has to be broad in energy and wavevector in order to probe a wide range of polariton dispersion, and weaker than the pump laser so that it does not significantly change the polariton density. In order to satisfy these conditions, we performed a beam-shaping, in particular, the pump laser was focused through a 30 μm pin-hole (PH) and collimated using a lens LP1 (f=40 mm), compare Fig. 5.6. The collimated beam was projected on the gimbal mirror M1[5] which provided a wavevector adjustment. Then, the pump laser spot was demagnified by a factor of 38 by lenses L1 (f=300 mm) and L2 (f=8 mm) and projected onto the sample. The lens LP2 (f=-100 mm) with a negative focal length was introduced in order to decrease the beam waist size on the mirror M1 such that the beam size on the sample was 70 μm. The pump laser beam spot on the sample is shown in Fig. 5.7a). For the pulse laser excitation, the beam was focused to the diffraction limited spot of $\sim 1\,\mu$m. In order to decrease the probe laser power, as compared to pump beam, we used a *pellicle beam splitter* providing 8:92 reflection to transmission ratio for the 800-900 nm wavelength range[6]. The probe laser beam spot on the sample is shown in Fig. 5.7b). The nominal pump laser power was 100 mW, it was decreased in the optical path due to losses in optical elements and cryostat windows giving overall

---

[5] Gimbal mount used here provided mirror rotation along horizontal and vertical axes lying on

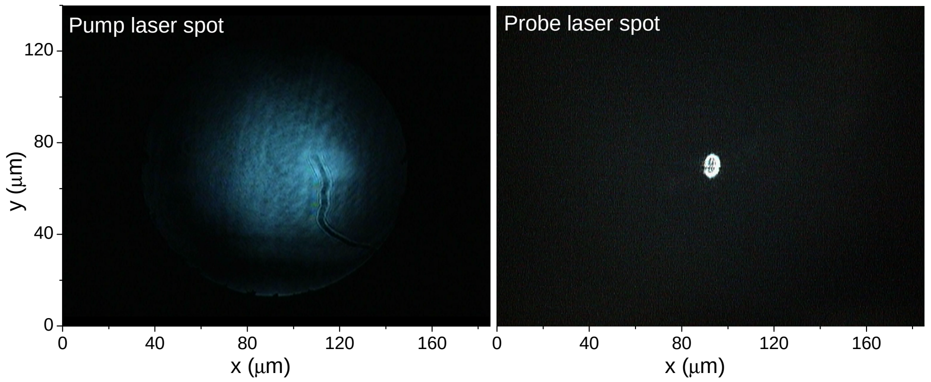

Figure 5.7: In a), the pump laser spot on the sample is $2\,r_D \sim 70\,\mu$m, b), the pulse laser spot on the sample diameter $2\,r_D \sim 6\,\mu$m, it can be focused down to diffraction limit $1\,\mu$m.

excitation power $\simeq$40 mW. Pulse laser power was $\simeq 400\,\mu$W.

The pump laser intensity on the sample was estimated as $I \sim 1 \times 10^3\,\mathrm{W/cm^2}$, from which we estimated the resonantly created polariton density as $n_\mathrm{P} = I\tau_p T/E_\mathrm{P} \simeq 3 \times 10^7/\mathrm{cm}^2$ using the polariton lifetime $\tau_p = \hbar/\gamma_\mathrm{hh} = 1.5\,\mathrm{ps}$ as deduced from $\gamma_\mathrm{hh} = 400\,\mu\mathrm{eV}$ for high power excitation, and the DBR top mirror transmission $T = 0.003$[18] calculated using $n(AlAs) = 3$, $n(Al_{0.15}Ga_{0.85}As) = 3.51$ at 810 nm[13]. Transmission through mirrors is assumed to be equal to the absorbtion inside the microcavity. We used cross-linearly polarized detection in order to suppress the surface reflected laser light. The polariton luminescence was imaged in reciprocal space onto the input slit of a high resolution (20 μeV) imaging spectrometer and recorded using a CCD-Camera [23, 41], compare Sec. 2.2.3.

5.6 Investigated microcavity sample

The microcavity sample investigated in this chapter was grown in Technical University of Denmark, Lyngby, Denmark, it was characterized in Ref [104]. It is a 1λ $\mathrm{Al_{0.05}Ga_{0.95}As}$ cavity with a single 15 nm GaAs quantum well with 5 nm $\mathrm{Al_{0.3}Ga_{0.7}As}$ barriers in its center, compare Fig. 5.8, providing two excitonic resonances, the heavy-hole and the light-hole exciton. The cavity is surrounded by $\mathrm{AlAs/Al_{0.15}Ga_{0.85}As}$ distributed Bragg reflectors with 25(16) periods on the bottom(top) of the epilayer. The cavity mode energy gradient was about 1.5 meV/mm, which allowed to adjust

---

its surface.

[6] This pellicle beam splitter is made of a 2 μm thin film of nitrocellulose and it does not introduce a significant beam displacement in the optical path, because of its thickness, extreme care have to be taken when handling it

the detuning between cavity and heavy-hole exciton $\Delta_c = E_c - E_{hh}$.

Exciton broadening mechanisms are significantly reduced in the cavity studied in this work. In particular, a single GaAs/AlGaAs quantum well exhibits small exciton inhomogeneous broadening resulting from the alloy disorder as compared to *e.g.* InGaAs/GaAs quantum wells [105], surface roughness is present [106], but due to the size of the quantum well which is comparable to the exciton Bohr radius, an exciton localization due to the well width fluctuation is reduced as compared to thinner wells [104]. Using $Al_{0.3}Ga_{0.7}As$/GaAs quantum well in a $Al_{0.05}Ga_{0.95}As$ cavity, provided a shallow confinement within the quantum well compared to the cavity layer resulting in the reduction of carrier trapping and thus of the exciton-free carrier scattering rate which contributes to the exciton homogenous broadening. This property was deduced from the reduction of the trion peak for this sample design as compared to the sample with a uniform cavity layer made of $Al_{0.3}Ga_{0.7}As$ [34]. The exciton linewidth was measured here in low-density regime as $\gamma_{hh} = 150\mu$eV at full-width half maximum using reflection spectroscopy. The exciton radiative linewidth was measured for a well of the same size using four-wave mixing as 50μeV [104].

The cavity linewidth γ_c was measured as $300\,\mu$eV. Bragg disorder [107] resulting from the lattice mismatch between $AlAs/Al_{0.15}Ga_{0.85}As$ which is equal to $\varepsilon_m \simeq 0.13\%$ at RT for this sample, measurements were made on the sample area with a low density of cross-hatches, $\rho_{MD} \simeq 10$/mm from Eq.(4.2).

5.7 POLARITON PARAMETRIC SCATTERING: MEASUREMENTS AND SIMULATIONS

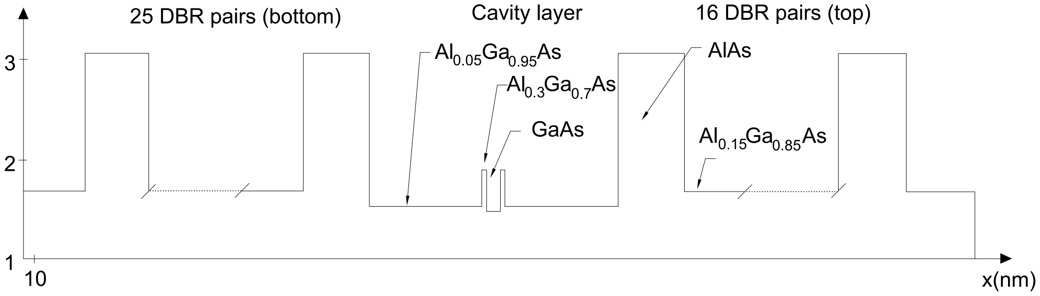

Figure 5.8: Microcavity sample studied in the experiment on parametric scattering of polaritons, direct band gap energies of the constituent heterolayers are plotted vs spatial position inside the structure.

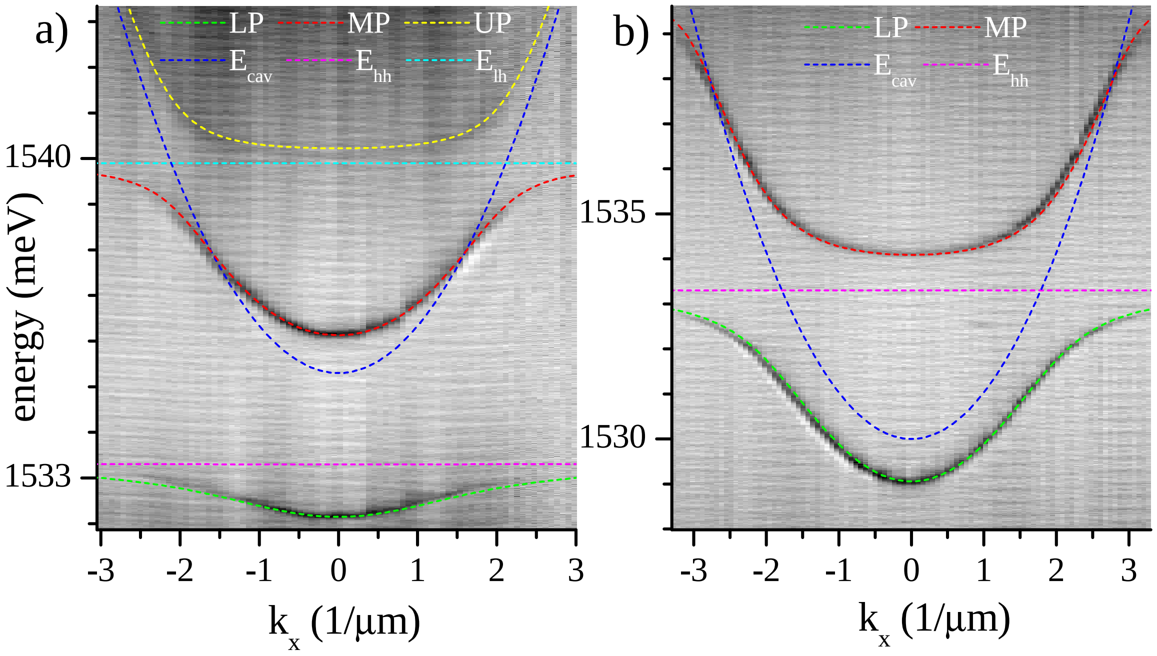

Figure 5.9: Reflection from the microcavity as function of photon energy and wavevector $\mathbf{k} = (k_x, 0)$ in a linear grey scale with minimum reflected intensity in black, maximum in white. a) positive detuning $\Delta_c = 5\,\text{meV}$, b) negative detuning $\Delta_c = -4\,\text{meV}$. The calculated polariton dispersions $E_B(\mathbf{k})$ are given by lines as labeled.

The polariton dispersion in the low-intensity regime was measured using **k** resolved reflection spectroscopy as shown in Fig. 5.9, and modeled with the coupled three oscillator model for cavity mode, heavy- and light-hole exciton [34] using

$$\begin{bmatrix} E_{hh} & 0 & \frac{\hbar\Omega_{hh}}{2} \\ 0 & E_{lh} & \frac{\hbar\Omega_{lh}}{2} \\ \frac{\hbar\Omega_{hh}}{2} & \frac{\hbar\Omega_{lh}}{2} & E_{cav} \end{bmatrix} \begin{bmatrix} X_{hh} \\ X_{lh} \\ C \end{bmatrix} = E \begin{bmatrix} X_{hh} \\ X_{lh} \\ C \end{bmatrix} \tag{5.21}$$

where E_{hh},E_{lh} and E_{cav} are the **k**-dependent heavy- and light-hole exciton and cavity mode energies, respectively. The exciton energy is taken as $E_i(\mathbf{k}) = E_i(0) + \frac{\hbar^2\mathbf{k}^2}{2M_i}$ where $i = hh, lh$, $M_{hh} = M_{lh} = 0.4m_e$[7], for cavity mode energy see Eq.(1.17). The off-diagonal coupling constants are equal to $\frac{\hbar\Omega_i}{2}$ where $\hbar\Omega_i$ is the vacuum Rabbi splitting [22]. From these fits, we deduced the exciton energies as $E_{\text{hh}} = 1.5333\,\text{eV}$, $E_{\text{lh}} = 1.5399\,\text{eV}$, and the vacuum Rabi splitting $\hbar\Omega_{\text{hh}} = 3.7\,\text{meV}$, $\hbar\Omega_{\text{lh}} = 2.4\,\text{meV}$, for heavy- and light-hole excitons, respectively. The exciton and polariton linewidths of this sample were previously compared [104] with the linewidth averaging model,

---

[7] We used $M_{hh} = M_{lh}$ as a approximation taking into account very light cavity photon mass in the order of $10^{-5}m_e$ even though for GaAs $M_{hh} = 0.4m_e, M_{lh} = 0.082m_e$ at $k = 0$

in which the polariton linewidth γ_{B}[8] is a weighted average of γ_{c} and the exciton linewidths $\gamma_{\mathrm{hh}}, \gamma_{\mathrm{lh}}$,

$$\gamma_{\mathrm{B}} = x_{\mathrm{hh,B}}\gamma_{\mathrm{hh}} + x_{\mathrm{lh,B}}\gamma_{\mathrm{lh}} + c_{\mathrm{B}}\gamma_{\mathrm{c}} \tag{5.22}$$

where $x_{\mathrm{hh=}}|X_{hh}|^2$, $x_{\mathrm{lh=}}|X_{lh}|^2$, $c = |C|^2$ are heavy-hole, light-hole exciton and cavity content of the respective branch. In the following we use the complex polariton energies, compare Eq.(5.11),

$$\widehat{E}_{\mathrm{B}} = E_B - i\gamma_{\mathrm{B}} + E_{\mathrm{B}}^{\mathrm{ren}}|P_P|^2 \tag{5.23}$$

where $E_{\mathrm{B}}^{\mathrm{ren}}(\mathbf{k})$ is simplified as

$$\begin{aligned} E_{\mathrm{B}}^{\mathrm{ren}}(\mathbf{k}) &= 2x_{\mathrm{LP}}(\mathbf{k}_{\mathrm{P}})x_{\mathrm{B}}(\mathbf{k}) \times \qquad (5.24) \\ & \left\{12E_{\mathrm{X}} + \frac{16\pi}{7}\Omega_{\mathrm{hh}}\left[\sqrt{x_{\mathrm{LP}}^{-1}(\mathbf{k}_{\mathrm{P}}) - 1} + \sqrt{x_{\mathrm{B}}^{-1}(\mathbf{k}) - 1}\right]\right\} \end{aligned}$$

after Ref. [93]. The exciton binding energy was taken as $E_{XB} = E_{XB\,hh} = 8\,\mathrm{meV}$ [104]. The model is assuming Lorenzian lineshapes, and shows good agreement [104] with the experiment for the lower polariton branch at zero and negative detuning, where the influence of the exciton inhomogeneous broadening can be neglected. Increasing the exciton density as relevant in our experiments, the exciton linewidth is dominated by exciton-exciton scattering, which has a different non-Lorentzian shape compared to inhomogeneous broadening.

The steady-state parametric emission was modeled by the author extending Eq.(5.9) and Eq.(5.10) in oder to describe parametric scattering from the lower and middle polariton idler and signal branches. The generalized coupling matrix is written as

$$M_{\mathrm{B}}^{\mathrm{par}} = \begin{pmatrix} \widehat{E}_{\mathrm{B}}(\mathbf{k}_{\mathrm{S}}) & E_{\mathrm{B}}^{\mathrm{int}}P_{\mathrm{P}}^2 \\ -(E_{\mathrm{B}}^{\mathrm{int}}P_{\mathrm{P}}^2)^* & 2E_{\mathrm{P}} - \widehat{E}_{\mathrm{B}}^*(\mathbf{k}_{\mathrm{I}}) \end{pmatrix} \tag{5.25}$$

with the eigenvalues $\widehat{E}_{\mathrm{B}}^{\pm}$.

The parametric emission intensity of each polariton branch $I_{\mathrm{B}}^{\mathrm{par}}$ is then given by

$$I_{\mathrm{B}}^{\mathrm{par}}(\mathbf{k}_{\mathrm{S}}, \omega) \propto c_{\mathrm{B}}(\mathbf{k}_{\mathrm{S}})\Im\left\{\frac{\Delta_{\mathrm{B}}(\mathbf{k}_{\mathrm{S}}, \omega)N_{\mathrm{B}}(\mathbf{k}_{\mathrm{S}}) + E_{\mathrm{B}}^{\mathrm{int}}(\mathbf{k}_{\mathrm{S}})P_{\mathrm{P}}^2A_{\mathrm{B}}^*(\mathbf{k}_{\mathrm{S}})}{\left(\widehat{E}_{\mathrm{B}}^+(\mathbf{k}_{\mathrm{S}}) - \hbar\omega\right)\left(\hbar\omega - \widehat{E}_{\mathrm{B}}^-(\mathbf{k}_{\mathrm{S}})\right)}\right\} \tag{5.26}$$

---

[8] Subscript "B" stands for a polariton branch B= $\{\mathrm{LP, MP, UP}\}$ for lower, middle and upper polariton branch while B*= $\{LP*,\ MP*,\ UP*\}$ are corresponding ghost branches

with the anomalous correlation amplitude

$$A^*_{\mathrm{B}}(\mathbf{k}_{\mathrm{S}}) = \frac{E^{\mathrm{int}}_{\mathrm{B}}(\mathbf{k}_{\mathrm{S}})P^2_{\mathrm{P}}\delta_{\mathrm{B}}(\mathbf{k}_{\mathrm{S}})}{|\delta_{\mathrm{B}}(\mathbf{k}_{\mathrm{S}})|^2 - \frac{(\gamma_{\mathrm{B}}(\mathbf{k}_{\mathrm{S}})+\gamma_{\mathrm{B}}(\mathbf{k}_{\mathrm{I}}))^2}{\gamma_{\mathrm{B}}(\mathbf{k}_{\mathrm{S}})\gamma_{\mathrm{B}}(\mathbf{k}_{\mathrm{I}})}|E^{\mathrm{int}}_{\mathrm{B}}(\mathbf{k}_{\mathrm{S}})P^2_{\mathrm{P}}|^2} \tag{5.27}$$

the steady-state population

$$N_{\mathrm{B}}(\mathbf{k}_{\mathrm{S}}) = \Im\left\{E^{\mathrm{int}}_{\mathrm{B}}(\mathbf{k}_{\mathrm{S}})P^2_{\mathrm{P}}A^*_{\mathrm{B}}(\mathbf{k}_{\mathrm{S}})\right\}/\gamma_{\mathrm{B}}(\mathbf{k}_{\mathrm{S}}) \tag{5.28}$$

the emission detuning

$$\Delta_{\mathrm{B}}(\mathbf{k}_{\mathrm{S}},\omega) = \hbar\omega + \widehat{E}^*_{\mathrm{B}}(\mathbf{k}_{\mathrm{I}}) - 2E_{\mathrm{P}} \tag{5.29}$$

and the signal-idler detuning,

$$\delta_{\mathrm{B}}(\mathbf{k}_{\mathrm{S}}) = 2E_{\mathrm{P}} - \widehat{E}^*_{\mathrm{B}}(\mathbf{k}_{\mathrm{S}}) - \widehat{E}^*_{\mathrm{B}}(\mathbf{k}_{\mathrm{I}}) \tag{5.30}$$

The total emission I^{par} is the sum of $I^{\mathrm{par}}_{\mathrm{B}}$ over all branches. We used the complex polariton energies $\widehat{E}_{\mathrm{B}}$ calculated with the three coupled oscillator model using the k-dependent broadening from Eq.(5.22) for $\gamma_{\mathrm{c}} = 300\,\mu\mathrm{eV}$,$\gamma_{\mathrm{lh}} = \gamma_{\mathrm{hh}} = 400\,\mu\mathrm{eV}$. The exciton linewidths broadening is attributed to exciton-exciton scattering due to the higher exciton density in the parametric scattering experiments [108]. The polariton-polariton interaction term $E^{\mathrm{int}}_{\mathrm{B}}$ was determined [93, 109] accounting for exciton-exciton scattering and exciton saturation as

$$\begin{aligned} E^{\mathrm{int}}_{\mathrm{B}}(\mathbf{k}_{\mathrm{S}}) \quad = \quad & x_{\mathrm{LP}}(\mathbf{k}_{\mathrm{P}})\sqrt{x_{\mathrm{B}}(\mathbf{k}_{\mathrm{S}})x_{\mathrm{B}}(\mathbf{k}_{\mathrm{I}})} \times \\ & \left\{12E_{\mathrm{X}} + \frac{16\pi}{7}\Omega_{\mathrm{hh}}\left[2\sqrt{x^{-1}_{\mathrm{LP}}(\mathbf{k}_{\mathrm{P}})-1} + \sqrt{x^{-1}_{\mathrm{B}}(\mathbf{k}_{\mathrm{S}})-1} + \sqrt{x^{-1}_{\mathrm{B}}(\mathbf{k}_{\mathrm{I}})-1}\right]\right\} \end{aligned} \tag{5.31}$$

for circularly polarized excitations. Here we used linearly polarized excitation and in simulations neglected spin interactions as discussed in Sec. 5.2. The excitonic content x in the above equations was taken as the sum $x = x_{\mathrm{hh}} + x_{\mathrm{lh}}$ of heavy and light hole content. The pump is assumed to be resonant to the lower polariton branch. Simulations were made below the critical density for polariton parametric amplification given in Eq.(5.20). Simulations were made with a resolution of $20\,\mu\mathrm{eV}$ in $\hbar\omega$ and $0.06/\,\mu\mathrm{m}$ in $\mathbf{k}_{\mathrm{S}}$.

The measured microcavity emission for different pump energies and wavevectors are discussed below together with results of simulations. We first discuss the results for

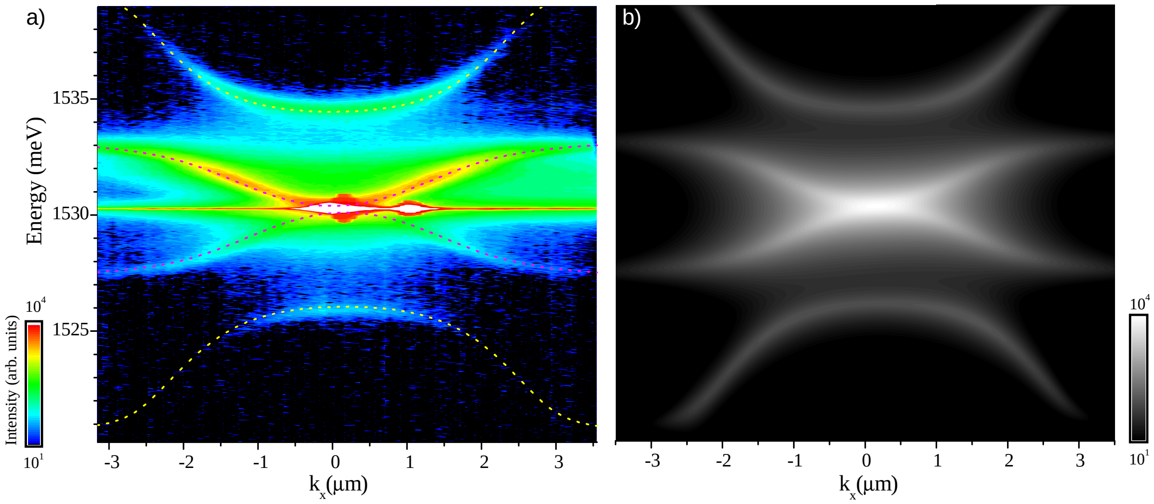

Figure 5.10: Energy and wavevector resolved emission $I(\mathbf{k},\omega)$ on a logarithmic scale as indicated, for a pump energy $E_\mathrm{P} = 1530.25\,\mathrm{meV}$ and wavevector $\mathbf{k}_\mathrm{P} = (0.1, 0)/\mu\mathrm{m}$ and a cavity detuning $\Delta_\mathrm{c} = -1.7\,\mathrm{meV}$. a) Measured $I(\mathbf{k},\omega)$ for $\mathbf{k} = (k_x, 0.4/\mu\mathrm{m})$. Lines: Eigenmodes $\widehat{E}^{\pm}_\mathrm{B}(\mathbf{k})$ of Eq.(5.25), red for lower polariton real and ghost branch, yellow for middle polariton real and ghost branch. b) Parametric emission $I^\mathrm{par}(\mathbf{k},\omega)$ calculated using Eq.(5.26). k-resolution of data $\delta k_x = 0.07/\mu\mathrm{m}$, $\delta k_y = 0.14/\mu\mathrm{m}$.

a pump close to the dispersion minimum at $E_\mathrm{P} = 1530.15\,\mathrm{meV}$ and $\mathbf{k}_\mathrm{P} = (0.1, 0)/\mu\mathrm{m}$ for a cavity detuning $\Delta_\mathrm{c} = -1.7\,\mathrm{meV}$, shown in Fig. 5.10. The measured emission $I((k_x, 0.4/\mu\mathrm{m}), \omega)$ (presented in Fig. 5.10a) shows a dominant emission from the LP and from the pump which is scattered elastically by disorder into the detection wavevector range. The emission from the MP is about 2 orders of magnitude weaker, and the ghost branches LP* and MP* are 2-4 orders of magnitude weaker and show a reversed dispersion. The predicted eigenvalues $\widehat{E}^{\pm}_\mathrm{B}(\mathbf{k})$ of Eq.(5.25) for the exact experimental conditions are following the observed emission peaks. For a more detailed comparison with theory, we show in Fig. 5.10b) the calculated parametric emission I^par. Qualitative agreement between experimental and theoretical data is found. The main difference is in the observed intensities, which in the experiment is much weaker for the ghost branches as compared to real branches. This is expected as the model accounts for radiative broadening only, such that all parametrically scattered polaritons are emitted, resulting in equal intensities of signal and idler. In the experiment, a significant part of the broadening is due to the excitons absorbtion (see Eq.(5.22)), which is a loss of polaritons not leading to emission. Eventually, this loss leads to a thermalized density of excitons in a high $\mathbf{k}$ range, emitting dominantly from the LP bottleneck region, which is the reason for the strong LP emission observed. Ghost branches are mostly visible for small pump wavevectors possibly due to the smaller

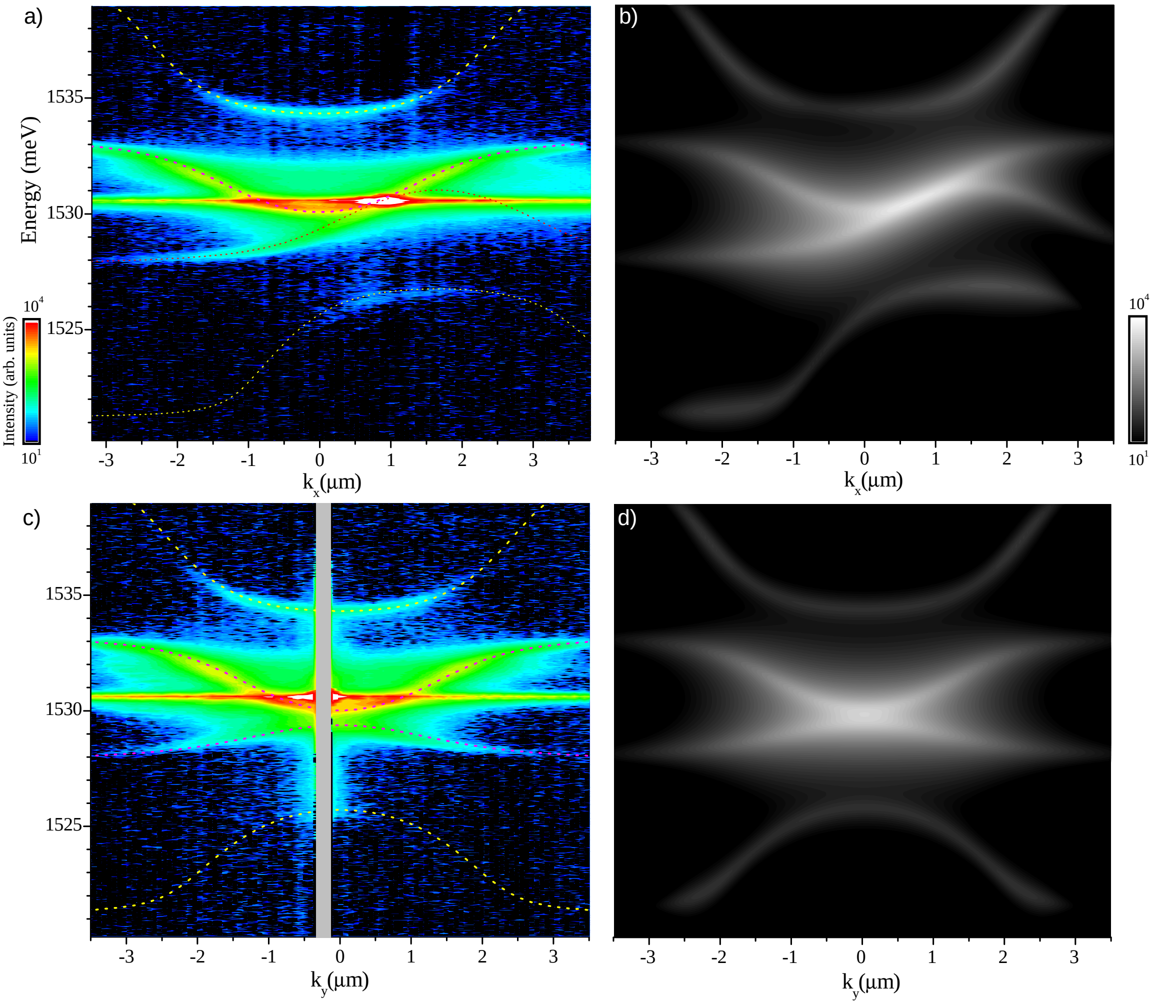

Figure 5.11: As Fig. 5.10, but for $E_\mathrm{P} = 1530.55\,\mathrm{meV}$, $\mathbf{k}_\mathrm{P} = (0.85, 0)/\mu\mathrm{m}$, $\Delta_\mathrm{c} = -2.1\,\mathrm{meV}$, and $\mathbf{k} = (kx, 0.3/\mu\mathrm{m})$. c) $\mathbf{k} = (0/\mu\mathrm{m}, ky)$. d) simulation of c).$k$ resolution of data a),b) $\delta k_x = 0.07/\mu\mathrm{m}$, $\delta k_y = 0.21/\mu\mathrm{m}$, in c),d) $\delta k_x = 0.21/\mu\mathrm{m}$, $\delta k_y = 0.07/\mu\mathrm{m}$.

exciton broadening contribution to the polariton linewidth as compared to radiative broadening for small $\mathbf{k}$ [108].

Moving to a pump away from the dispersion minimum to $\mathbf{k}_\mathrm{P} = (0.85, 0)/\mu\mathrm{m}$, the emission reveals the expected asymmetry as shown in Fig. 5.11. Two different cross-sections $\mathbf{k} = (0.3, 0)/\mu\mathrm{m}$ in Fig. 5.11a),b) and $\mathbf{k} = (0/\mu\mathrm{m}, ky)$ in Fig. 5.11c),d) of the full three-dimensional data are shown. Moving even further along the dispersion to $\mathbf{k}_\mathrm{P} = (0, -1.9)/\mu\mathrm{m}$, as shown in Fig. 5.12, corresponding to an excitation angle of 14° to the sample normal, which is close to the inflexion point for these sample parameters, LP and LP* intersect close to the dispersion minimum at $\mathbf{k}_\mathrm{P} = (0, -0.5)/\mu\mathrm{m}$ and $\mathbf{k}_\mathrm{P} = (0, 0.2)/\mu\mathrm{m}$, at which energy and momentum conserving scattering is doubly resonant, both for signal and idler. The pump wavevector for which LP and LP*

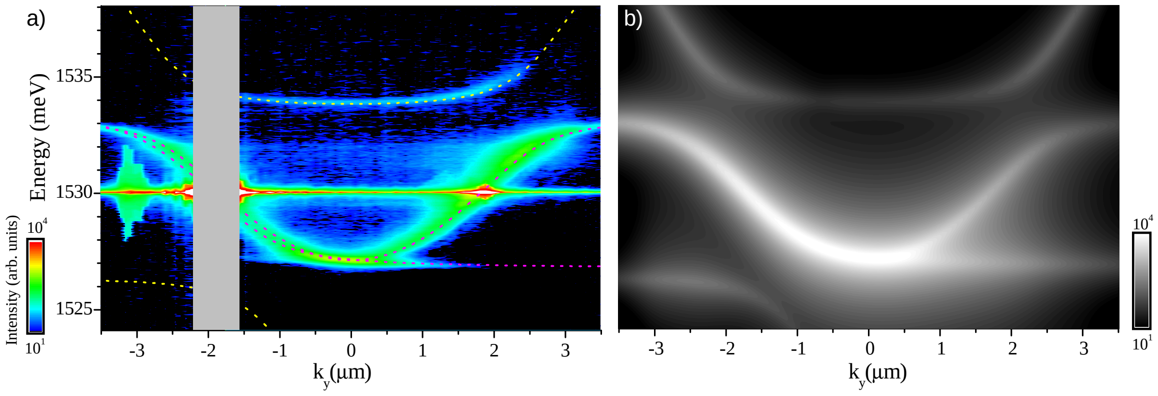

Figure 5.12: As Fig. 5.10, but for $E_\mathrm{P} = 1530.1\,\mathrm{meV}$, $\mathbf{k}_\mathrm{P} = (0, -1.9)/\mu\mathrm{m}$, $\Delta_\mathrm{c} = -5.5\,\mathrm{meV}$, and crosssection $\mathbf{k} = (0, k_y)$, k resolution of data $\delta k_x = 0.14/\mu\mathrm{m}$, $\delta k_y = 0.07/\mu\mathrm{m}$.

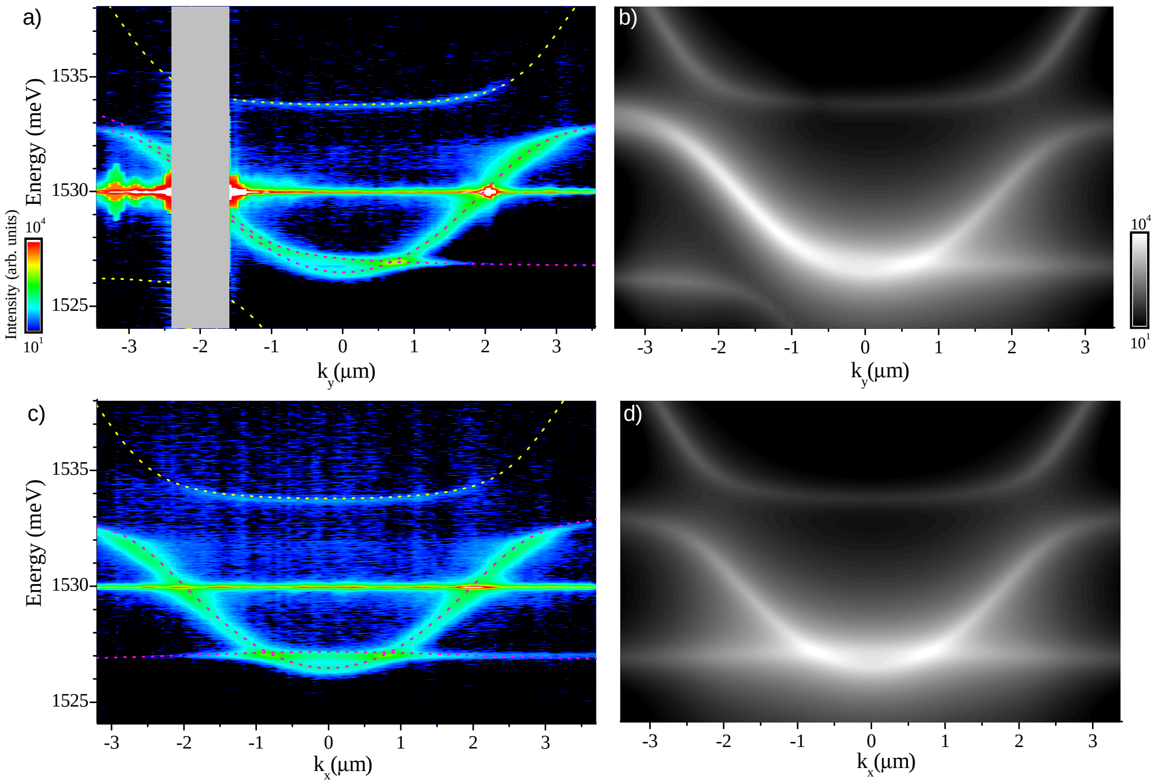

Figure 5.13: As Fig. 5.10 but for $E_\mathrm{P} = 1530.0\,\mathrm{meV}$, $\mathbf{k}_\mathrm{P} = (0, -1.95)/\mu\mathrm{m}$, $\Delta_\mathrm{c} = -6\,\mathrm{meV}$, and $\mathbf{k} = (-0.25/\mu\mathrm{m}, k_y)$ for a,b and $\mathbf{k} = (k_x, 0)$ in (c,d). k resolution of data a),b) $\delta k_x = 0.14/\mu\mathrm{m}$, $\delta k_y = 0.07/\mu\mathrm{m}$, in c),d) $\delta k_x = 0.07/\mu\mathrm{m}$, $k_y = 0.14/\mu\mathrm{m}$.

branches intersecting at $\mathbf{k} = 0$ pump angle is referred to as magic angle [90], yielding a low threshold for parametric oscillation. Parametric emission is mainly visible for the phase matched points. Simulated luminescence for this data is shown in Fig. 5.12b), it gives good agreement with the measurement.

In Fig. 5.13, we show the measured polariton luminescence for a still higher pump wavevector $\mathbf{k}_\mathrm{P} = (0, -1.95)/\mu\mathrm{m}$. Real and ghost branches intersect at $E = 1526.95\,\mathrm{meV}$, $\mathbf{k} = (-0.25, 0.7)/\mu\mathrm{m}$. In Fig. 5.13c), the cross-section $\mathbf{k} = (kx, 0)$ is shown, lower polariton real and ghost branches intersect at $E = 1527.1\,\mathrm{meV}$, $\mathbf{k} = (\pm 0.82, 0)/\mu\mathrm{m}$.

5.8 CONCLUSIONS

In summary we have shown polariton parametric pair scattering from a resonantly excited pump state into real and ghost branches of signal and idler polaritons for different excitation angles and wavevectors. The measurements are in agreement with simulations, in particular, the eigenmodes of the system are well reproduced from generalized coupling matrix Eq.(5.25). Measured and simulated intensities from real and ghost branches give qualitative agreement, apart from the additional emission from the real branch due to thermalized excitons and the missing treatment of non-radiative decay. These results can be further explored towards entangled photon source by measurements of their timecorrelation, measurements for higher pump powers which will give rise to stronger renormalisation and deviation of polariton dispersion from quadratic can be also studied.

6 POLARITON QUANTUM FLUID EFFECTS

In this section, polariton quantum fluid effects are discussed. Firstly, a brief literature overview of the subject is presented, then, the Gross-Pitaevskii equation is discussed for the spin independent and spin dependent case [110], and results of simulations are given. Further to this, a design of the samples for the purpose of polariton superfluid measurements and their characteristics are presented together with the description of the setup.

BEC of polaritons was reported in Ref. [2, 3], since then significant development in the field took place. In the experiment from Ref. [3], the investigated sample was II-VI CdTe cavity with 5nm CdTe/$Cd_{0.4}Mg_{0.6}Te$ multiple quantum wells. Exciton binding energy in II-VI materials is higher than for III-V materials, this results in higher exciton saturation densities for the earlier what allows to overcome the bottleneck effect[1] and provide efficient polariton scattering towards $E_{LP}(0)$ state. In particular, for the 5nm wide CdTe/$Cd_{0.4}Mg_{0.6}Te$ quantum well, exciton binding energy is $E_X = 26\,\mathrm{meV}$ as compared to $E_X = 9\,\mathrm{meV}$ for 6nm GaAs/$Al_{0.25}Ga_{0.75}As$ quantum well. In this experiment, polaritons were injected non-resonantly and thermalized towards the $E_{LP}(0)$ state. First and second order coherence functions were measured giving evidence of the polariton spontaneous coherence build-up above the threshold density, what is characteristic for the bosonic phase transition.

It was predicted theoretically in Ref [102], that by the analogy to atomic condensates [111], polaritons would exhibit a superfluid phase. Polariton superfluid would exhibit a linear energy dispersion and reveal the suppression of the Rayleigh scattering in the presence of photonic disorder such as point-like-defects, compare Chap. 3. Shortly after, experiments exploring quantum fluid effects of polaritons followed, in

---

[1] For negative detunings $\Delta_c < 0$, bottleneck effect results from the inefficient exciton relaxation inside the photon like part of the lower polariton dispersion, in particular, relaxation times are longer than the polariton lifetime.

particular, Utsunomiya in Ref. [112] performed experiment on polaritons propagation. Sample consisted of a AlAs cavity with GaAs/AlAs quantum wells sandwiched between AlAs/AlGaAs DBRs. In order to provide a polariton trap, a mask made of a thin metallic film was deposited onto the microcavity surface, mask consisted of a uniform layer with circular holes which acted as polariton traps. Polaritons were injected outside the trap and propagated towards the trap exhibiting, above the threshold pump power, a quasi-linear energy dispersion.

Further to this, Amo in Ref. [113] reported on the suppression of the Rayleigh scattering in a polariton fluid. In this experiment, polaritons were injected resonantly in TOPO configuration[2] using a CW pump laser and probed with a pulsed laser. It was observed that the polariton fluid propagating across natural defects [23, 107] was scattered for the pump powers below threshold, while above threshold, scattering was suppressed as was theoretically predicted [102].

Most recently, bright [114] and dark [115] solitons were demonstrated in polariton quantum fluid.

6.1 Theoretical model

6.1.1 Polarization independent case

The Gross-Pitaevskii equation is a non-linear Schrödinger equation proposed by L.Pitaevskii[3] and E.P Gross. The wavefunction $\Psi(\mathbf{r},t)$ is an order parameter of the system of interacting bosons in a trapping potential $V(r,t)$ [111].

$$i\hbar\frac{\partial\Psi(\mathbf{r},t)}{\partial t} = \left(-\frac{\hbar^2}{2m}\nabla^2 + V(\mathbf{r},t) + g|\Psi(\mathbf{r},t)|^2\right)\Psi(\mathbf{r},t) \tag{6.1}$$

This equation, originally developed to model atomic condensates [111], successfully reproduced experiments on polaritonic condensates as was experimentally and theoretically demonstrated in Ref. [112, 113] and Ref. [102, 110] respectively. In the following, we evaluated numerically a scalar Gross-Pitaevskii equation for a single condensate pumped resonantly with a circularly polarized pump laser[4], and probed with a weak probe laser. Matlab code used for these simulations was provided by Tim Liew, code was further extended and simulation performed by the author. The

---

[2] TOPO configuration satisfies $2E_{LP}(\mathbf{k}_\mathrm{P}) = E_{LP}(\mathbf{k}_\mathrm{S}) + E_{LP}(\mathbf{k}_\mathrm{I})$ with $\mathbf{k}_\mathrm{S} \neq 0$, while for OPO configuration, $\mathbf{k}_\mathrm{S} = 0$

[3] L.Pitaevskii is the former student of Nobel prize winner Lev Davidovich Landau, Landau was awarded the Nobel prize in physics for his work on theory of superfluidity

[4] Single polarization of the pump: σ_+ or σ_-.

modified Gross-Pitaevskii equation is written as

$$\left[i\hbar\frac{\partial}{\partial t} - E_{LP}(k)\right]\Psi(x,t) = \alpha_1|\Psi(x,t)|^2\Psi(x,t) + AF_P(x,t) + F_{PR}(x,t) \tag{6.2}$$

where pump P and probe PR lasers intensities have mathematical formulas

$$F_P(x,t) = F_P^0(t,x)\, e^{-i\frac{E_P t}{\hbar}}\, e^{k_P x}\, e^{-\frac{(x-x_{P0})^2}{\Delta x_P^2}} \tag{6.3}$$

$$F_{PR}(x,t) = F_{PR}^0(t,x)\, e^{-i\frac{E_{PR} t}{\hbar}}\, e^{-\frac{(t-t_{PR0})^2}{\Delta t_{PR}^2}}\, e^{-ik_{PR}x} e^{-\frac{x^2}{\Delta x_{PR}^2}} \tag{6.4}$$

The polariton dispersion $E_{LP}(k)$ is defined in k-space, such that we need to perform the Fourier transform $\mathcal{F}$ and the inverse Fourier transform $\mathcal{F}^{-1}$ in order to evaluate $\Psi(x,t)$ in real-space, namely,

$$i\hbar\frac{\partial}{\partial t}\Psi(x,t) = \mathcal{F}^{-1}\left(\, E_{LP}(k)\,\mathcal{F}(\,\Psi(x,t)\,)\,\right) + \alpha_1|\Psi(x,t)|^2\Psi(x,t) + A\cdot F_P(x,t) + F_{PR}(x,t) \tag{6.5}$$

The lower polariton dispersion is calculated as

$$E_{LP}(k) = \frac{1}{2}\left(E_X(k) + E_{cav}(k) - \sqrt{\frac{(E_X(k) - E_{cav}(k))^2}{4} + (\hbar\Omega_R)^2}\right) \tag{6.6}$$

with

$$\begin{aligned} E_{cav}(k) &= E_{cav}(0) + \frac{\hbar^2 k_{xy}^2}{2m_{cav}} - \frac{i\hbar}{2\tau_{cav}} \\ E_X &= E_X(0) + \frac{\hbar^2 k_{xy}^{*2}}{2m_X} - \frac{i\hbar}{2\tau_x} \end{aligned} \tag{6.7}$$

where E_{cav} and E_X are cavity photon and exciton energies respectively, k_{xy} is the cavity mode wavevector component in microcavity plane, k_{xy}^{*2} is the exciton wavevector component in microcavity plane. Detuning between a cavity photon and a quantum well exciton is defined as $\Delta_\mathrm{c} = E_\mathrm{c} - E_X$, we assumed here $\Delta_\mathrm{c} = 0$, $\gamma = \frac{\hbar}{2\tau}$ is a radiative linewidth, where the exciton lifetime $\tau_X = 100\,\mathrm{ps}$ and the cavity photon lifetime $\tau_{cav} = 1\,\mathrm{ps}$ were used. The Rabi splitting is $\Omega_R = 5\,\mathrm{meV}$, the cavity mass $m_{cav} = 10^{-5}\, m_e$, the exciton mass was assumed $m_X \rightarrow\propto$ resulting in $E_X = const.$ The polariton density for 1-dimensional calculations is $|\Psi(x)|^2$ in units of $\frac{1}{\mu\mathrm{m}}$ while the driving fields F_P,F_{PR} are in units of $\frac{meV}{\sqrt{\mu\mathrm{m}}}$.

Interaction parameter is $\alpha_1 = 6x^2 E_{XB} a_{XB}^2$ where x is the exciton content of polariton, E_{XB} is the exciton binding energy, a_{XB} is the exciton Bohr radius, in calculations

$\alpha_1 = 2.4\,\mathrm{meV}\mu\mathrm{m}^2$ was assumed after Ref. [110]. Pump laser is switched on gradually in time, it is implemented in the program using the Gaussian profile defined as [116]

$$A = \begin{cases} e^{\frac{-(t-t_{P0})^2}{\Delta t_P^2}} & \text{for } t < t_{P0} \\ 1 & \text{for } t > t_{P0} \end{cases}$$

where $t_{P0} = 0.05\,\mathrm{ps}$, $\Delta t_P = 0.2\,\mathrm{ps}$. Polaritons are injected non-resonantly at the pump energy $E_P = E_{LP}(k_P) + \delta E$ where the pump and the lower polariton branch energy detuning is δE. The pump spot diameter on the sample was $\Delta x_P = 200\,\mu\mathrm{m}$. In the program, after 15 ps when a quasi-equilibrium was obtained, the probe signal F_{PR} was introduced. Quasi-equilibrium is defined here as a state for which the total number of polaritons inside microcavity is constant, what effectively means that radiative losses are compensated by the pump. The probe parameters are as follows, amplitude $F_{PR}^0 = 10^{-4}\,F_P^0$, energy $E_{PR} = E_P$, $t_{PR0} = 15\,\mathrm{ps}$, time $\Delta t_{PR} = 1\,\mathrm{ps}$, wavevector $k_{PR} = k_P$, spot size $\Delta x_{PR} = 1\,\mu\mathrm{m}$

6.1.1.1 Results

In order to solve the differential equation Eq.(6.2), we implemented numerical algorithms using multistep methods, namely Runge-Kutta-Fehlberg (RKF) and Adams-Bashforth-Moulton (ABM) [116, 117]. These methods are more stable and precise as compared to single step methods such as the Range-Kutta algorithm [118]. The Runge-Kutta-Fehlberg method was implemented in order to evaluate wavefunction in the first four time-points, then, Adams-Bashforth-Moulton method was used in order to evaluate wavefunction at the later times. ABM is corrector-predictor method based on the fundamental theorem of calculus $y(t_{k+1}) = y(t_k) + \int\limits_{t_k}^{t_{k+1}} f(t, y(t))dt$. Predictor uses the Lagrange polynomial approximation for $f(t, y(t))$ based on points (t_{k+j}, f_{k+j}) with $j = -3, -2, -1, 0$, the predictor is defined as

$$p_{k+1} = y_k + h/24(-9f_{k-3} + 37f_{k-2} - 59f_{k-1} + 55f_k) \tag{6.8}$$

Corrector uses a second Lagrange polynomial based on new points (t_{k+j}, f_{k+j}) where $j = -2, -1, 0, 1$, corrector is defined as

$$y_{k+1} = y_k + h/24(f_{k-2} - 5f_{k-1} + 19f_k + 9f_{k+1}) \tag{6.9}$$

where $(t_{k+1}, f_{k+1}) = (t_{k+1}, f(t_{k+1}, p_{k+1}))$, t is time.

In calculations we evaluated $f = \frac{\partial}{\partial t}\Psi(x,t)$ from Eq.(6.5) twice, with and without probe laser, and subtracted one from the other in order to obtain the response of polariton system to the probe laser.

In Matlab, RKF and ABM algorithms are available as built-in functions called ODE (from ordinary differential equations)45 and ODE123 respectively. However, these algorithms were defined explicitly in the program in order to obtain a better error control.

In order to convert spatio-temporal data into frequency and wavevector domains we applied Fast Fourier Transform algorithm by using built-in Matlab functions *fft* and *ifft* for forward and inverse Fourier transform, respectively.

Simulation were made on a spatial grid of 1024 points covering 400 μm range, and temporal grid of 2000 points covering 20 ps range for the propagation simulations, and temporal gird of 100 000 points with 100 ps range for the bistability simulations. In order to increase the computational efficiency, Condor manager of the Cardiff University pool was accessed. Condor uses open access workstation inside Cardiff University network to run jobs in parallel on many workstation at the time. The Condor pool consists of 1000 workstation with 2.8 GHz processors connected to the network at speed of 10 Mbps [119].

In Fig. 6.1, we have plotted the solution of Eq.(6.2) substracting from the solution of the same equation but without the probe laser for different pump powers. The wavefunction $|\Psi|^2(k, E)$ is plotted in Fourier domain in a linear grey scale. Simulations were made for parameters $k_P = 0$, $\delta E = 1$meV. Each plot from Fig. 6.1 corresponds to a different pump intensity, starting from the pump intensity below threshold in Fig. 6.1a) where scattering from the pump state at $k_P = 0$ towards states $E_{LP}(\pm k) = E_P$ is observed. When the pump intensity is increased, blue-shift of the polariton dispersion is observed in Fig. 6.1b)-g). Finally, at Fig. 6.1h)-j), linear dispersion characteristic for Bogoliubov branches with further renormalisation is observed.

In Fig. 6.2, corresponding real space images of propagating polariton wavepacket are shown for different pump intensities. In Fig. 6.2a)-c), propagation of two wavepackets with wavevectors $\pm k$ and their interference in real space is observed. On the other hand, in Fig. 6.2d,e), the propagation of a single wavepacket with wavevector $|k| < 0.4/\mu$m is shown. Further to this, in Fig. 6.2f), polariton superfluid propagation is shown.

We also investigated polariton density as a function of pump intensity, shown in Fig. 6.3. Pump was switched on at $t = 0$ ps, starting from $t = 15$ ps, pump amplitude was linearly ramped from $F_{P0}(t, x) = 1$ to 16, and back to $F_{P0}(t, x) = 1$, pump profile is shown in the inset to Fig. 6.3. Remaining parameters used in simulations were as

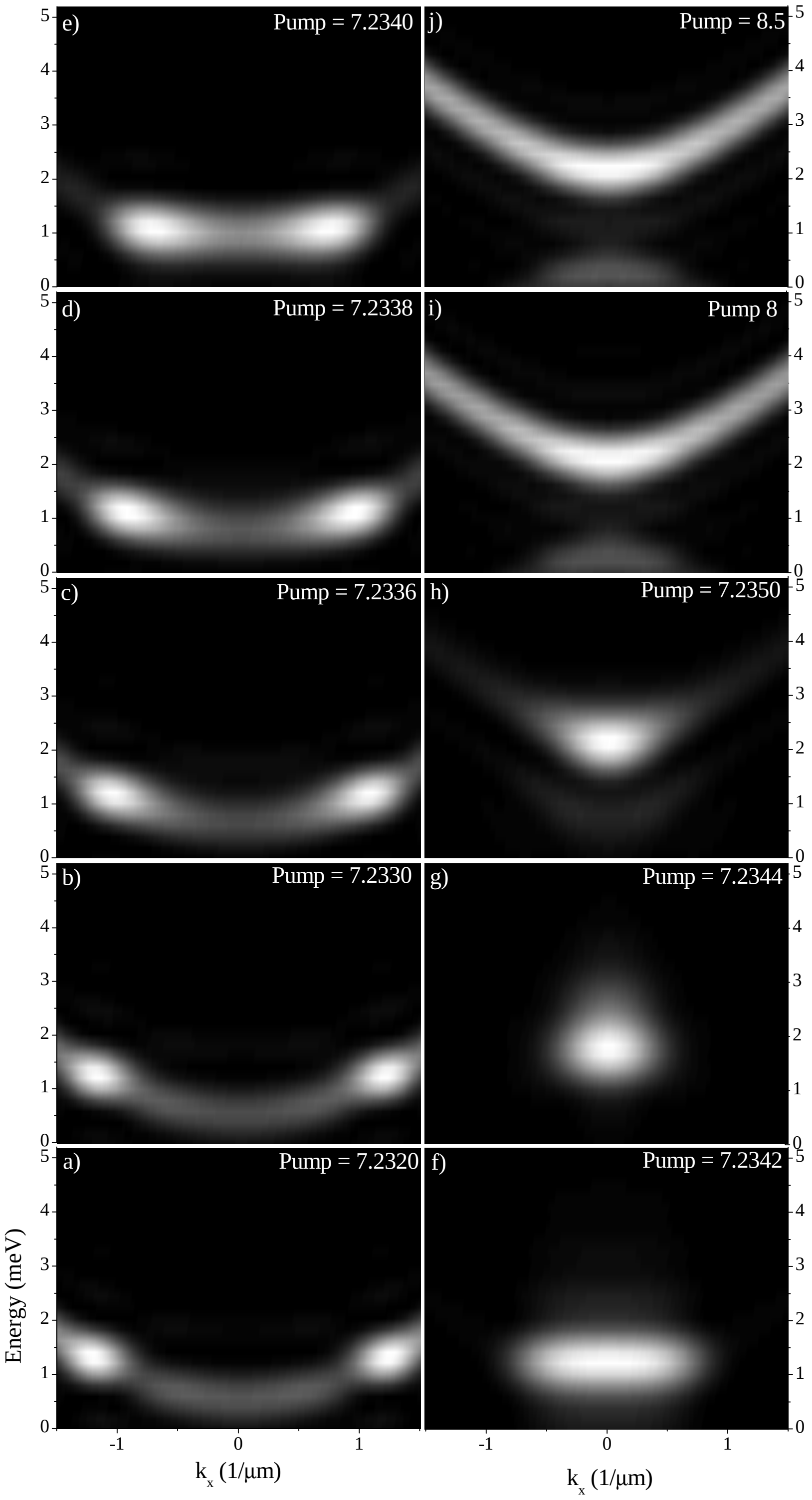

Figure 6.1: $|\Psi(k,\omega)|^2$ calculated using Eq.(6.5) on a linear grey scale, the energy is scale is relative to the $E_{LP}(0)$ energy.

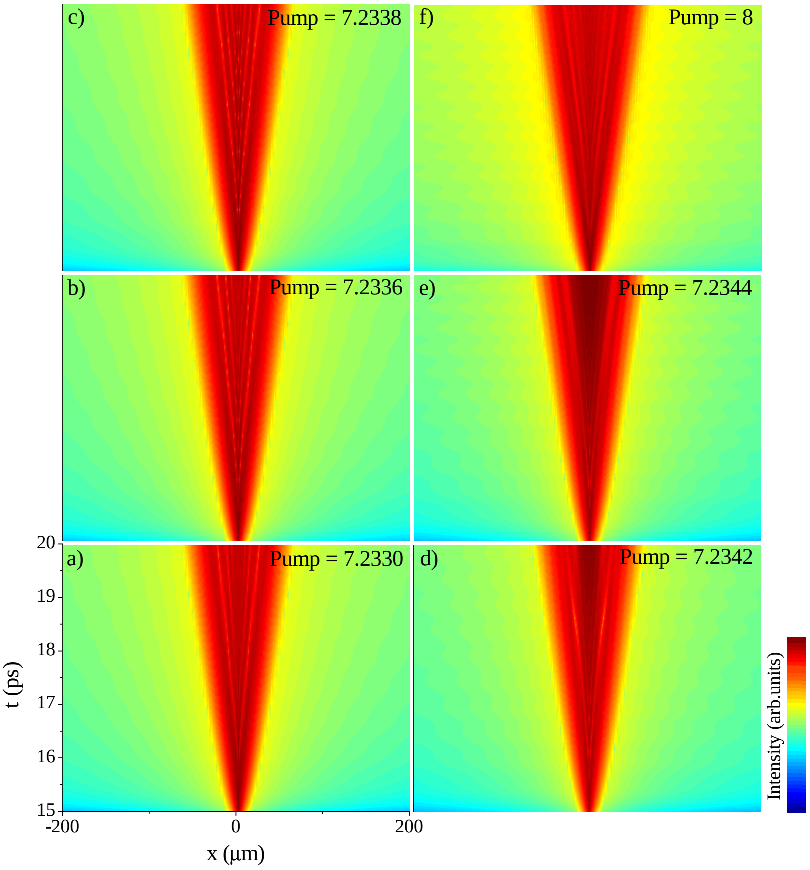

Figure 6.2: $|\Psi(x,t)|^2$ calculated using Eq.(6.5) on a logarithmic color scale for a corresponding $|\Psi(k,\omega)|^2$ plots from Fig. 6.1

.

for simulations described in Fig. 6.1 and Fig. 6.2. Maximum spatial density $n = |\Psi(x)|^2$ was calculated for each pump power, the results are plotted in Fig. 6.3 showing a hysteresis and thus the bistability of the polariton density.

To summarize, the simulations described above provide us with a practical tool to model experiments on polariton superfluidity, what was the primarily goal of this project. The Matlab code could be further extended to provide 2-dimensional simulations in real and k-space, polarization dependent interaction could also be introduced as will be discussed in the following section. Program is attached in Appendix B.

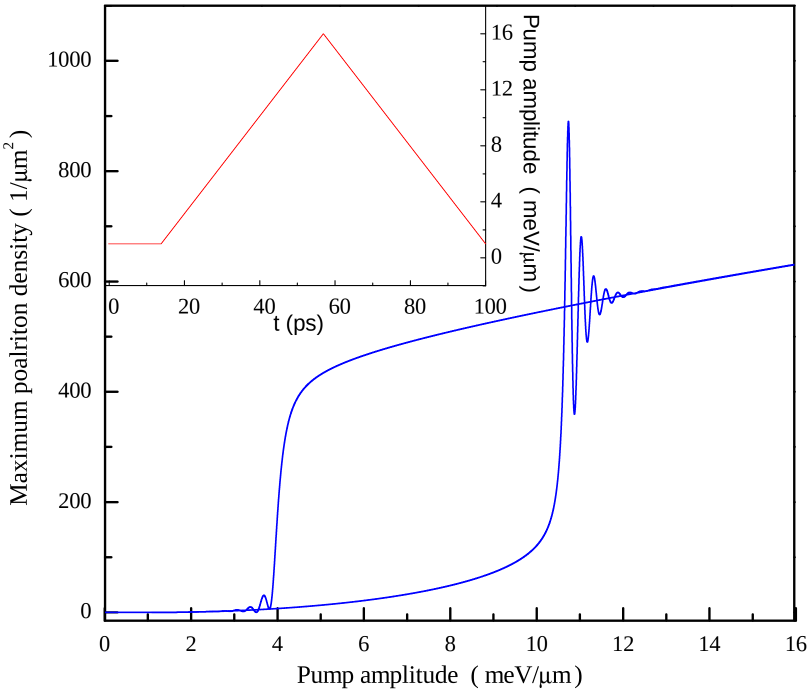

Figure 6.3: Spatial maximum density of polaritons as a function of time dependent pump amplitude was investigated. Time profile of the pump is shown in the inset.

6.1.2 POLARIZATION DEPENDENT CASE

In order to include spin dependent interaction between polaritons in singlet and triplet configuration[5] [25], the spinor Gross-Pitaevskii equation was considered [110] where two Gross-Pitaevskii equations Eq.(6.5) are coupled by the spin dependent interaction term. In Ref. [110], polaritons were injected resonantly by the pump laser which was in general linearly polarized to populate both, σ_+,σ_-, polariton condensates, and then the spin dependent interactions were investigated. Decay of polaritons was introduced by finite lifetimes of exciton and cavity photons as described in Sec. 6.1.1. Gross-Pitaevskii spinor equation written in polariton basis taking into account only lower polariton branch is written as

$$\left[i\hbar\frac{\partial}{\partial t} - E_{LP}(k)\right]\Psi^j(x,t) = \left[\alpha_1|\Psi^j(x,t)|^2 + \alpha_2|\Psi^{\bar{j}}(x,t)|^2\right]\Psi^j(x,t) + F_j e^{-i\omega_0 t} \tag{6.10}$$

where j, $\bar{j}$ denotes co- and cross-circular polarization. α_1,α_2 are interaction terms for co- and cross-polarized polaritons, usually $\alpha_1 \gg \alpha_2$ [110], remaining parameters are defined as for Eq.(6.2). Analytical formulas for the dispersion of four polariton

---

[5] Singlet spin state is when two fermions have opposite spins and total spin is 0, triplet spin state is when particles have parallel spins and total spin is 1.

branches, two for each circular polarization, were derived in Ref. [110] for circularly and linearly polarized pump. It was found that the polarization of the pump and the polariton system coincide only for circularly polarized pump, while for linearly polarized pump, polarization mixing takes place. Due to spin dependent scattering, the dispersion of interacting polaritons exhibit peculiar shapes, e.g. flattening of dispersion for small wavevectors $k \sim 0$ was predicted, what agree with experiment [120]. Theoretically predicted multistability of polariton system is a consequence of the spin nature of polaritons, it reduces to bistability when spin is not considered as shown in Sec. 6.1.1.1.

6.2 Strain compensated microcavity samples

Samples designed and grown for the purpose of experiments on the polariton quantum fluid effects are characterized in Appendix C.

6.3 Setup

Setup developed in order to study superfluidity of microcavity polaritons is described in Sec. 5.5.1.

6.4 Conclusions

We have theoretically modeled polariton quantum fluid effect, these model can be used in the future. Design of the microcavity samples, successive growths and characterization of 20 wafers grown in National III-V Centre in Sheffield UK, provided us with reproducible growth receipts which can be used in the future in order to obtain samples with long photon lifetimes and low exciton and photon disorder.

7 CONCLUSIONS

In this work, we have identified origins behind the formation of disorder in microcavity samples and propose and demonstrated methods to eliminate it. In particular, we identified the cross-hatch dislocation pattern as a cause of polariton scattering and localization, and have proposed and demonstrated the suppression of the cross-hatch disorder in GaAs/AlAs microcavities by strain compensation, which was realized by incorporating thin AlP layers into the AlAs layers of the DBRs. Using an AlP layer thickness of 1.1 nm, corresponding to an effective $\mathrm{AlAs}_{0.985}\mathrm{P}_{0.015}$ alloy of the low-index layer, a reduction of the cross-hatch density by an order of magnitude is achieved.
Furthermore, we have identified point-like oval or round defects in MBE grown GaAs microcavities which create zero-dimensional polariton states of narrow linewidths. We have revealed their three-dimensional structure and their formation mechanism, an impinging Ga droplet during growth, we have deduced effective confinement potentials for the defects, and suggested methods to eliminate them.
Moreover, in low-disordered samples, we have shown polariton parametric pair scattering from a resonantly excited pump state into real and ghost branches of signal and idler polaritons for different excitation angles and wavevectors. We also simulated experimental data using Heisenberg equation of motion for coupled polariton populations. These measurements are in agreement with simulations, apart from the additional emission from real branch originating from thermalized excitons which are not currently included in the model. These results can be further explored towards entangled photon source by measurements of their time-correlation.
Finally, we presented results of theoretical simulations on polariton quantum fluid effects. We also presented extensive discussion on samples design and characterization, when strain-compensated strongly coupled samples with long photon lifetime will be grown, the many-body physics and quantum phase transitions in these systems is going to be studied.

APPENDIX A DUAL LENS HOLDER

Discussion on the design of the dual lens holder and its functionalities see Sec. 2.2.2.2.

Drawn by: Joanna Zajac at 10/05/28
Part P1 scale 1:1
Quantity: 1
Material:Stainless steel

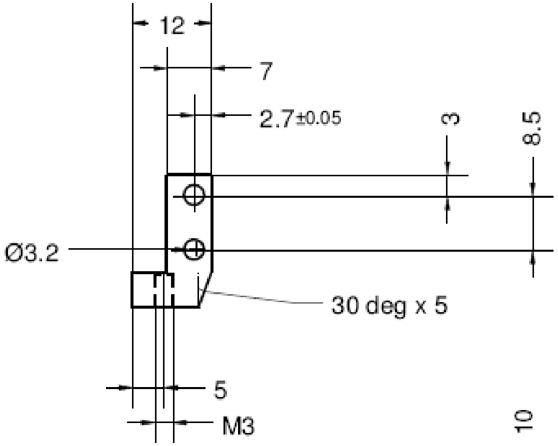

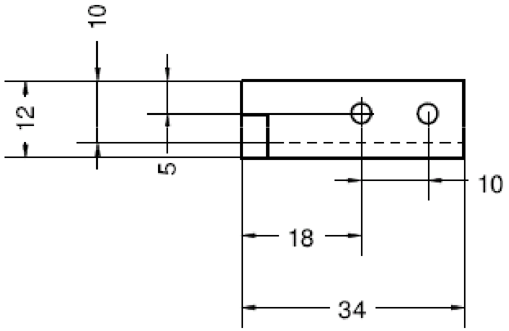

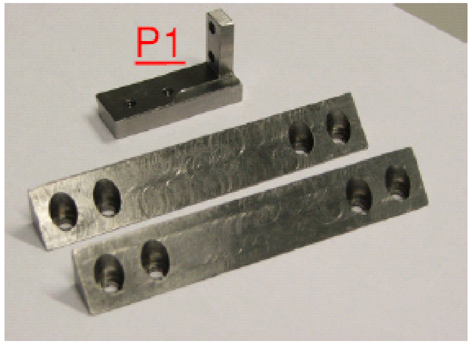

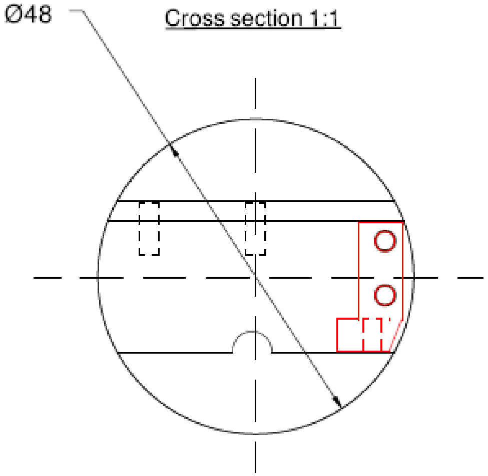

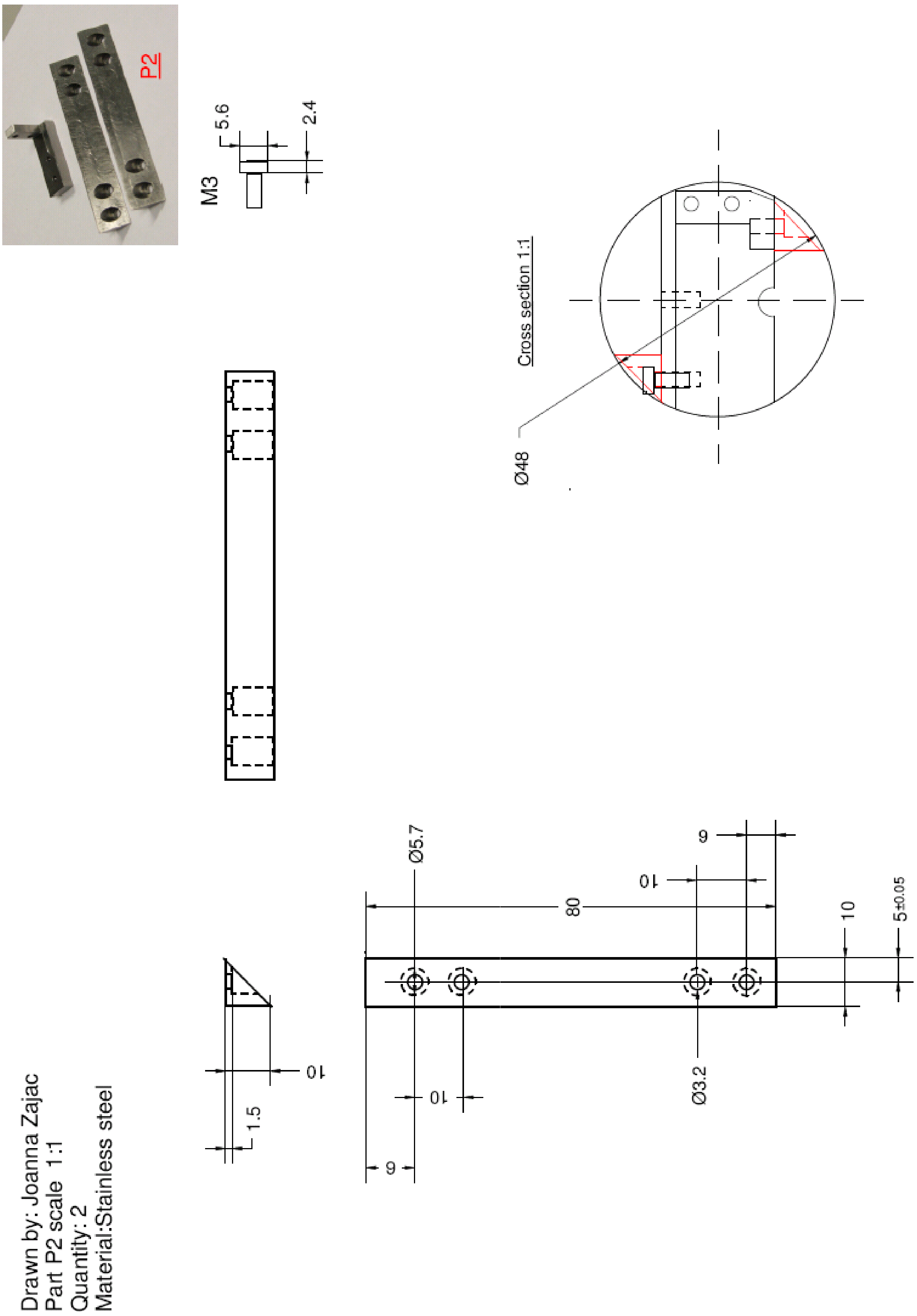

Drawn by: Joanna Zajac
Part P2 scale 1:1
Quantity: 2
Material:Stainless steel

Drawn by: Joanna Zajac at 10/05/28
Part P3 scale 1:1
Quantity: 2
Material:Stainless steel

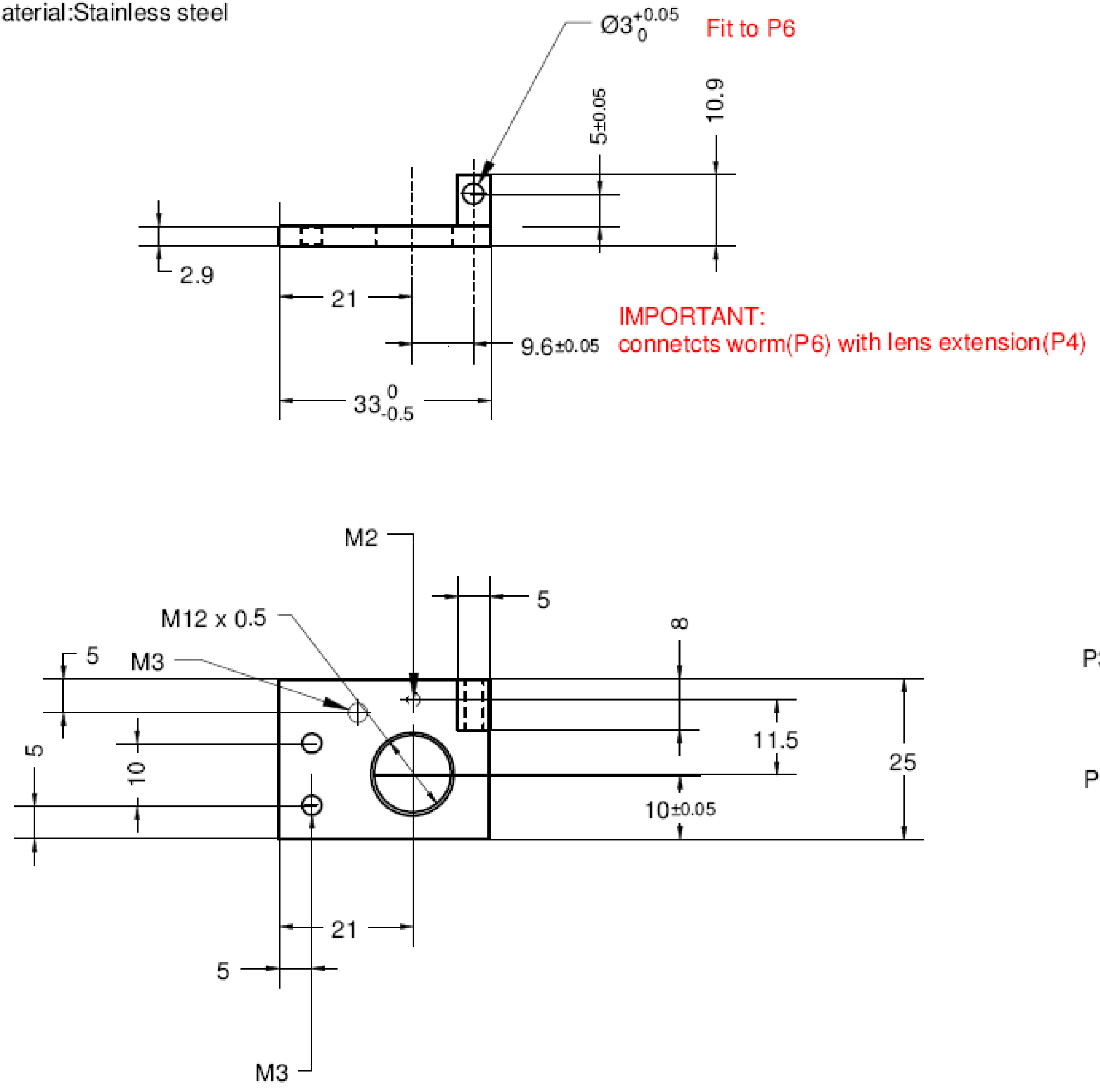

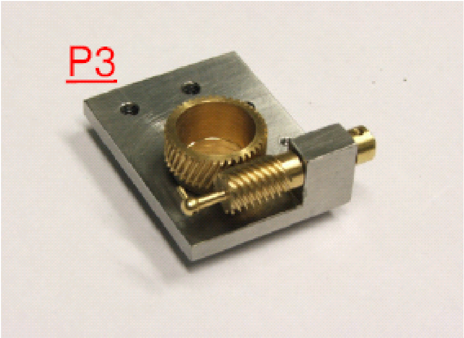

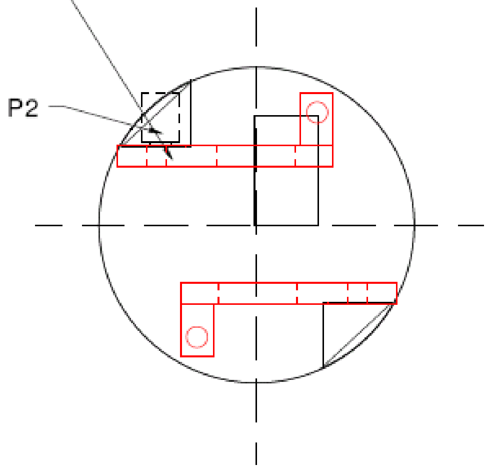
Cross section scale 1:1

Drawn by: Joanna Zajac at 10/05/28
Part P4, scale 2 : 1,
Quantity: 2
Material: Brass

m=0.3 (axial pitch of worm),
p = 0.94 (normal pitch of worm)
z = 42 (nr of teeth)
do = 12.6 (wheel diamteter)

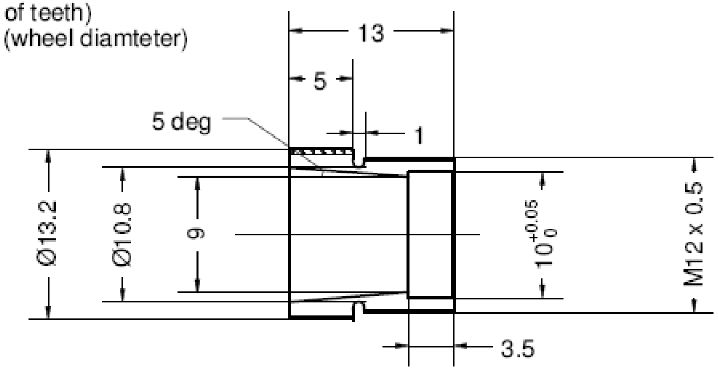

Part P4b, scale 1: 1,
Quantity: 2
Material: Aluminium

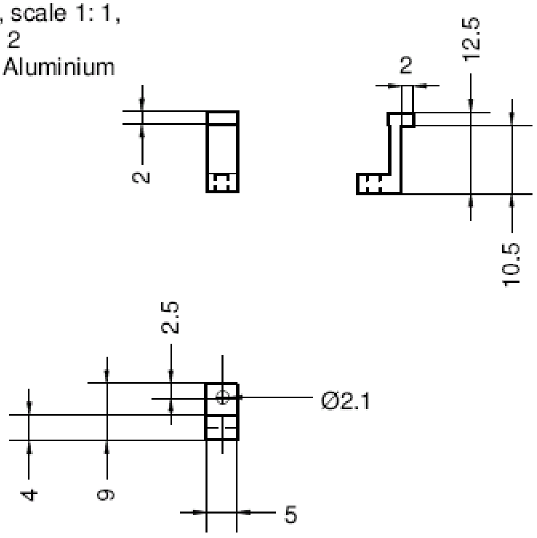

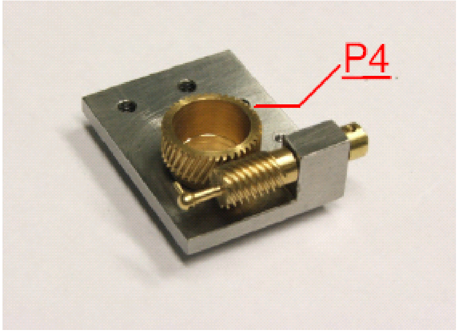

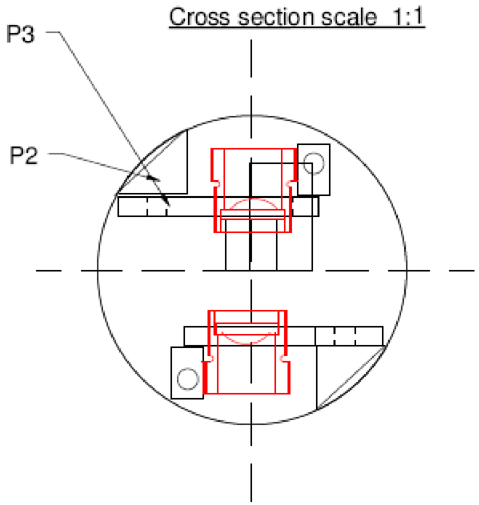

Drawn by: Joanna Zajac at 10/05/28
Part P5a scale 2 : 1
Quantity: 2
Material:Brass

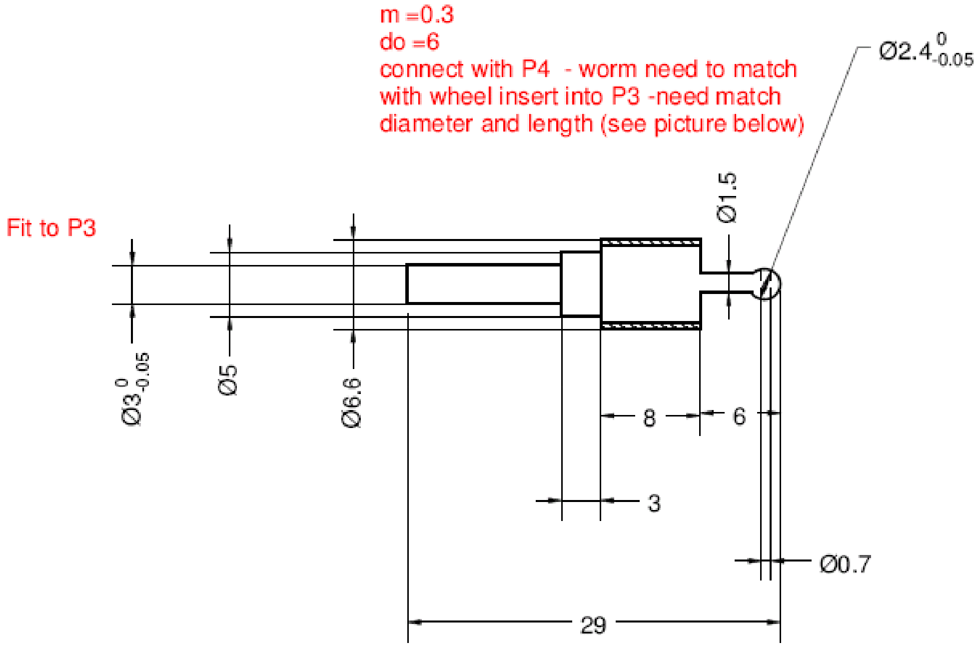
m =0.3
do =6
connect with P4 - worm need to match
with wheel insert into P3 -need match
diameter and length (see picture below)

Fit to P3

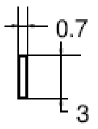

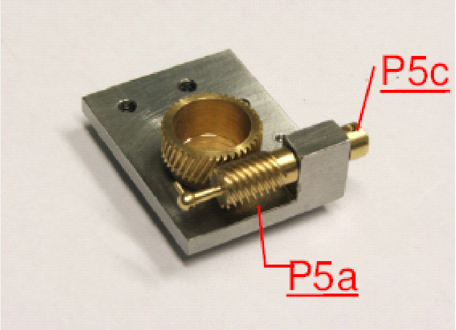

Part P5b scale 1 : 1
Quantity: 2
Material:
tube

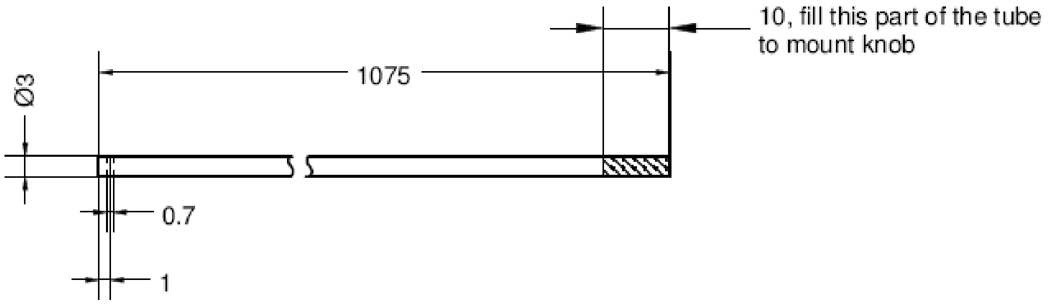

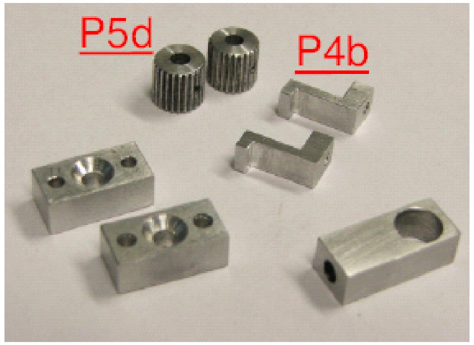

Part P5c scale 1 : 1
Quantity: 2
Material:Brass

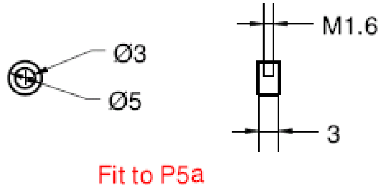

Part P5d scale 1 : 1
Quantity: 2
Material:Aluminium
knob

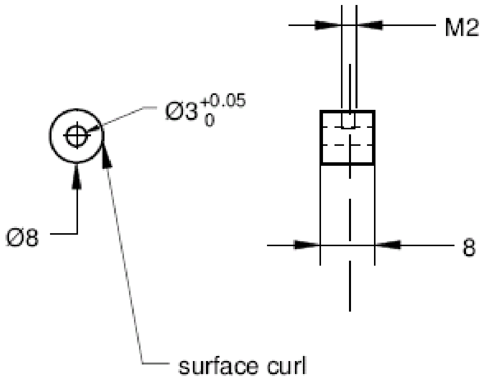

Drawn by: Joanna Zajac at 10/05/28
Part P6, scale 1:1
Quantity: 1
Material:Aluminium (modifications only!)

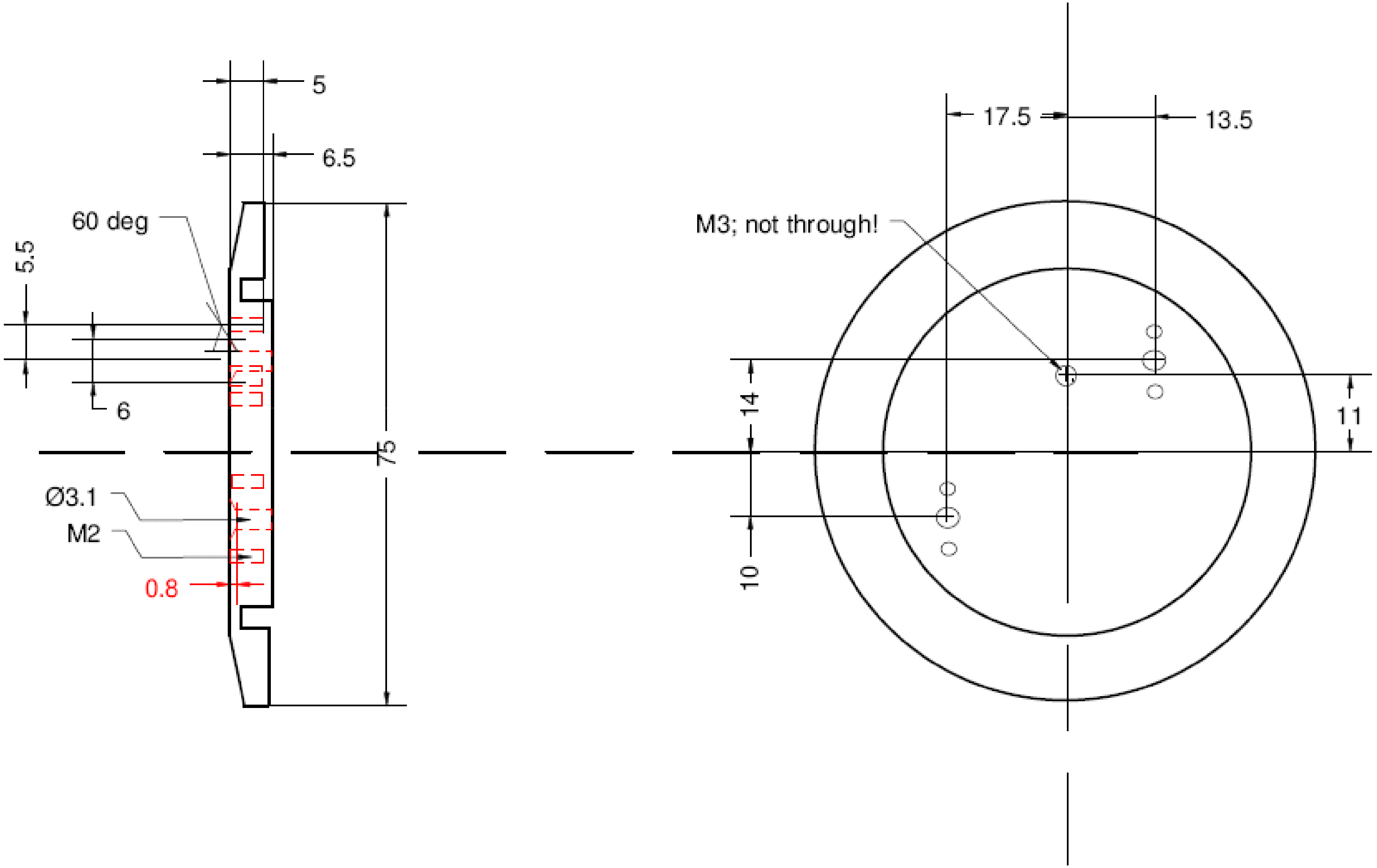

Drawn by: Joanna Zajac at 10/05/28
Part P7a, scale 1:1
Quantity: 2
Material:Aluminium

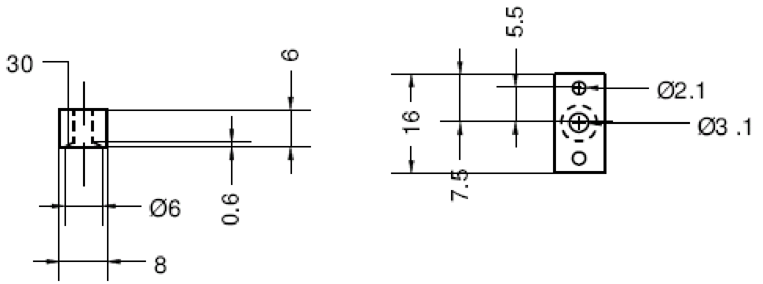

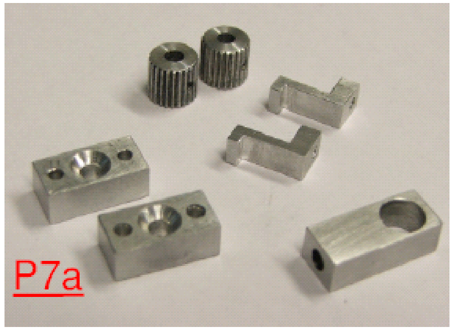

Part P7b, scale 1:1,
modify part e2b.836.11.00.2-27
modyfications on one side only(in red);

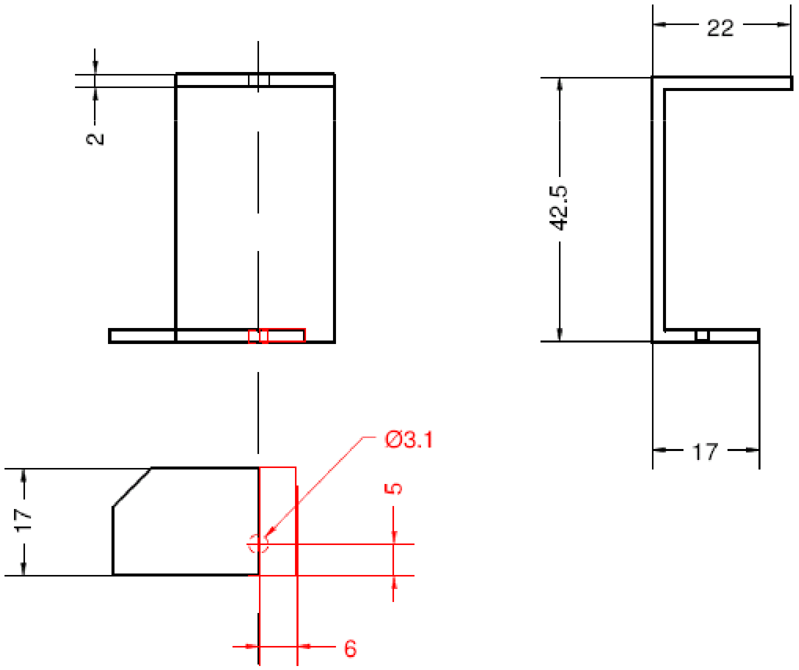

Part P8, scale 1:1,
Quantity: 1
Material:Aluminium

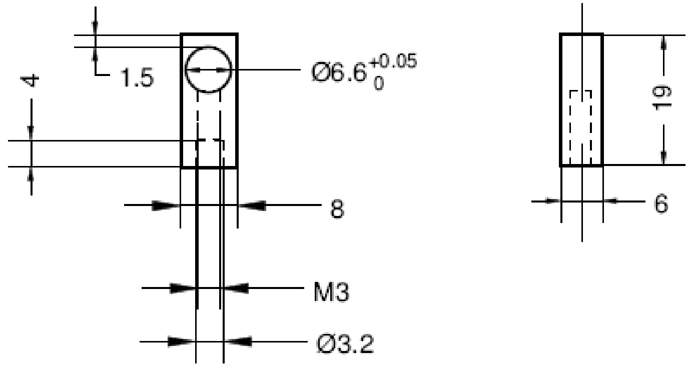

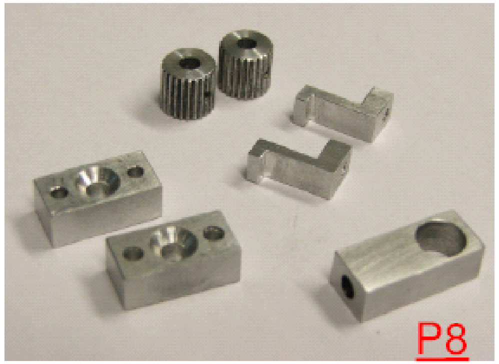

APPENDIX B GROSS-PITAEVSKII SIMULATIONS

Discussion on the numerical simulation of Gross-Pitaievskii equation see Sec. 6.1.1.1. Below the Matlab code solving a 1-dimensional equation is attached.

```
%     /////////////////////////////////////////////////////////////////////////
%     Author: Joanna Zajac, 090106. Modified 15/08/12
%     All rights (and lefts) reserved.
%     Description: Program written to model polariton density dependency on
%     a pump intensity using Gross-Pitaevskii equation
%     /////////////////////////////////////////////////////////////////////////


function load_const_v3(Pump_amplitude)
    dt = datestr(now, 'yyyymmddTHHMMSS');
    global Pump_amplitude;
    Pump_amplitude = 9;

    c=3*1e8*1e6*1e-12;                %units: um,ps,meV
    me=0.511*1e9/c^2;
    hbar = 6.582*1e-16*1e3*1e12;

    %gird
    Nx = 1024;
    x = zeros(Nx,1);
    k_max = 4; k_min = -k_max;
    x_max = 2*pi*Nx/(k_max); x_min = -x_max;
    step_x = (x_max - x_min)/Nx;
    x = x_min+step_x:step_x:x_max;
    step_k = (k_max-k_min)/Nx;
    k_x = k_min:step_k:k_max-step_k;

    step_t = 0.01;
    t_max = 20; t_min = 0;
    Nt = (t_max - t_min)/(step_t);
    tt = zeros(1,Nt);
    tt = t_min+step_t:step_t:t_max;
    nt = -Nt/2+1:Nt/2;
    Et = (nt*2*pi)./(t_max)*hbar;

    %pump
    Pump_to = 0.05;
    Pump_tL = 0.2;
    Pump_xL =200;
    %pulse
    Pulse_xL = 1;
    Pulse_to = 15;
    Pulse_tL = 0.1   ;
    Pulse_amplitude = 1e-3;
    alfa1 = 2.4*1e-3;
    alfa2 = -0.1*alfa1;

     %exciton-photon parameters
     m_cav = 1e-5*me;
     t_cav = 1;
     t_ex = 100;
     V = 5;
     E_cav0 = 1533.5;
     E_ex0  = 1533.5;
     E_ex = E_ex0 -1i*hbar/2/t_ex;

     %calculate E_LP(k=0)
     E_cav_k0 = E_cav0 + -1i*hbar/2/t_cav;
     E_LP_k0 = real(1/2*(E_ex+E_cav_k0)-1/2*((E_ex-E_cav_k0)^2 + 4*V^2)^(1/2));

     %calcualte E_pump = E_LP(k_pump)
     k_pump = 0;
```

```
     E_cav_pump = E_cav0 + hbar^2*k_pump^2/(2*m_cav)-1i*hbar/2/t_cav;
     E_LP_pump = 1/2*(E_ex+E_cav_pump)-1/2*((E_ex-E_cav_pump)^2 + 4*V^2)^(1/2);
     detuning2 = 1;
     E_pump = real(E_LP_pump)+detuning2;
     detuning = real((E_pump) - (E_LP_k0));
     disp('detuning dE = E_pump - E_LP_k0 '); disp(detuning);

     assume E_pulse = E_pump
     E_pulse = E_pump;
     k_pulse = k_pump;

     %calcualte dispersion E_LP(k) E_LP is complex
     E_cav = E_cav0 + hbar^2*k_x.^2/(2*m_cav) - 1i*hbar/2/t_cav;
     E_LP = 1/2.*(E_ex + E_cav) - 1/2*(((E_ex - E_cav).^2 + 4*V^2).^(1/2));

     %rescale E_LP(k=0) = 0
     E_LP = 1/2.*(E_ex + E_cav) - 1/2*(((E_ex - E_cav).^2 + 4*V^2).^(1/2)) - real(E_LP_k0);
     E_pulse = E_pulse - real(E_LP_k0);
     E_pump = E_pump - real(E_LP_k0);

     disp('E_pulse');disp(E_pulse);
     disp('E_pump');disp(E_pump);
     figure(2); plot(k_x,real(E_LP),k_x,real(E_pulse),k_x,real(E_pump));

     display('Ive saved variables const_gauss');
     save const_GP.mat;
     clear;

end


function GP_calculations(Pump_amplitude)
    clear;
    global psi_plus pulse_on dt;
    load_const_v3;
    load const_GP.mat;

    disp('I calculate dispersion without pulse');
    pulse_on = 0; numeric(pulse_on);  psi_plus2 = psi_plus;
    save ('psi_plus2','psi_plus2');
    disp('I calculate dispersion with pulse');
    pulse_on = 1; numeric(pulse_on);  psi_plus3 = psi_plus;
    save ('psi_plus3','psi_plus3');

    load psi_plus2;    load psi_plus3;
    psi_plus  = psi_plus3-psi_plus2;  clear psi_plus2 psi_plus3;
    save('psi_plus','psi_plus');

    psi_plus = flipud(fftshift(fft((psi_plus),[],2),2));       %FFT time
    psi_plus = fftshift(fft(fftshift(psi_plus,1),[],1),1);     %FFT space

    figure(4); pcolor(k_x,Et,abs(psi_plus).^2); figure(gcf);
    set(gca,'YDir','normal');shading flat; colormap gray; colorbar;
    xlabel('kx (um-1)'); ylabel('Et(meV)'); axis([-k_max k_max 0 4 ]);
    name = strcat('Dispersion ',dt,' with Pump=',num2str(Pump_amplitude),'.png');
    saveas(gcf,name); clear name;
    psi_plus = abs(psi_plus).^2;

    for i=1:Nt-1
        for j=1:Nx-1
            if(psi_plus(i,j)*1e8>8*1e10)
             disp('abobe exciton saturation density for GaAs 8 10^8/cm^2');
            end
```

```
      end
   end
end

%      ///////////////////////////////////////////////////////////////////////////////

function[psi_plus] = numeric(pulse_on)
global psi_plus ;
 load  const_GP;
  PSI = zeros(Nt,Nx);
  n = zeros(1,Nx);
  delta_x = 1/2000; L = 2*x_max;
  PSI(1,:) = 1;

  tt(1) = 0;
      A = [0 0 0 0 0 0; 1/4 0 0 0 0 0; 3/32 9/32 0 0 0 0; 1932/2197 ...
         -7200/2197 7296/2197 0 0 0; 439/216 -8 3680/513 -845/4104 ...
         0 0; -8/27 2 -3544/2565 1859/4104 -11/40 0];
      B = [16/135 0 6656/12825 28561/56430 -9/50 2/55];
      C = [0 1/4 3/8 12/13 1 1/2];

            for j = 1:1:4     % Runge Kutta Fehlberg
                  f1 = step_t*f ( tt(j),         PSI(j,:));
                  f2 = step_t*f ( tt(j)+C(2)*step_t, PSI(j,:) + A(2,1)*f1);
                  f3 = step_t*f ( tt(j)+C(3)*step_t, PSI(j,:,1) + A(3,1)*f1 +A(3,2)*f2);
                  f4 = step_t*f ( tt(j)+C(4)*step_t, PSI(j,:,1) + A(4,1)*f1 +A(4,2)*f2...
                     +A(4,3)*f3);
                  f5 = step_t*f ( tt(j)+C(5)*step_t, PSI(j,:,1) + A(5,1)*f1 +A(5,2)*f2...
                     +A(5,3)*f3 +A(5,4)*f4);
                  f6 = step_t*f ( tt(j)+C(6)*step_t, PSI(j,:,1) + A(6,1)*f1 +A(6,2)*f2...
                     +A(6,3)*f3 +A(6,4)*f4 +A(6,5)*f5);
                  PSI(j+1,:) = PSI(j,:) + (B(1)*f1 + B(2)*f2 + B(3)*f3 + B(4)*f4 + ...
                     B(5)*f5 + B(6)*f6);
            end
                         % Adams-Bashforth
            for j=5:1:(Nt-1)
                  gauss_numeric = PSI(j,:)+ step_t/720*(1901* f(tt(j),PSI(j,:))-2774* ...
                     f(tt(j-1),PSI(j-1,:))...
                  +2616* f(tt(j-2),PSI(j-2,:))-1274* f(tt(j-3),PSI(j-3,:))...
                  +251* f(tt(j-4),PSI(j-4,:)));

                  if( mod(j,10) == 0)
                     disp(['time: ',num2str(j*step_t)]);
                  end
                         % Adams-Moulton
                  PSI(j+1,:) = PSI(j,:)+step_t/720* ( 251*f(tt(j+1),gauss_numeric)+ ...
                     646*f(tt(j),PSI(j,:,1))...
                  -264*f(tt(j-1),PSI(j-1,:))+106*f(tt(j-2),PSI(j-2,:))...
                  -19*f(tt(j-3),PSI(j-3,:)));
                  clear gauss_numeric ;
            end
            psi_plus = PSI;
   clear j PSI tt;
  %{  %}
end

%      ///////////////////////////////////////////////////////////////////////////////

function[m_plus] = f(t1,y)
      load  const_GP;
      global  psi_plus psi_minus pulse_on Pump_amplitude;
       if t1<=Pump_to
         A=exp(-(t1-Pump_to)^2/Pump_tL^2);
```

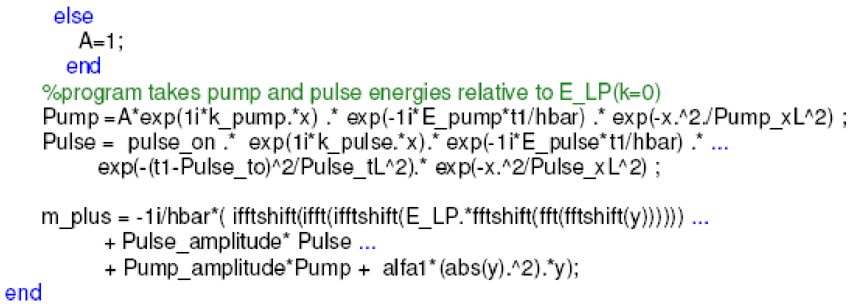

```
      else
          A=1;
        end
    %program takes pump and pulse energies relative to E_LP(k=0)
    Pump =A*exp(1i*k_pump.*x) .* exp(-1i*E_pump*t1/hbar) .* exp(-x.^2./Pump_xL^2) ;
    Pulse =  pulse_on .*  exp(1i*k_pulse.*x).* exp(-1i*E_pulse*t1/hbar) .* ...
            exp(-(t1-Pulse_to)^2/Pulse_tL^2).* exp(-x.^2/Pulse_xL^2) ;

    m_plus = -1i/hbar*( ifftshift(ifft(ifftshift(E_LP.*fftshift(fft(fftshift(y)))))) ...
             + Pulse_amplitude* Pulse ...
             + Pump_amplitude*Pump +  alfa1*(abs(y).^2).*y);
end
```

APPENDIX C SAMPLES

During this work we have designed and characterized 20 MBE wafers grown in the National Center for III-V Technology in Sheffield, UK, by Maxime Huges and Mark Hopkinson, and by Edmund Clarke. In this chapter only samples grown in National Center during the duration of this project are described. The list of samples is given in a Table C.1. The detailed growth design and sample characterization are discussed in this Chapter, references to studies on point-like-defects and cross-hatch dislocations are given where relevant. The sample design was originally made by Wolfgang Langbein, further extended by Joanna M Zajac and Wolfgang Langbein. For some samples, the actual structure differed from designed one, see discussion for each sample. Samples listed here fall into three categories, bare microcavities[1], quantum wells test samples, and microcavities with embedded quantum wells.

Wafer number	Cavity length (λ)	QW	DBR top (bottom)	requested-received date
VN1324	1λ	-	24(27)	06/08-10/08
VN1316/18	-	InGaAs	-	06/08-11/08
VN1379	-	InGaAs	-	06/08-11/08
VN1448	2λ	InGaAs	24(27)	03/09-03/09
VN1539	-	InGaAs	-	–/– -06/09
VN1623/27/33	$3/2\lambda$	InGaAs	24(27)	–/– -09/09
VN1836/39	2λ	InGaAs	19(22)	–/– -06/10
VN1968/69/70	2λ	-	23(26)	10/10-01/11
VN2217/18	2λ	-	23(26)	03/11-01/12
VN2301	2λ	-	23(26)	02/12-04/12
VN2302	-	InGaAs	-	02/12-04/12
VN2303/04/05	2λ	InGaAs	23(26)	02/12-04/12
VNxxxx	2λ	InGaAs	23(26)	06/12-xx/xx

Table C.1: Samples designed, grown and characterize during this project.

---

[1] A bare microcavity is a microcavity without quantum wells.

C.1 SAMPLE VN1324

Design
Detailed sample design is given in Table C.2 where X=59.8 nm is the $\lambda/4$ layer thickness of GaAs at 850 nm, Y=72.2 nm is the $\lambda/4$ layer thickness of AlAs at 850 nm. This is a bare microcavity sample with a designed polariton lifetime of 100 ps calculated using the transfer matrix method neglecting absorbtion losses. During the growth, the wafer temperature was ramped up to 715 °C for the AlAs Bragg layers and down to 660°C for GaAs Bragg layers, while the cavity layer was grown at 630 °C, compare Sec. 3.3.

Material	Thickness (nm)	Periods	Comment
GaAs	200	1	Buffer
GaAs	X	27	$\lambda/4$
AlAs	Y	27	$\lambda/4$
GaAs	4X	1	cavity
AlAs	Y	24	$\lambda/4$
GaAs	X	24	$\lambda/4$

Table C.2: Bare microcavity sample design

Characterisation
Sample VN1324 is described in Chap. 3 and Ref. [23, 65, 121], it is referred as MC1.
Comments
The measured microcavity wavelength was centered at 837 nm instead of designed 850 nm, its backsurface was inhomogeneous indicating inhomogeneous growth temperature over the wafer. Quality of a cavity mode varied strongly over the wafer, for more details see Chap. 3.

C.2 SAMPLE VN1316, VN1318

Design
This is a multiple quantum well test structure. The detailed sample design is given in Table C.3 where X=59.8 nm is the $\lambda/4$ layer thickness of GaAs at 850nm, Y=72.2 nm is the $\lambda/4$ layer thickness of AlAs at 850 nm, W=6 nm is the quantum well width, C=1.04 is the correction factor for the refractive index difference between GaAs and $In_{0.1}Ga_{0.9}As$. This sample was designed in order to determine the exciton energy in a 6 nm thick GaAs/$In_{0.1}Ga_{0.9}As$ quantum well.
Characterisation
Sample VN1316 and VN1318 have both the same design shown in Table C.4, but

Material	Thickness (nm)	Periods	Comment
GaAs	200	1	Buffer
$Al_{0.3}Ga_{0.7}As$	100	1	Barrier
GaAs	X-CW/2	1	$\lambda/4$
$In_{0.1}Ga_{0.9}As$	W	1	QW
GaAs	X-CW/2	1	$\lambda/8$
$In_{0.1}Ga_{0.9}As$	W	4	QW
GaAs	X-CW/2	4	$\lambda/4$
$In_{0.1}Ga_{0.9}As$	W	1	QW
GaAs	X-CW/2	1	$\lambda/8$
$In_{0.1}Ga_{0.9}As$	W	1	QW
GaAs	X-CW/2	1	$\lambda/4$
$Al_{0.3}Ga_{0.7}As$	100	1	Barrier
GaAs	10	1	Cup

Table C.3: Multiple quantum well sample design

Material	Thickness (nm)	Periods	Comment
GaAs	300	1	Buffer
$Al_{0.3}Ga_{0.7}As$	100	1	Barrier
GaAs	X-CW/2	1	$\lambda/4$
$In_{0.1}Ga_{0.9}As$	W	6	QW
GaAs	X-CW/2	6	$\lambda/4$
$Al_{0.3}Ga_{0.7}As$	100	1	Barrier
GaAs	10	1	Cup

Table C.4: Multiple quantum well VN1316 and VN1318 actual sample

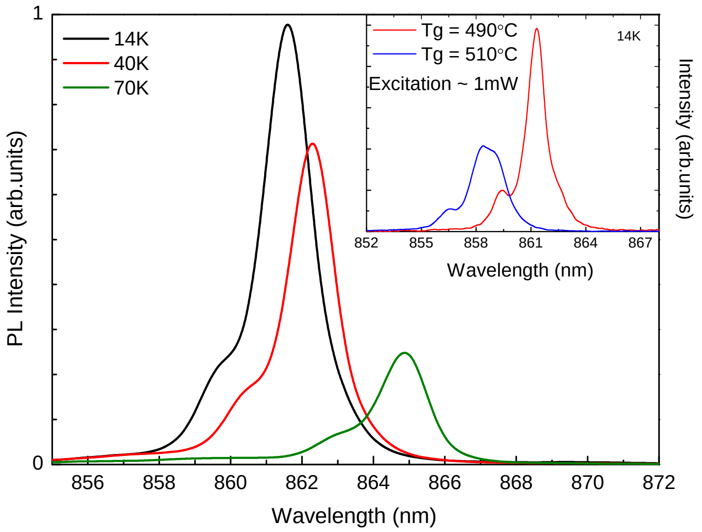

Figure C.1: Low temperature photoluminescence for sample VN1316, in the inset, exciton photoluminescence for the two wafers.

they were grown with different wafer temperatures of 490°C and 510°C. It was found that for the growth temperature of 490°C, the exciton peak has a smaller FWHM equal to 2 meV at $T = 14\,\mathrm{K}$. Moreover, in both samples, the double peak feature is visible in photoluminescence (PL) spectra in all temperatures, its origin is unclear, see Fig. C.1, possible it was due to In segregation.

Comments

A regrowth was needed in order to identify the reason behind the double peak. A multiple quantum well with six wells of different thicknesses and a 8% In content was grown for this purpose, sample VN1379.

C.3 SAMPLE VN1379

Design

This is a multiple quantum well test structure. Detailed sample design is given in Table C.5.

Material	Thickness (nm)	Periods	Comment
GaAs	100	1	
AlGaAs	100	1	
GaAs	73.6	1	
$In_{0.08}Ga_{0.92}As$	3	1	QW
GaAs	53.6	1	barrier
$In_{0.08}Ga_{0.92}As$	4	1	QW
GaAs	53.6	1	barrier
$In_{0.08}Ga_{0.92}As$	5	1	QW
GaAs	53.6	1	barrier
$In_{0.08}Ga_{0.92}As$	6	1	QW
GaAs	53.6	1	barrier
$In_{0.08}Ga_{0.92}As$	7	1	QW
GaAs	53.6	1	barrier
$In_{0.08}Ga_{0.92}As$	8	1	QW
GaAs	53.6	1	barrier
GaAs	73.6	1	
AlGaAs	100	1	
GaAs	300	1	buffer

Table C.5: Multiple quantum well sample with different well widths design

Characterisation

Sample VN1379 has six quantum wells with nominal well widths of $3, 4, 5, 6, 7, 8\,\mathrm{nm}$ and 8% In content. The 5,6,7,8 nm wells were assigned 839.3, 843.5, 847.1, 861.1 nm emission wavelength at T=14K, after peak order, as shown in Fig. C.2 where photoluminescence and optical density[2] is shown.

Comments

No double peak was observed for this quantum wells, it was decided to keep In content at 8% and 6 nm well width in the future designs.

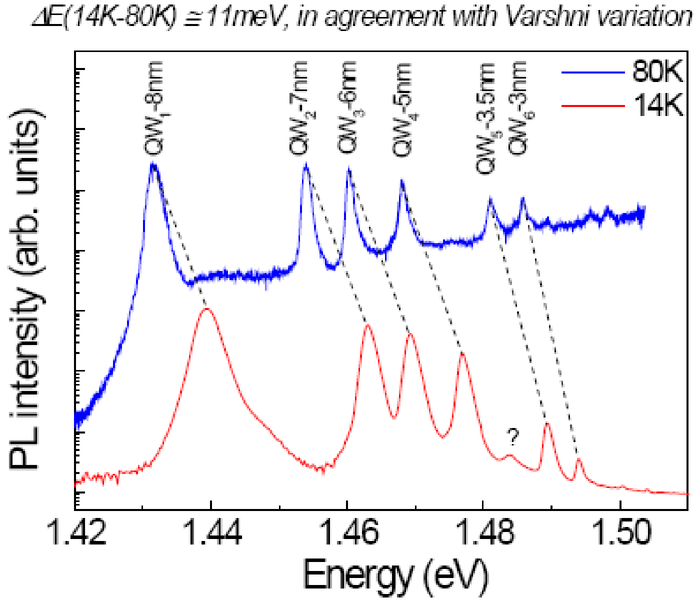

$\Delta E(14K\text{-}80K) \cong 11meV$, in agreement with Varshni variation

Figure C.2: Temperature dependent photoluminescence and optical density from multiple quantum well sample VN1379.

C.4 SAMPLE VN1448

Design

This is a microcavity structure with embedded quantum wells in the antinodes of the intracavity field, it is referred as microcavity sample full coupling. The detailed sample design is in Table C.6 where X=60.8 nm is $\lambda/4$ layer thickness of GaAs at 850 nm, Y=73.4 nm is $\lambda/4$ layer thickness of AlAs at 850 nm, X,Y were adjusted from the original values according to the real VN1324 sample, W=6 nm is a quantum well width, C=1.03 is correction factor for the refractive index difference between GaAs and $In_{0.08}Ga_{0.92}As$, B=20 nm is a barrier width which was chosen thick enough to avoid In segregation from one to another well. It was decided to introduce wafer

---

[2] Optical density was extracted from the photoluminescence by dividing PL by Boltzmann occupation factor $f = \alpha\, e^{\frac{-E}{kT}}$ where α is a fitting parameter.

Material	Thickness (nm)	Periods	Comment
GaAs substrate			
GaAs	200	1	Buffer
GaAs	X	27	$\lambda/4$ Bragg
AlAs	Y	27	$\lambda/4$ Bragg
			stop rotation
GaAs	X-CW/2	1	$\lambda/4$
			start rotation
$In_{0.08}Ga_{0.92}As$	W	1	QW carrier drain
GaAs	X-CW3/2-B/2	1	$\lambda/4$
$In_{0.08}Ga_{0.92}As$	W	2	QW active
GaAs	B	2	barrier
$In_{0.08}Ga_{0.92}As$	W	2	QW active
GaAs	2X-2CW-B	2	$\lambda/2$
$In_{0.08}Ga_{0.92}As$	W	2	QW active
GaAs	X-CW3/2-B/2	1	$\lambda/4$
$In_{0.08}Ga_{0.92}As$	W	1	QW carrier drain
			stop rotation
GaAs	X-CW/2	1	$\lambda/4$
			start rotation
AlAs	Y	24	$\lambda/4$ Bragg
GaAs	X	24	$\lambda/4$ Bragg

Table C.6: Microcavity structure full coupling rotation interruption design

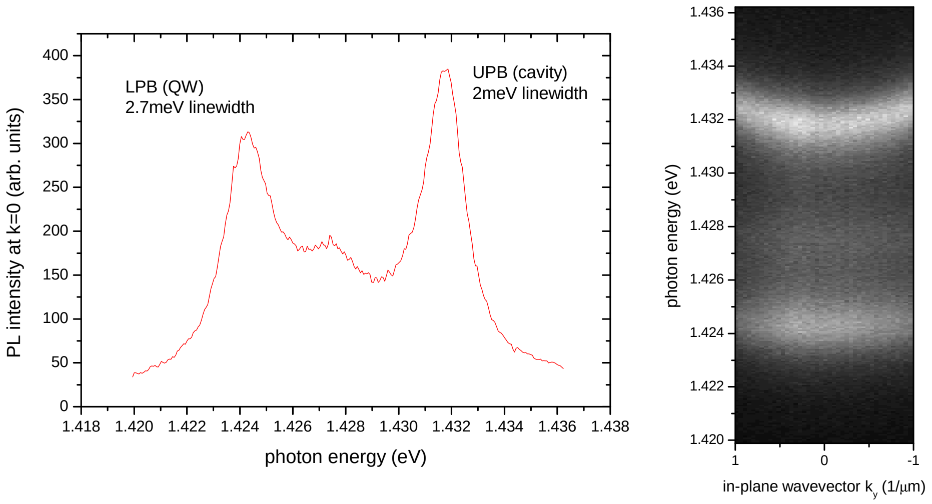

Figure C.3: Photoluminescence from microcavity sample VN1448 measured in transmission with signatures of lower and upper polariton branches.

rotation interruptions during the growth of this sample in order to increase cavity wedge, see Table C.6, compare Sec. 1.2.3 on advanced growth techniques.

Characterization

Photoluminescence was measured at 80K using Ti:Sapph excitation and Horiba Jobin-Yvon spectrometer in detection. Cavity mode wavelength was centered at 864 nm, quantum well exciton was at 871 nm as compared to designed 850 nm. Strong coupling was observed for this sample, but only with positive detunings. Low temperature photoluminescence is shown in Fig. C.3, lower and upper polaritons linewidths were 2 and 2.7 meV respectively, a signature of the third peak was also observed.

Comments

The Al source was changed before the growth of this sample, it resulted in a higher quadratic thickness gradient originating from the cell than expected, thickness gradient was equal to 30 nm over the wafer as deduced from the wavelength gradient of the upper polariton branch shown in Fig. C.4, it had to be reversed in the future growths in order to avoid inhomogeneous broadening of polariton linewidth.

In summary, regrowth was needed as the cavity mode and a quantum well exciton emission wavelength differed from designed 850 nm, and also the thickness gradient was too big. It was decided to grow firstly a quantum well structure in order to calibrate In cell.

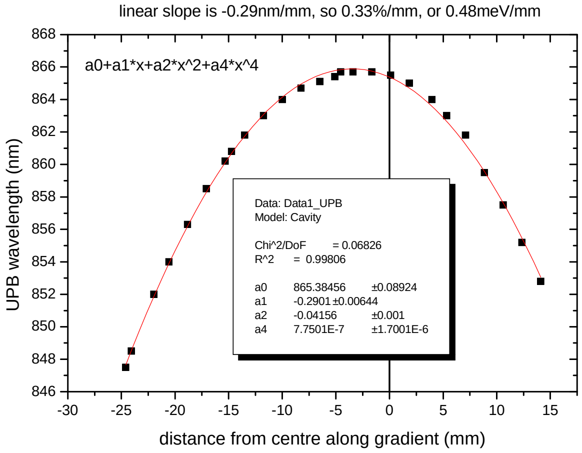

Figure C.4: Upper polariton branch wavelength gradient for microcavity sample VN1448 measured at T=80K.

C.5 SAMPLE VN1539

Design

This is multiple quantum well sample, growth design as for sample VN1316, but with less In content, namely, 7% instead of 8%, see Table C.4.

Characterisation

Optical density for this quantum well measured using He:Ne excitation is shown in Fig. C.5, heavy-hole exciton was at 848 nm at T=14 K.

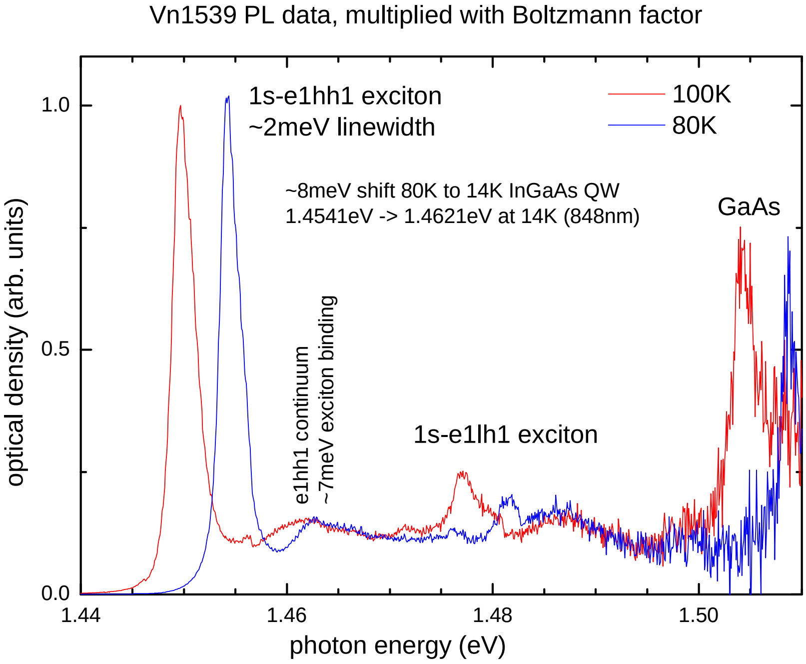

Figure C.5: Optical density for multiple quantum wells sample VN1539.

Comments

This sample was as expected except that the exciton should be at 850 nm at low temperature. Next planned sample was a repeat of microcavity sample full coupling, design in Table C.6. Because of high cell gradient, continues wafer rotation was used.

C.6 SAMPLE VN1623,VN1627,VN1633

Design

These are microcavity samples full coupling with a design given in Table C.6 but with continuous wafer rotation.

Characterisation

Samples were grown with $3/2\lambda$ cavities instead of designed 2λ and 4 quantum well instead of 6, it was due to mistake during the growth, and the resulting changed design is shown in Table C.7. For sample VN1623, strong coupling was observed for central piece of the wafer at T=80K, see Fig. C.6, positive and negative detunings

were expected for this wafer. Spectral oscillations visible in Fig. C.6 were due to reflection on the back surface of the cavity, which can be removed by HfO_2 antireflex coating as discussed in Sec. 2.6. Sample, VN1627 has a 2.6% increased thickness of X,Y, cavity is resonant at 872 nm, this sample was not requested. Sample VN1633 has a 0.8% reduced X,Y for the Bragg, and increased X for the cavity, it is at 867 nm at the center, strong coupling was observed at 15 mm from the center (853 nm quantum well), this sample was also not requested.
Low temperature measurements at T=5 K were made on sample VN1623 using simplified setup described in Chap. 5 (without AOMs). However, we did not observe renormalisation of dispersion neither signatures of BEC of polaritons (compare discussion in Chap. 6), laser power up to 110mW was used. This could be due to reduced light-matter coupling as there was less quantum wells than in the original sample design from Table C.7.

Material	Thickness (nm)	Periods	Comment
GaAs substrate			
GaAs	200	1	Buffer
GaAs	X	27	$\lambda/4$ Bragg
AlAs	Y	27	$\lambda/4$ Bragg
			stop rotation
GaAs	X-CW/2	1	$\lambda/4$
			start rotation
$In_{0.08}Ga_{0.92}As$	W	1	QW carrier drain
GaAs	X-CW3/2-B/2	1	$\lambda/4$
$In_{0.08}Ga_{0.92}As$	W	1	QW active
GaAs	B	1	barrier
$In_{0.08}Ga_{0.92}As$	W	1	QW active
GaAs	2X-2CW-B	1	$\lambda/2$
$In_{0.08}Ga_{0.92}As$	W	1	QW active
GaAs	X-CW3/2-B/2	1	$\lambda/4$
$In_{0.08}Ga_{0.92}As$	W	1	QW carrier drain
			stop rotation
GaAs	X-CW/2	1	$\lambda/4$
			start rotation
AlAs	Y	24	$\lambda/4$ Bragg
GaAs	X	24	$\lambda/4$ Bragg

Table C.7: Microcavity structure full coupling cw rotation design

Comments
In the next growth, redo sample VN1623 but with correct cavity length and number of quantum wells. Grow second sample with reduced amount of Braggs to 22(19)

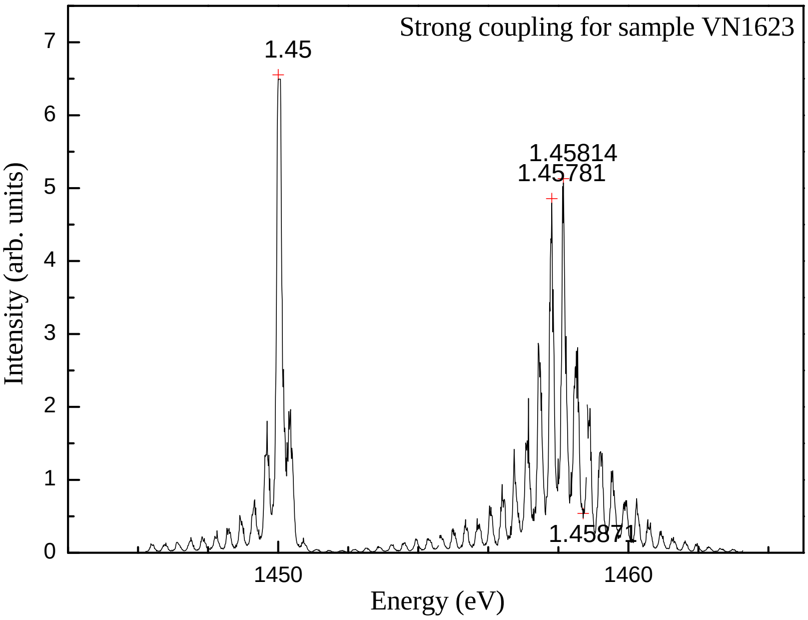

Figure C.6: Transmission spectrum from sample VN1623 at $k = 0$.

bottom(top) to reduce the nominal cavity lifetime.

C.7 Sample VN1836,VN1839

Design

Microcavity samples full coupling according to the design in Table C.6 but with continuous wafer rotation for a full wafer, the second microcavity sample has the same design but reduced number of DBRs to 22(19) bottom(top).

Characterisation

Cavity resonance for sample VN1839 was at 842 nm at T=80K, it was too much in the blue as compared to exciton resonance which was measured at 853 nm, cavity mode was broad (4 meV) due to quantum wells absorbtion. Sample VN1836 had very little transmission due to higher number of DBRs. Cavity energy gradient over sample was only about 10 nm.

Comments

Regrowth of this sample was needed with correct positioning of the cavity energies. Regrowth have not happened as Maxime Huges, who grew samples up to now, had finished his work in Sheffield, also there was reactor failure such that growth was suspended for a half a year, after that was decided to grow strain compensated samples.

C.8 Sample VN1968,VN1969,VN1970

Design

These are strain compensated bare microcavity samples. Detailed sample design is given in Table C.8 where X=60.8 nm is a $\lambda/4$ layer thickness of GaAs at 850 nm, Y is a $\lambda/4$ layer thickness of AlAs at 850 nm which depends on the AlP content in DBRs, namely, (Y,Z)= (73.4 nm,0 nm) for the 0% AlP sample, (Y,Z)= (72 nm,1.5 nm) for the 2% AlP sample, (Y,Z)= (71.3 nm,2.2 nm) for the 3% AlP sample. Samples were grown on undoped double side polished three-inch wafers with continues wafer rotation.

Material	Thickness (nm)	Periods	Comment
GaAs	X	23	$\lambda/4$ Bragg
AlAs	Y/2	23	$\lambda/4$ Bragg
AlP	Z	23	including AlP strain
AlAs	Y/2	23	compensating inset
GaAs	8X	1	2λcavity
AlAs	Y/2	26	$\lambda/4$ Bragg
AlP	Z	26	including AlP strain
AlAs	Y/2	26	compensating inset
GaAs	X	26	$\lambda/4$ Bragg
GaAs	200	1	buffer

Table C.8: Strain compensated bare microcavity samples design

Characterisation

Samples VN1968,VN1969,VN1970 were characterized in Chap. 4 and Ref. [107]. Sample VN1968 was characterize in Chap. 3 and Ref. [23, 65], it is refereed there as MC2.

Comments

Effect of strain compensation was succesfuly observed, however, more samples were needed in order to investigate this effect in more details. It was decided to grow two new samples with AlP content of 1% and 1.5%. They were grown 1 year later due to the MBE reactor failure.

C.9 Sample VN2217,VN2218

Design

These are strain compensated bare microcavity samples. Sample design is shown in Table C.8 with X layer thickness as for VN1968-70 samples, while Y was chosen as (Y,Z)= (72.7 nm,0.75 nm) for the 1% AlP sample, (Y,Z)= (72.35 nm,1.13 nm) for the

1.5% AlP sample. Samples were grown on undoped double side polished three-inch wafers with continues wafer rotation.

Characterisation

Samples VN2217 with 1% AlP content had strongly inhomogenous transmission and broad cavity mode with FWHM=1meV, there was a problem with Al cell stability during this growth and this sample was disregarded. Sample VN2218 with 1.5% AlP content had spatially homogenous transmission not indicating any problems during the growth, it is described in Chap. 4 and Ref. [107].

Comments

Effect of strain compensation resulting in the suppression of the cross-hatch dislocation pattern was successfully observed, it is described in Chap. 4 and Ref. [107].

C.10 SAMPLE VN2301-05

Design

VN2301 is a bare microcavity sample, repeat of VN2217. Sample VN2302 is a single quantum well calibration sample. Samples VN2303-05 are strain compensated microcavity samples full coupling, AlP concentration of 1.2% was used here, samples were design in a sequence of three with the X,Y lengths multiplied by factor of 1, 1.01, and 1.02 respectively, in order to match quantum well exciton and cavity mode in case of growth instabilities and provide different detuning ranges, for detailed growth receipt see Table C.9 where X was as for VN1968,VN1969,VN1970 samples, Y thickness was chosen as 72.56 nm, Z=0.9 nm is the AlP layer thickness, W=6 nm is a quantum well width, C=1.03 is a correction factor of refractive index between GaAs and $In_{0.08}Ga_{0.92}As$, B=20 nm is a barrier width.

Characterisation

Sample VN2301 has good quality, it is described in Chap. 4 and Ref. [107]. Cavity sample VN2303 was centered at 860 nm, VN2304 at 867 nm, VN2306 at 855 nm while a quantum well exciton was centered at 847 nm with FWHM=4meV as measured with He:Ne at T=80K for sample VN2302. The exciton wavelength was shifting towards shorter wavelengths as measured for chronologically ordered samples, this could indicate uncompensated depletion of In cell during the growth. There was no strong coupling for these samples.

Comments

Regrowth is needed.

Material	Thickness (nm)	Periods	Comment
GaAs	X	23	$\lambda/4$ Bragg
AlAs	Y/2	23	$\lambda/4$ Bragg
AlP	Z	23	including AlP strain
AlAs	Y/2	23	compensating inset
GaAs	X-CW/2	1	$\lambda/4$ reduce T
$In_{0.08}Ga_{0.92}As$	W	1	QW carrier trap
GaAs	X-CW3/2-B/2	1	$\lambda/4$
$In_{0.08}Ga_{0.92}As$	W	2	QW
GaAs	B	2	barrier
$In_{0.08}Ga_{0.92}As$	W	2	QW
GaAs	2X-2CW-B	1	$\lambda/2$
$In_{0.08}Ga_{0.92}As$	W	1	QW
GaAs	B	2	barrier
GaAs	X-CW3/2-B/2	1	$\lambda/4$
$In_{0.08}Ga_{0.92}As$	W	2	QW
GaAs	X-CW/2	1	$\lambda/4$ reduce T
AlAs	Y/2	26	compensating inset
AlP	Z	26	including AlP strain
AlAs	Y/2	26	$\lambda/4$ Bragg
GaAs	X	26	$\lambda/4$ Bragg
GaAs	200 nm	1	buffer

Table C.9: Strain compensated strongly coupled microcavity samples design

C.11 SAMPLE REQUESTED 6/2012

Design

Requested samples are strain compensated mcrocavity samples repeat of design in Table C.9 again in a sequence of three with X,Y lengths multiplied by factor of 1.014, 1.004, 0.994, see design in Table C.10. Wafer rotation stop was introduced for $\lambda/2$ layer in order to increase thickness gradient over the wafer, calculated gradient using the same Al cell parameters as for VN2306 was 25 nm over the wafer. Also a fourth sample was requested with even higher thickness gradient of 30 nm over the three-inch wafer. Design of this sample was as in Table C.10 but starting the rotation in the middle of the $\lambda/4$ layer after the first quantum well, and stopping rotation in the middle of the $\lambda/4$ layer before the last quantum well.

Comments

These samples were not received at the time of submission of this thesis.

Material	Thickness (nm)	Periods	Comment
GaAs	X	23	$\lambda/4$ Bragg
AlAs	Y/2	23	$\lambda/4$ Bragg
AlP	Z	23	including AlP strain
AlAs	Y/2	23	compensating inset
			stop rotation before layer
GaAs	X-CW/2	1	$\lambda/4$ reduce T
			start rotation after layer
$In_{0.08}Ga_{0.92}As$	W	1	QW carrier trap
GaAs	X-CW3/2-B/2	1	$\lambda/4$
$In_{0.08}Ga_{0.92}As$	W	2	QW
GaAs	B	2	barrier
$In_{0.08}Ga_{0.92}As$	W	2	QW
GaAs	2X-2CW-B	1	$\lambda/2$
$In_{0.08}Ga_{0.92}As$	W	1	QW
GaAs	B	2	barrier
GaAs	X-CW3/2-B/2	1	$\lambda/4$
$In_{0.08}Ga_{0.92}As$	W	2	QW
			stop rotation before layer
GaAs	X-CW/2	1	$\lambda/4$ reduce T
			start rotation before layer
AlAs	Y/2	26	compensating inset
AlP	Z	26	including AlP strain
AlAs	Y/2	26	$\lambda/4$ Bragg
GaAs	X	26	$\lambda/4$ Bragg
GaAs	200 nm	1	buffer

Table C.10: Strain compensated strongly coupled microcavity samples with rotation interruption design

Summary

As for the present day, we received bare microcavity samples with long photon lifetime and strain compensated bare microcavity samples, we did not received strongly coupled strain compensated microcavity samples with long photon lifetime which could be used for the purpose of the polariton quantum fluid measurements.

Appendix D Abbreviations

Physical constants and abbreviations commonly used in the main text are short listed below.

c-speed of light $c = 3 \cdot 10^8$m/s^2
e-electron charge $e = -1.6^{-19}C$
m_e-electron mass $m_e = 0.51$ MeV/c^2

AFM-atomic force microscope
DBRs-distributed Bragg reflectors
FIB-focused-ion beam
FESEM-field emission scanning electron microscopy
FF-far-field
FWHM-full width at half maximum
GP-Gross-Pitaevskii equation
MBE-molecular beam epitaxy
MC-microcavity
MD-misfit dislocations
NF-near field
PD-point-like defects
QW-quantum well
RF - radio frequency
SEM-scanning electron microscopy
TD-threading dislocations

BIBLIOGRAPHY

[1] C. Weisbuch, M. Nishioka, A. Ishikawa and Y. Arakawa. Observation of the coupled exciton-photon mode splitting in a semiconductor quantum microcavity. *Phys. Rev. Lett.*, **69**, 3314 (1992).

[2] H. Deng, G. Weihs, C. Santori, J. Bloch and Y. Yamamoto. Condensation of semiconductor microcavity exciton polaritons. *Science*, **298**, 199 (2002).

[3] J. Kasprzak, M. Richard, S. Kundermann, A. Baas, P. Jeambrun, J. M. J. Keeling, F. M. Marchetti, M. H. Szymanska, R. Andre, J. L. Staehli, V. Savona, P. B. Littlewood, B. Deveaud and L. S. Dang. Bose-Einstein condensation of exciton polaritons. *Nature*, **443**, 409 (2006).

[4] C. W. Lai, N. Y. Kim, S. Utsunomiya, G. Roumpos, H. Deng, M. D. Fraser, T. Byrnes, P. Recher, N. Kumada, T. Fujisawa and Y. Yamamoto. Coherent zero state and p state in an exciton polariton condensate array. *Nature*, **450**, 529 (2007).

[5] K. G. Lagoudakis, M. Wouters, M. Richard, A. Baas, I. Carusotto, R. Andr, D. L. S. Dang and B. Deveaud-Plédran. Quantized vortices in an exciton-polariton condensate. *Nature Physics*, **4**, 706 (2008).

[6] A. Amo, J. Lefrre, S. Pigeon, C. Adrados, C. Ciuti, I. Carusotto, R. Houdr, E. Giacobino and A. Bramati. Superfluidity of polaritons in semiconductor microcavities. *Nature Physics*, **5**, 805 (2009).

[7] T. Liew, I. Shelykh and G. Malpuech. Polaritonic devices. *Physica E*, **43**, 1543 (2011).

[8] K. B. Davis, M. O. Mewes, M. R. Andrews, N. J. van Druten, D. S. Durfee, D. M. Kurn and W. Ketterle. Bose-Einstein condensation in a gas of sodium atoms. *Phys. Rev. Lett.*, **75**, 3969 (1995).

[9] H. W. O. Madelung, M. Schulz, editor. *Landolt-Bornstein Numerical data and functional relationships in science and technology, Vol 17, Semiconductors, Physics of group IV elements and III - V compounds* (Springer-Verlag Berlin, 1982).

[10] J. Jensen. *MBE-grown semiconductor nanostrucutres with electronic and photonic confinment.* Ph.D. thesis, Research Centre COM, Technical University Denmark (2000).

[11] J. R. Chelikowsky and M. L. Cohen. Nonlocal pseudopotential calculations for the electronic structure of eleven diamond and zinc-blende semiconductors. *Phys. Rev. B*, **14**, 556 (1976).

[12] *Properties of Galium Arsenide 2nd edition* (INSPEC, 1990).

[13] S. Gehrsitz, F. K. Reinhart, C. Gourgon, N. Herres, A. Vonlanthen and H. Sigg. The refractive index of $Al_xGa_{1-x}As$ below the band gap: Accurate determination and empirical modeling. *J. Appl. Phys.*, **87**, 7825 (2000).

[14] Y. Singh. *Semiconductor Devices* (I.K.International Publishing House, 2009).

[15] P. Bhattacharya. *EMIS Datareviews Series, Properties of Lattice-Matched and Strained Indium Gallium Arsenide* (INSPE, 1993).

[16] C. Klingshirn. *Semiconductor Optics.* Advanced Texts in Physics (Springer, 2005). ISBN 9783540213284.

[17] E. S. Koteles and J. Y. Chi. Experimental exciton binding energies in $GaAs/Al_{x}Ga_{1-x}As$ quantum wells as a function of well width. *Phys. Rev. B*, **37**, 6332 (1988).

[18] V. Savona, C. Piermarocchi, A. Quattropani, P. Schwendimann and F. Tassone. Optical properties of microcavity polaritons. *Phase Transitions*, **68**, 169 (1998).

[19] R. C. Miller, D. A. Kleinman, W. T. Tsang and A. C. Gossard. Observation of the excited level of excitons in GaAs quantum wells. *Phys. Rev. B*, **24**, 1134 (1981).

[20] H. Haug and S. Koch. *Quantum theory of the optical and electronic properties of semiconductors* (World Scientific, 1990).

[21] M. Born and E. Wolf. *Principles of Optics: Electromagnetic Theory of Propagation, Interference and Diffraction of Light* (Cambridge University Press, 2000). ISBN 9780521784498.

[22] M. Skolnick. Strong coupling phenomena in quantum microcavity structures. *Semicond. Sci. Technol.*, **13, 7**, 645 (1998).

[23] J. M. Zajac, W. Langbein, M. Hugues and M. Hopkinson. Polariton states bound to defects in GaAs/AlAs planar microcavities. *Phys. Rev. B*, **85**, 165309 (2012).

[24] J. J. Hopfield and D. G. Thomas. Theoretical and experimental effects of spatial dispersion on the optical properties of crystals. *Phys. Rev.*, **132**, 563 (1963).

[25] A. Kavokin, J. Baumberg, G. Malpuech and F. Laussy. *Microcavities.* Series on Semiconductor Science and Technology (OUP Oxford, 2007). ISBN 9780191620737.

[26] C. Ciuti, P. Schwendimann and A. Quattropani. Theory of polariton parametric interactions in semiconductor microcavities. *Semicond. Sci. Technol.*, **18**, S279 (2003).

[27] M. Fox. *Quantum Optics.* Oxford Master Series in Physics (OUP Oxford, 2006). ISBN 9780198566731.

[28] A. Tredicucci, Y. Chen, V. Pellegrini, M. Börger, L. Sorba, F. Beltram and F. Bassani. Controlled exciton-photon interaction in semiconductor bulk microcavities. *Phys. Rev. Lett.*, **75**, 3906 (1995).

[29] Y. Chen, A. Tredicucci and F. Bassani. Bulk exciton polaritons in GaAs microcavities. *Phys. Rev. B*, **52**, 1800 (1995).

[30] B. Deveaud. *The Physics of Semiconductor Microcavities* (John Wiley & Sons, 2007). ISBN 9783527610167.

[31] U. Oesterle, R. P. Stanley and R. Houdré. MBE growth of high finesse microcavities. *Phys. Status Solidi B*, **242**, 2157 (2005).

[32] S. Koshiba, Y. Nakamura, M. Tsuchiya, H. Noge, H. Kano, Y. Nagamune, T. Noda and H. Sakaki. Surface diffusion processes in molecular beam epitaxial growth of GaAs and AlAs as studied on GaAs (001)-(111)B facet structures. *J Appl Phys.*, **76**, 4138 (1994).

[33] C. Kittel. *Wstęp do fizyki ciała stałego* (Państwowe Wydawnictwo Naukowe, 1976).

[34] J. R. Jensen, P. Borri, W. Langbein and J. M. Hvam. Ultranarrow polaritons in a semiconductor microcavity. *Appl. Phys. Lett.*, **76**, 3262 (2000).

[35] I. Carusotto and C. Ciuti. Probing microcavity polariton superfluidity through resonant Rayleigh scattering. *Phys. Rev. Lett.*, **93**, 166401 (2004).

[36] S. Reitzenstein and A. Forchel. Quantum dot micropillars. *J. Phys. D: Appl. Phys.*, **43**, 033001 (2010).

[37] C. Grossmann, C. Coulson, G. Christmann, I. Farrer, H. E. Beere, D. A. Ritchie and J. J. Baumberg. Tuneable polaritonics at room temperature with strongly coupled Tamm plasmon polaritons in metal/air-gap microcavities. *Appl. Phys. Lett.*, **98**, 231105 (2011).

[38] *Sacher Company User's Manual: Tunable Littrow External Cavity Diode Laser, Lynx* (2006).

[39] J. H. Rubin T., Altman W. Coefficients of thermal expansion of solids at low temperatures I the thermal expansion of copper from 15 to 300 k. *Journal of the American Chemical Society*, **76**, 5289 (1954).

[40] S. Schneider. Aufbau eines hochauflösenden abbildenden Spektrometers (2000).

[41] W. Langbein. Coherent optical spectroscopy of semiconductor nanostructures. *Rivista del nuovo cimento*, **33**, 255 (2010).

[42] D. Meschede. *Optics, Light and Lasers* (Wiley VCH, 2003).

[43] J. G. Grabmaier and C. B. Watson. Dislocation etch pits in single crystal GaAs. *Phys. Status Solidi B*, **32**, K13 (1969).

[44] S. Amelinckx. *The direct observation of dislocations* (Academic Press New York and London, 1964).

[45] J. W. Matthews and A. E. Blakeslee. Defects in epitaxial multilayers. *J. Crystal Growth*, **27**, 118 (1974).

[46] W. L. Bond and J. Andrus. Photographs of the stress field around edge dislocations. *Phys. Rev.*, **101**, 1211 (1956).

[47] W. Heinke and H. J. Queisser. Photoluminescence at dislocations in GaAs. *Phys. Rev. Lett.*, **33**, 1082 (1974).

[48] K. Bacher and J. S. Harris. A wet etching technique for accurate etching of GaAs/AlAs distributed Bragg reflectors. *J. Electrochem. Soc.*, **142**, 2386 (1995).

[49] M. Shinohara, T. Ito and Y. Imamura. Generation and propagation of defects into molecular beam epitaxially grown GaAs from an underlying GaAs substrate. *J. Appl. Phys*, **58**, 3449 (1985).

[50] L. A. Giannuzzi and F. A. Stevie, editors. *Introduction to focused ion beams: instrumentation, theory, techniques, and practise* (Springer-Verlag Berlin, 2005).

[51] Hafnium oxide, HfO_2 for optical coatings, product leaflet. Technical report, CERAC incorporated subsidary of Williams Advanced Materials (2007).

[52] *AUTO 306: EB3 muli-hearth electron beam source and accessories* (2003).

[53] *Dektak 8 Advanced Development Profiler Manual Veeco* (2003).

[54] J. Aarik, A. Aidla, A. Kiisler, T. Uustare and V. Sammelselg. Influence of substrate temperature on atomic layer growth and properties of HfO_2 thin films. *Thin Solid Films*, **340**, (1990).

[55] Y. Wang, Z. Lin, X. Cheng, H. Xiao, F. Zhang and S. Zou. Study of Hfo_2 thin films prepared by electron beam evaporation. *Applied Surface Science*, **228**, 93 (2004).

[56] M. F. Al-Kuhaili, S. M. A. Durrani and E. E. Khawaja. Characterization of hafnium oxide thin films prepared by electron beam evaporation. *J. Phys. D: Appl. Phys.*, **37**, 1254 (2004).

[57] M. Herman and H. Sitter. *Molecular Beam Epitaxy* (Springer-Verlag Berlin, 1989).

[58] N. Chand and S. Chu. A comprehensive study and methods of elimination of oval defcts in MBE-GaAs. *J. Cryst. Growth*, **104**, 485 (1990).

[59] K. Fujiwara, K. Kanmoto, Y. Ohta, Y. Tokuda and T. Nakayama. Classification and origins of GaAs oval defects grown by molecular beam epitaxy. *J. Cryst. Growth*, **80**, 104 (1987).

[60] C. Orme, M. D. Johnson, K. T. Leung and B. G. Orr. AFM and STM studies of large-scale unstable growth formed during GaAs(001) homoepitaxy. *Material Research Society Symposium Proceedings Vol 340* (1994). ISSN 0921-5107.

[61] P. Kreutzer, T. Zacher, W. Naumann, T. Franke and R. Anton. Comparative REM and AFM investigations of the surface recovery of MBE-grown GaAs(001)-layers during annealing. *Ultramicroscopy*, **76**, 107 (1999).

[62] H. Kawada, S. Shirayone and K. Takahashi. Reduction of surface defects in GaAs layers grown by MBE. *J. Cryst. Growth*, **128**, 550 (1993).

[63] P. Brunemeier. Observation of gallium source "spitting". *J. Vac.Sci. Technol.B*, **9,5**, 2554 (1991).

[64] E. Clarke. Private communication (2012).

[65] J. M. Zajac and W. Langbein. Structure and zero-dimensional polariton spectrum of natural defects in gaas/alas microcavities. *Phys. Rev. B*, **86**, 195401 (2012).

[66] G. Kocherscheidt, W. Langbein, G. Mannarini and R. Zimmermann. Spectral speckle analysis of resonant secondary emission from solids. *Phys. Rev. B*, **66**, 161314(R) (2002).

[67] R. I. Kaitouni, O. E. Daf, A. Baas, M. Richard, T. Paraiso, P. Lugan, T. Guillet, F. Morier-Genoud, J. D. Ganire, J. L. Staehli, V. Savona and B. Deveaud. Engineering the spatial confinement of exciton polaritons in semiconductors. *Phys. Rev. B*, **74**, 155311 (2006).

[68] D. Sanvitto, A. Amo, L. Viña, R. André, D. Solnyshkov and G. Malpuech. Exciton-polariton condensation in a natural two-dimensional trap. *Phys. Rev. B*, **80**, 045301 (2009).

[69] M. Abramowitz and I. Stegun. *Handbook of Mathematical Functions: with Formulas, Graphs, and Mathematical Tables* (Dover Publications, 1965).

[70] N. McLachlan. *Theory and applications of Mathieu functions* (Oxford, 1947).

[71] H. Waalkens, J. Wiersig and H. R. Dullin. Elliptic quantum billiard. *Ann. Phys*, **260**, 50 (1997).

[72] R. Coïsson, G. Vernizzi and X. Yang. Mathieu functions and numerical solutions of the mathieu equation. *IEEE Proceedings of International Workshop ?Open source software for scienti?c computation? (OSSC), Guiyang*, pages 3–10 (2009).

[73] T. Mano, T. Kuroda, S. Sanguinetti, T. Ochiai, T. Tateno, J. Kim, T. Noda, M. Kawabe, K. Sakoda, G. Kido and N. Koguchi. Self-assembly of concentric quantum double rings. *Nano Lett.*, **5**, 425 (2005).

[74] K. Ohta, T. Kojima and T. Nakagawa. Anisotropic surface migration of Ga atoms on GaAs (001). *J. Cryst. Growth*, **95**, 71 (1989).

[75] D. K. Biegelsen, R. D. Bringans, J. E. Northrup and L.-E. Swartz. Surface reconstructions of GaAs(100) observed by scanning tunneling microscopy. *Phys. Rev. B*, **41**, 5701 (1990).

[76] R. Cerna, D. Sarchi, T. K. Paraso, G. Nardin, Y. Lèger, M. Richard, B. Pietka, O. E. Daif, F. Morier-Genoud, V. Savona, M. T. Portella-Oberli and B. Deveaud-Plédran. Coherent optical control of the wave function of zero-dimensional exciton polaritons. *Phys. Rev. B*, **80**, 121309(R) (2009).

[77] V. Mantovani, S. Sanguinetti, M. Guzzi, E. Grilli, M. Gurioli, K. Watanabe and N. Koguchi. Low density GaAs/AlGaAs quantum dots grown by modified droplet epitaxy. *J. Appl. Phys.*, **96**, 4416 (2004).

[78] T. Paraiso, M. Wouters, Y. Leger, F. Morier-Genoud and B. Deveaud-Plédran. Multistability of a coherent spin ensemble in a semiconductor microcavity. *Nature Materials*, **9**, 655 (2010).

[79] M. Gurioli, F. Bogani, D. S. Wiersma, P. Roussignol, G. Cassabois, G. Khitrova and H. Gibbs. Experimental study of disorder in a semiconductor microcavity. *Phys. Rev. B*, **64**, 165309 (2001).

[80] W. Langbein and J. M. Hvam. Elastic scattering dynamics of cavity polaritons: Evidence for time-energy uncertainty and polariton localization. *Phys. Rev. Lett.*, **88**, 047401 (2002).

[81] W. Langbein. Microcavity polariton dynamics in real and reciprocal space. In *Proc. 26th Int. Conf. on the Physics of Semiconductors* (2002).

[82] M. Abbarchi, C. Diederichs, L. Largeau, V. Ardizzone, O. Mauguin, T. Lecomte, A. Lemaitre, J. Bloch, P. Roussignol and J. Tignon. Discretized disorder in

planar semiconductor microcavities: Mosaicity effect on resonant rayleigh scattering and optical parametric oscillation. *Phys. Rev. B*, **85**, 045316 (2012).

[83] A. Mazuelas, R. Hey, B. Jenichen and H. T. Grahn. Alternating Be and C doping for strain compensated GaAs/AlAs distributed Bragg reflectors. *Appl. Phys. Lett.*, **70**, 2088 (1997).

[84] A. M. Andrews, J. S. Speck, A. E. Romanov, M. Bobeth and W. Pompe. Modeling cross-hatch surface morphology in growing mismatched layers. *J. Appl. Phys.*, **91**, 1933 (2002).

[85] B.L.Weiss, editor. *EMIS Data Review Series No 7, Properties of Aluminium Galium Arsenide* (INSPEC, 1993).

[86] M. Ettenberg and R. Paff. Thermal expansion of AlAs. *J Appl Phys.*, **41**, 3926 (1970).

[87] B. Monemar. Determination of band gap and refractive index of AIP from optical absorption. *Solid State Commun.*, **8**, 1295 (1970).

[88] S. Y. Shiryaev, F. Jensen, J. L. Hansen, J. W. Petersen and A. N. Larsen. Nanoscale structuring by misfit dislocations in $\mathrm{Si}_{1-x}\mathrm{Ge}_x$/Si epitaxial systems. *Phys. Rev. Lett.*, **78**, 503 (1997).

[89] R. W. Boyd. *Nonlinear Optics* (Academic Press, 2008).

[90] P. G. Savvidis, J. J. Baumberg, R. M. Stevenson, M. S. Skolnick, D. M. Whittaker and J. S. Roberts. Angle-resonant stimulated polariton amplifier. *Phys. Rev. Lett.*, **84**, 1547 (2000).

[91] D. Sanvitto, D. M. Whittaker, M. S. Skolnick and J. S. Roberts. Continuous wave pump-probe experiment on a planar microcavity. *Phys. Status Solidi A*, **202**, 353 (2005).

[92] C. Ciuti, P. Schwendimann and A. Quattropani. Parametric luminescence of microcavity polaritons. *Phys. Rev. B*, **63, 4**, 5 (2001). Parametric.

[93] W. Langbein. Spontaneous parametric scattering of microcavity polaritons in momentum space. *Phys. Rev. B*, **70**, 205301 (2004).

[94] W. Langbein. Polariton correlation in microcavities produced by parametric scattering. *Phys. Status Solidi B*, **242**, 2260 (2005).

[95] S. Savasta, O. D. Stefano, V. Savona and W. Langbein. Quantum complementarity of microcavity polaritons. *Phys. Rev. Lett.*, **94**, 246401 (2005).

[96] J. L. O'Brien, A. Furusawa and J. Vucovic. Photonic quantum technologies. *Nature Photonics*, **3**, 687 (2009).

[97] C. Diederichs, J. Tignon, G. Dasbach, C. Ciuti, A. Lemaitre, J. Bloch, P. Roussignol and C. Delalande. Parametric oscillation in vertical triple microcavities. *Nature*, **440**, 904 (2006).

[98] M. Abbarchi, V. Ardizzone, T. Lecomte, A. Lemaitre, I. Sagnes, P. Senellart, J. Bloch, P. Roussignol and J. Tignon. One-dimensional microcavity-based optical parametric oscillator: Generation of balanced twin beams in strong and weak coupling regime. *Phys. Rev. B*, **83**, 201310 (2011).

[99] V. Ardizzone, M. Abbarchi, T. Lecomte, A. Lemaitre, I. Sagnes, P. Senellart, J. Bloch, P. Roussignol and J. Tignon. Optical parametric oscillaton in 1d semiconductor microcavities. *Phys. Status Solidi B*, **249**, 896 (2012).

[100] D. F. Walls and G. Milburn. *Quantum optics*. Springer Study Edition (Springer-Verlag, 1995). ISBN 9783540588313.

[101] L. Landau and E. Lifszyc. *Mechanika kwantowa: Teoria nierelatywistyczna*. Fizyka teoretyczna (Państwowe Wydaw. Naukowe, 1958).

[102] C. Ciuti and I. Carusotto. Quantum fluid effects and parametric instabilities in microcavities. *Phys. Status Solidi B*, **242, 11**, 2224 (2005).

[103] Bogoliubov. On the theory of superfluidity. *J Phys.*, **XI**, 292 (1946).

[104] P. Borri, W. Langbein, U. Woggon, J. R. Jensen and J. M. Hvam. Microcavity polariton linewidths in the weak-disorder regime. *Phys. Rev. B*, **63**, 035307 (2001).

[105] J. R. Jensen, J. M. Hvam and W. Langbein. Optical properties of InAlGaAs quantum wells: Influence of segregation and band bowing. *J. Appl. Phys.*, **86**, 2584 (1999).

[106] K. Leosson, J. R. Jensen, W. Langbein and J. M. Hvam. Exciton localization and interface roughness in growth-interrupted GaAs/AlAs quantum wells. *Phys. Rev. B*, **61**, 10322 (2000).

[107] J. M. Zajac, E. Clarke and W. Langbein. Suppression of cross-hatched polariton disorder in GaAs/AlAs microcavities by strain compensation. *Appl. Phys. Lett.*, **101**, 041114 (2012).

[108] A. Huynh, J. Tignon, O. Larsson, P. Roussignol, C. Delalande, R. André, R. Romestain and L. S. Dang. Polariton parametric amplifier pump dynamics in the coherent regime. *Phys. Rev. Lett.*, **90**, 106401 (2003).

[109] C. Ciuti, P. Schwendimann, B. Deveaud and A. Quattropani. Theory of the angle-resonant polariton amplifier. *Phys. Rev. B*, **62**, R4825 (2000).

[110] D. D. Solnyshkov, I. A. Shelykh, N. A. Gippius, A. V. Kavokin and G. Malpuech. Dispersion of interacting spinor cavity polaritons out of thermal equilibrium. *Phys. Rev. B*, **77**, 045314 (2008).

[111] L. Pitaevskii and S. Stringari. *Bose-Einstein Condensation*. International Series of Monographs on Physics (Oxford University Press, USA, 2003). ISBN 9780198507192.

[112] S. Utsunomiya, L. Tian, G. Roumpos, C. W. Lai, N. Kumada, T. Fujisawa, M. Kuwata-Gonokami, A. Löffler, S. Höfling, A. Forchel and Y. Yamamoto. Observation of Bogoliubov excitations in exciton polariton condensates. *Nature Physics*, **4**, 700 (2008).

[113] A. Amo, D. Sanvitto, F. P. Laussy, D. Ballarini, E. del Valle, M. D. Martin, A. Lematre, J. Bloch, D. N. Krizhanovskii, M. S. Skolnick, C. Tejedor and L. Via. Collective fluid dynamics of a polariton condensate in a semiconductor microcavity. *Nature*, **457**, 291 (2009).

[114] M. Sich, D. N. Krizhanovskii, M. S. Skolnick, A. V. Gorbach, R. Hartley, D. V. Skryabin, E. A. Cerda-Méndez, K. Biermann, R. Hey and P. V. Santos. Observation of bright polariton solitons in a semiconductor microcavity. *Nature Photonics*, **6**, 50 (2012).

[115] A. Amo, S. Pigeon, D. Sanvitto, V. G. Sala, R. Hivet, I. Carusotto, F. Pisanello, G. Lemenager, R. H. E. Giacobino, C. Ciuti and A. Bramati. Polariton superfluids reveal quantum hydrodynamic solitons. *Science*, **332, 6034**, 1167 (2011).

[116] T. Liew. Private communication (2009).

[117] J. Mathews and K. Fink. *Numerical methods using MATLAB* (Pearson Prentice Hall, 2003). ISBN 9780130652485.

[118] Z. Fortuna, B. Macukow and J. Wasowski. *Metody numeryczne* (Wydawnictwo Naukowo Techniczne Warszawa, 2005).

[119] J. Osborne, C. Bording, Lynes.H, L. Daly, M. Guest, H. Beedie and C. Kitchen. Introduction to Condor arcca Cardiff University (2009).

[120] J. Kasprzak, R. André, L. S. Dang, I. A. Shelykh, A. V. Kavokin, Y. G. Rubo, K. V. Kavokin and G. Malpuech. Build up and pinning of linear polarization in the Bose condensates of exciton polaritons. *Phys. Rev. B*, **75**, 045326 (2007).

[121] M. Maragkou, C. E. Richards, T. Ostatnický, A. J. D. Grundy, J. Zajac, M. Hugues, W. Langbein and P. G. Lagoudakis. Optical analogue of the spin Hall effect in a photonic cavity. *Opt. Lett.*, **36**, 1095 (2011).